ESTIMATION OF PARAMETERS IN CONDUCTION-RADIATION HEAT TRANSFER IN POROUS MEDIA

A Thesis

Submitted by

VIJAY KUMAR MISHRA

for the award of the degree

of

DOCTOR OF PHILOSOPHY

DEPARTMENT OF MECHANICAL ENGINEERING

INDIAN INSTITUTE OF TECHNOLOGY GUWAHATI

MAY 2016

CERTIFICATE

It is certified that the work contained in this thesis entitled **Estimation of Parameters in Conduction-Radiation Heat Transfer in Porous Media** by Vijay Kumar Mishra, a student of the Department of Mechanical Engineering, Indian Institute of Technology Guwahati, India, for the award of the degree of Doctor of Philosophy has been carried out under our supervision and that this work has not been submitted elsewhere for a degree.

Dr. Subhash C. Mishra
Professor
Department of Mechanical Engineering
Indian Institute of Technology Guwahati
Assam, India
May 2016

Dr. Dipankar Narayan Basu
Assistant Professor
Department of Mechanical Engineering
Indian Institute of Technology Guwahati
Assam, India
May 2016

Abstract

Development of thermal systems like a porous radiant burner, heat exchangers, insulations, etc., quantitative knowledge of heat and/or mass transfer, temperature field are essential. With geometric details, thermo-physical and optical properties, and initial and boundary conditions known, the desired results, viz., temperature and heat flux distributions are known by numerically solving a set of governing equations. However, when a thermal system is designed, a priori knowledge of some or all of the geometric parameters, and thermos-physical and optical properties of the material, and even initial and/or boundary conditions may not be known. Experimental route to optimize these parameters with trial and error approach for the desired outcome is not scientific. Recourse of an inverse analysis is the most preferred option by the scientific community. With thermo-physical properties and initial and boundary conditions known, calculations of the desired velocity field, temperature field or heat and mass flow rates, come under solving a direct problem. However, when either of the desired quantities (temperature, velocity fields, heat and mass transfer rates), and one or more of the properties or initial or boundary conditions are unknown, problem becomes an inverse one. In the direct problem, causes are known, and getting the outcomes are straightforward. On the contrary, in inverse problems, the outcome is known, but not the cause(s). Estimation of cause(s) is relatively, a difficult task. Mathematically, inverse problems are ill-posed. With even a slight variations in governing parameters, solution goes astray.

Over the last five decades, many researchers have studied heat and mass transfer in porous media. They have considered different geometric and thermal configurations. However, study on estimation of parameters in a combined mode conduction and radiation heat transfer with or without combustion is scarce. With its application in porous radiant burners in mind, the present work, is aimed at heat transfer analysis as well as estimation of thermo-physical and optical properties in a combined mode conduction and radiation heat transfer in porous media. With aforementioned objective in mind, in the present work, different configurations like single stage, two stage are considered. Different geometries like 1D planar, 2D rectangular, 2D axisymmetric cylindrical are also considered. Also, different optimization algorithms in the inverse analysis are used, such

as genetic algorithm, global search algorithm, pattern search algorithm, simulated annealing etc.

Acknowledgements

First and foremost, I would like to thank my advisor, Dr. Subhash C. Mishra and Dr. Dipankar Narayan Basu, for their exceptional guidance, expertise, and patience over the years. Their consistent encouragement has helped me make this thesis a work I can be truly proud of. I am immensely grateful to them for providing me with the opportunity to do this research and develop my skills in a field which has both fundamental scientific value and current practical relevance. I would also like to thank the members of my thesis committee: Dr. Manmohan Pandey, Dr. Dipankar Bandyopadhyay and Dr. Ganesh Natarajan, for their enthusiasm and support. I also take this opportunity to thank other faculty members of the Department of Mechanical Engineering for their blessings, encouragement and support.

I am thankful to all staff members of IIT Guwahati who helped me in different ways whenever I had any problem. Of course, none of this would have been possible without the love of my family. Their life-long support and encouragement has contributed so much to making me who I am, and I simply cannot thank them enough for everything they have done for me.

I would like to recognize the many friends I have made since coming to IIT for their camaraderie and their contributions intentional or otherwise to this thesis. I would like to thank Jai Manik, Raushan Kumar, Daya Shankar, Ramanuj Chauksey, Kalpo Jyoti Bora, Pankaj Kumar, Snehasish Panigrahy, Gyan Sagar Sinha, Dhrubajyoti Kashyap, Mantulal Basumatari, Mukesh Kumar, Chandrahas Patel, Jyoti Kumar Doley, A Srinivas Pavan Kumar, Ashif Iqbal, Vinod Yadav, Saptarshi Karmakar, Milan Krishna Singha Sarkar, Jitendra Kumar Patel, Sailen Dutta, Rajesh Ranjan, Vinod Pandey, Mukul Parmananda, Arnab Lahiri, Devavrat Kashyap and many others for all the Supreme times, and for likely extending the amount of time it took to complete the work contained in this thesis.

Vijay Kumar Mishra

May 2016

LIST OF PUBLICATIONS FROM THE WORK

International Journals:

1. V.K. Mishra, S.C. Mishra and D.N. Basu, Simultaneous estimation of parameters in analyzing porous medium combustion - Assessment of seven optimization tools, Numerical Heat Transfer, Part A (in press: DOI:10.1080/10407782.2016.1139908) 2016.
2. V.K. Mishra, S.C. Mishra and D.N. Basu , Simultaneous estimation of four parameters in a combined mode heat transfer in a 2-D rectangular porous matrix with heat generation, Numerical Heat Transfer, Part A (in press: DOI:10.1080/10407782.2016.1139910).
3. V.K. Mishra, S.C. Mishra and D.N. Basu, Simultaneous estimation of properties in a combined mode conduction- radiation heat transfer in a porous medium, Heat Transfer - Asian Research, DOI:10.1002/htj.21184 .
4. V.K. Mishra, S.C. Mishra and D.N. Basu, Combined mode conduction and radiation heat transfer in a porous medium and estimation of optical properties of the porous matrix, Numerical Heat Transfer, Part A, 67, 1119-1135, 2015.
5. V.K. Mishra, S.C. Mishra and D.N. Basu, Heat transfer characteristics of 2D-axisymmetric porous radiant burner, (Manuscript Prepared).
6. V.K. Mishra, S.C. Mishra and D.N. Basu, Simultaneous optimization of optical properties of a 2-D porous matrix in combined mode conduction and radiation heat transfer, (Manuscript Prepared).

International Conferences:

1. V.K. Mishra, S.C. Mishra and D.N. Basu, Combined mode conduction-radiation heat transfer in 2-D cylindrical porous medium and simultaneous estimation of its properties, 23rd National and 1st International ISHMT-ASTFE Heat and Mass Transfer Conference, Trivandrum, Kerala, India, 17 - 20 December 2015.
2. V.K. Mishra, S.C. Mishra and D.N. Basu , Simultaneous estimation of properties of a porous radiant burner, 23rd National and 1st International ISHMT-ASTFE

Heat and Mass Transfer Conference, Trivandrum, Kerala, India, 17 - 20 December 2015.

3. V.K. Mishra, S. C. Mishra and D.N. Basu, Estimation of a parameter in a combined mode heat transfer in a two layered 2D-axisymmetric porous matrix, 12th International Conference on Flow Dynamics, Sendai, Japan, 27 - 29 October 2015.
4. V.K. Mishra, S. C. Mishra and D.N. Basu, Combined mode conduction and radiation heat transfer in a 2-D porous medium and simultaneous estimation of its optical properties, 11th International Conference on Flow Dynamics, Sendai, Japan, 8 - 10 October 2014.
5. V.K. Mishra, S.C. Mishra and D.N. Basu, Heat transfer analysis combined with estimation of optical properties of a porous radiant burner, 22nd National and 11th ISHMT - ASME Heat and Mass Transfer Conference, IIT Kharagpur, 28 - 31 December 2013.

Contents

List of Figures

List of Tables

Nomenclature

A	-	surface area per unit volume of solid, $^{1}/_{\mathrm{m}}$
c	-	specific heat at constant pressure, $^{\mathrm{J}}/_{\mathrm{kg\times K}}$
d	-	pore diameter, m
G	-	incident radiation, $^{\mathrm{W}}/_{\mathrm{m^2}}$
h	-	heat transfer coefficient, $^{\mathrm{W}}/_{\mathrm{m^2\times K}}$
I	-	intensity, $^{\mathrm{W}}/_{\mathrm{m^2\times sr}}$
J	-	objective function
k	-	thermal conductivity, $^{\mathrm{W}}/_{\mathrm{m\times K}}$
L	-	thickness, m
M	-	number of effective intensities/directions
N	-	number of control volumes in computational domain
q_R	-	radiative heat flux, $^{\mathrm{W}}/_{\mathrm{m^2}}$
R	-	universal gas constant, $^{\mathrm{J}}/_{\mathrm{mol\,K}}$
S_{av}	-	average source term, $^{W}/_{\mathrm{m^2}}$
T	-	temperature, K
u	-	velocity, $^{\mathrm{m}}/_{\mathrm{s}}$
w	-	molecular weight, $^{\mathrm{kg}}/_{\mathrm{mol}}$

$\bar{W}$ - mixture averaged molecular weight, $^{kg}/_{mol}$

X_k - mole fraction of k_{th} species

Y_k - mass fraction of k_{th} species

x, y, z - coordinate, m

X, Y - length of the medium and breadth of the medium, m

Greek symbols

β - extinction coefficient, $^{1}/_{m}$

δ - polar angle, rad

ε - Emissivity

θ - non-dimensional temperature

ρ - density, $^{kg}/_{m^3}$

σ - Stefan-Boltzmann constant = $5.67\times10^{-8}\ ^{W}/_{m^2\times K^4}$

Ψ_R - non-dimensional radiative heat flux

Φ equivalence ratio

ϕ Porosity

$\dot{\omega}$ molecular generation rate, $^{mol}/_{m^3\ s^{-1}}$

ω - scattering albedo

Ω - solid angle, rad

Subscripts

B	-	Boundary
conv	-	Convective
E ,W	-	east, west
e	-	Exit
g	-	Gas
i	-	inlet
P	-	cell center
rad	-	Radiative
s	-	solid

Superscripts

j	-	index for direction
*	-	non-dimensional
~	-	exact

Chapter 1

INTRODUCTION

1.1 Introduction to Porous Media Combustion

Combustion is defined as the burning of a fuel and oxidant to produce heat and/or work [1, 2]. It is the major energy release mechanism in the Earth and key to humankind's existence. Combustion includes thermal, hydrodynamic, and chemical processes. It starts with the mixing of fuel and oxidant, and sometimes in the presence of other species or catalysts. The fuel can be gaseous, liquid, or solid and the mixture may be ignited with a heat source. When ignited, chemical reactions of fuel and oxidant take place and the heat release from the reaction creates a self-sustained process. The combustion products include heat, light, chemical species, pollutants, mechanical work, and plasma. Sometimes, a low-grade fuel, e.g., coal, biomass, or coke, can be partially burned to produce higher-grade fuel, e.g., methane. The partial burning process is called gasification. Various combustion systems, e.g., furnaces, combustors, boilers, reactors, and engines, are developed to utilize combustion heat, chemical species, and work.

For millennia, combustion-derived radiation has been used by civilization to warm themselves and their food, and to craft tools, vessels, armaments, artistic works, and everyday wares. Industry depends heavily upon radiant heating for many of its manufacturing processes. Driven by the desire for higher radiant heating rates and the need to emit minimal pollutants, interest in porous media combustion is growing. The porous media burners are characterized by high flame speeds, extended lean flammability limits, low emissions of pollutants (such as NOx and CO) and high radiant output [3 - 8].

The combustion of hydrocarbon fuels within a porous matrix involves stabilizing a reaction wave within the pore structure of the matrix. Conceptually, the most basic configuration resembles an enclosed flat flame burner (Fig. 1.1). Premixed fuel and air

enters the porous matrix where it is convectively heated as it passes through the interstitial voids in the matrix, the matrix material having been heated by radiation emitted upstream from the reaction zone, and by conduction through the solid matrix. The pre-heated fuel and air then pass to the reaction zone where the mixture is entrained under the influence of the local fluid mechanics, reaction occurs, and energy release takes place. The reacted products flow along a convoluted path through the porous matrix to the exit, convectively heating the material which radiates thermal energy to its surroundings.

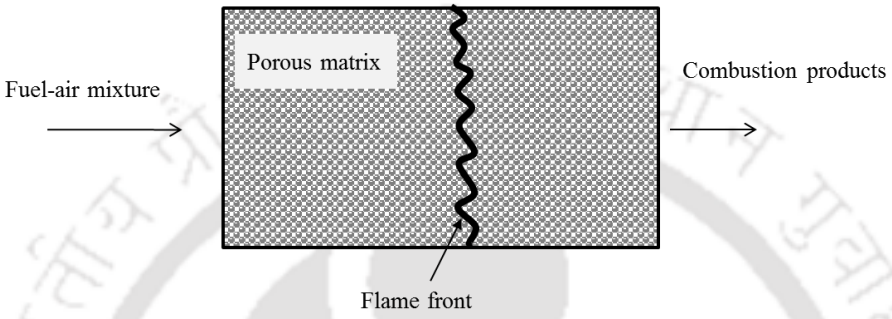

(a)

(b)

Figure 1.1: Combustion in porous media (a) Schematic of a basic configuration of porous burner (b) Heated surface of volumetric porous burner

The recirculation of energy from the combustion reaction is due to multiple thermal transport pathways. The dominant heat transfer mechanisms are [9-11]

- solid-solid radiation
- solid conduction within the porous matrix
- thermal convection between the solid and the gas phase

1.1.1 Material Design

Ceramic materials are more commonly used than metals in porous burners due to their higher temperature stability. Alumina (Al2O3), zirconia (ZrO2) and silicon carbide (SiC) based materials are most commonly used materials in porous burners. For a porous burner material, following properties are desirable [12]:

- durable, hard and chemical stability
- high thermal resistance
- manageable heat transfer properties
- good thermal shock performance

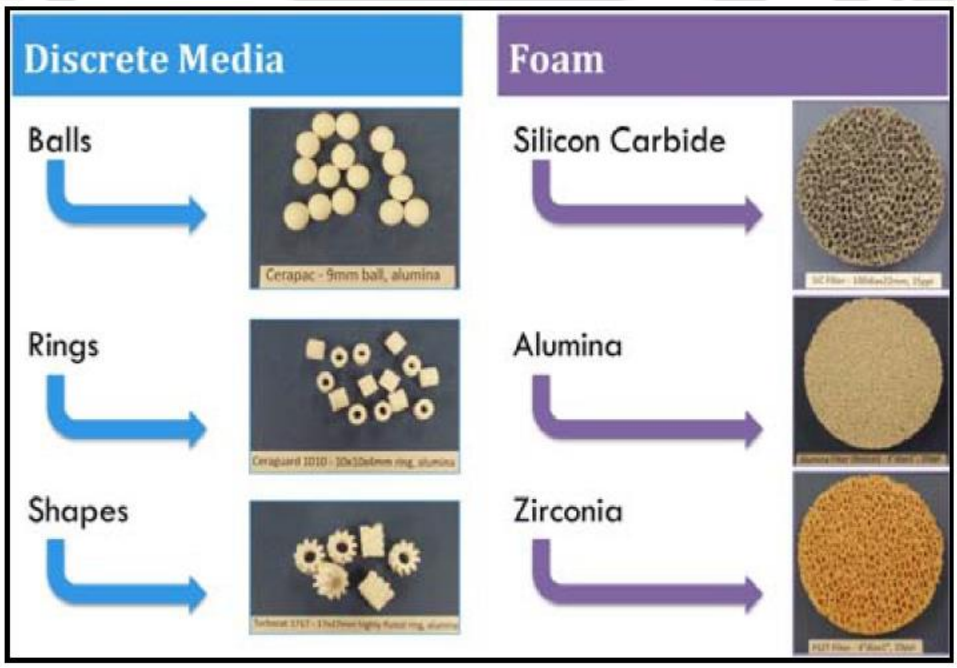

Figure 1.2: Summary of porous materials available

Porous burner materials are mainly used in discrete element form and cellular structures (Fig. 1.2). Ceramic balls, ceramic pebbles and ceramic saddles are the main discrete

element media used in porous burners. In cellular structures, ceramic foams are made in the form of fine interconnecting struts.

Various types of porous materials are commonly used in porous burners and they are shown in Fig. 1.2.

1.1.2 Applications

Due to advantages of combustion in porous media, it is finding applications in various fields like :

- IC Engine [13, 14]
- Gas turbines and propulsion [15, 16]
- Heat exchangers [17, 18]
- Oil and gas recovery [19, 20]
- Lighting [21]
- Hydrogen production [22, 23]

In IC engine the main problem of using PM is the formation of small particles due to thermal cycling and brittleness of the PM, which damages the IC engines. In heat exchanger, the fouling and dust accumulations are big problems. In Gas turbines and propulsion, the PM has a low elongation at break, a poor tensile strength and a high notch sensitivity. To obtain a material of low susceptibility to shocks and to the propagation of cracks initiated by the least defect, it is necessary to have a weak fiber-matrix bond. In that case, however, the material is not structurally strong since it is known that, to obtain composite materials with good mechanical properties, it is necessary to have a strong bond between the reinforcing texture and the matrix. Thermal and Chemical stability of PM, pose a problem in Hydrogen production. Such bottlenecks needs to be resolved before this technology can find wide spread acceptance.

1.2 Motivation

Performance of a porous radiant burner (PRB) is very sensitive to its thermo physical, optical, and geometric properties such as thermal conductivity, scattering albedo, and

porosity etc. Knowledge of these important parameters is very necessary for design of a PRB, and inverse analysis is an important engineering tool for the estimation of parameters. In the inverse analysis, an optimization algorithm is employed to minimize the objective function. The objective function to be fed to the optimization algorithm, is constructed using the known value of dependent variable like temperature distribution, heat flux etc. The dependent variable can be obtained by any means like experimentally measured, numerically computed or by analytic solution. The computed temperature and/or heat fluxes at the exit, based on the estimated values is fed into the objective function and the process is repeated until the objective function approaches its set minimum value.

1.3 Literature Review

The review is divided into two parts: experimental studies and numerical modeling of porous media; and the design optimization of combustion. Under the porous media part, various application of porous media followed by history of the concept of combustion in porous media is presented. Next, the development of the physical burner and attempts to model the burner will be reviewed. Then, the enhancements made to both the physical and model burner will be presented, followed by the studies on emission. Thereafter a review on research about the physical properties of the burner materials and the effect of those properties on performance is presented. At last, application of porous medium in wide variety of fields, followed by the design optimization section, will be presented.

1.3.1 Porous Media Studies

Porous media find extensive applications in thermal systems involving heat and mass transfer [24–28]. A wide range of thermal systems, such as compact heat exchangers, heat pipes, electronic cooling, solar collectors, and porous radiant burners (PRBs) use porous media for improving their thermal performance [24–28]. Approximately, a 50% increase in the value of Nusselt number was reported for laminar heat transfer through channels [26] imbedded with porous materials, whereas Naphon [27] predicted 25.9% higher thermal efficiency for solar air heaters. Compared to burners based on free-flame combustion, PRBs, in which combustion takes place within a radiating and conducting

porous matrix, have been reported to have high thermal efficiencies and low emissions of CO and NOx [29, 30–42]. The improved thermal performance with the utilization of a porous medium is attributed to its high surface area per unit volume for convection, and high thermal conductivity and emissivity of the porous matrix that enhances heat transfer by conduction and radiation, respectively [30–36].

Creating an excess enthalpy flame [43] motivated the research into porous media combustion. Weinberg [43] proposed that peak temperatures in excess of the adiabatic flame temperature could be attained by recirculating heat from the combustion products to the reactants. Hardesty and Weinberg [44] then hypothesized that the excess enthalpy flame would allow stable combustion of fuels having low energy content, but NOx concentrations may increase because the peak temperature of the burner exceeds the adiabatic flame temperature. To confirm the claim they constructed a burner, shown schematically in Fig. 1.3, comprising a counter-flow heat exchanger to provide the incoming reactants with the heat from the products. Results demonstrated that the peak temperature exceeded the adiabatic flame temperature.

Takeno and Sato [45] simplified the way heat could be transferred from the products to the reactants by placing a highly conductive solid into the flame to conduct the enthalpy of combustion upstream to the reactants. They modelled the problem as a laminar flame interacting with an isothermal solid. They concluded that increasing the flow rate would also increase the peak temperature as the reaction zone thinned, and the high peak temperature would have little effect on NOx due to short residence time of the gases in the high temperature zone. Using this model as the base, a lot of research was done to study the characteristics of the burner like, the stability of the flame front (Buckmaster and Takeno [46]), the effect of the length of the solid and heat loss (Takeno and Hase [47]), and an experimental study on the location and stability of the flame front (Kotani and Takeno [48]).

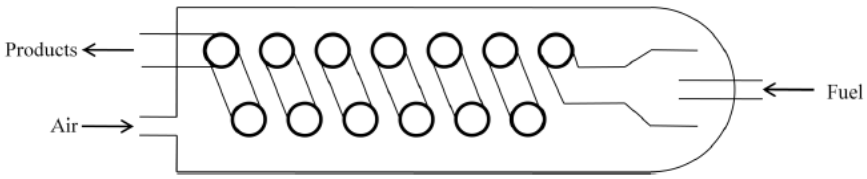

Figure 1.3 : Hardesty and Weinberg [44] Burner

Echigo et al. [49] explored the idea of using a porous media in place of a solid bar for heat recirculation. They simplified the problem by modeling it as one dimensional with spatially-dependant heat generation in place of detailed reaction kinetics, and scattering was omitted from the radiation equations. They were able to adequately match the results with the experimental data. Through experiments it was found that low energy content fuels could be burned in this type of burner, leading to the extension of the lean limit of combustion. This burner was more effective in heat recirculation due to radiative heat transfer, and thus motivating further research with proper attention to radiative heat transfer. Tong et al. [50] took care of the radiation using absorption and anisotropic scattering, and solved the radiative transfer equation (RTE) using the P-11 spherical harmonics approximation. They concluded that radiant output could be increased by increasing the optical thickness of the porous medium, and also by having a strongly backscattering medium.

After sufficiently understanding the radiative heat transfer in porous burner, improvement of combustion chemistry model became the goal of research. Hsu and Matthews [51] found that a single step chemistry mechanism over-predicted the peak flame temperature by five to twenty percent and also over predicted the burning rate. They also found that for equivalence ratios greater than 0.8, the porous media burner ceases to be an excess enthalpy flame.

The addition of a second stage of porous media was the next major development to porous burner technology (Hsu, Howell and Matthews [52]). They used the upstage porous section with small pores to allow for greater preheating and to also act as a flame arrester. The second stage has larger pores to accommodate the submerged flame.

Next step in the development of porous burner technology was to focus on emissions. Experimental studies were performed to determine the effect of flame speed and equivalence ratio on the emission levels of pollutants such as NOx and CO. Khanna et al. [53] experimented with pre-mixed methane and air and showed that the concentration of NOx increases with flame speed, due to the increase in peak temperature, while the concentration is relatively constant for a given equivalence ratio. They also showed that CO concentration increases with flame speed, as concentration are dependent on flame location and at faster speeds the flame is located near the end of the burner and does not have time to oxidize the CO into CO_2. The radiant output increases but the radiant thermal efficiency decreases with flame speed.

Barra et al. [54] studied the effect of equivalence ratio, solid conductivity, volumetric heat transfer coefficient, and extinction coefficient on the stable operating range of a two-stage porous ceramic burner. Increasing the equivalence ratio caused the stable operating range to shift to faster velocities as well as widen the range. The remainder of their tests were performed with an equivalence ratio of 0.65. For the solid conductivity four different cases were run with different combinations of solid conductivities in the upstream and downstream section of the burner. The best operating condition occurred when the second stage thermal conductivity was increased by a factor of ten which resulted in the stable range increasing by approximately a factor of two. For the volumetric heat transfer coefficient, three cases were carried out by altering the pore diameter in the Nusselt number correlation. The case where the pore diameter of the second stage was decreased by a factor of two resulted in the greatest effect on the operating range. The final set of tests was for the radiation extinction coefficient, which involved five cases. Increasing the first stage extinction coefficient by a factor of six yielded the best stable operating range.

More recently, Randrianalisoa et al. [55] attempted to find the porous radiant burner design attributes that minimized pollutant emissions, such as CO and NOx, while maximizing radiant power. For this study, a series of experiments were carried out to determine which material would be best in what situations. Two experiments for each material were performed; one at the high and one at the low range of the operating conditions for the desired burner. While no rigorous mathematical optimization was performed, their results are still enlightening. In terms of lowering pollutants, metallic

foams, such as FeCrAlY, were found to be best at both operating conditions. In terms of radiant power, on the other hand, Mullite foam was best for the low operating condition, but second worse for the high end, where FeCrAlY was the best choice. No conclusion was made about which material is best overall.

1.3.1.1 Work at IIT Guwahati

Application of PRB in domestic cooking stove has been explored at IIT Guwahati (Kakati et al.[54] and Pantangi et al. [55]). A wide range of smaller wattages and fuels like LPG, Kerosene etc. are tested (Sharma et al. [56] and Pantangi [57]). The efficiency, emission and energy cost for PRB are investigated (group of Mishra [58-60]). Increase in efficiency and decrease in emissions is observed (Mishra et al. [61]).

1.3.2 Optimization in Combustion Studies

Although the studies of Barra et al. [62] and Randrianalisoa et al. [63] show the general trends of the porous burner performance with material properties, these univariate parametric studies generally ignore the non-linear interactions that the properties have with each other. This is why design optimization is important; it considers all the variables and their interactions simultaneously, and identifies the combination of variables that provide the best possible solution.

Work on combustion and optimization was started by Smith et al. [64], who improved the design of coal gasification combustion while using a comprehensive model, through optimization. The objective was to maximize the cold gas efficiency of the burner by changing the pressure, oxygen/coal ratio, and steam/coal ratio. Two different injector designs were also considered: the first was a standard co-flow jet; while the second had swirl added to the coal stream. They employed response surface modelling (RSM) as optimization tool. The optimal efficiencies were found to be 84.86% for the co-flow burner and 82.74% for the burner with swirl; however, experimental verification was still ongoing and not provided. They also considered performing optimization on the coal gasification burner to maximize burnout, while keeping the NOx in the flue gas below 200ppm. The variables were the secondary swirl number, the variance of the particle size distribution, and the primary-to-secondary momentum ratio. Using the same techniques as the previous cases a solution to the problem was found, located on the constraint due to the competing nature of NOx concentration and burnout.

Correa and Smith [65] used design optimization to improve the operation of an ethylene furnace. Their objective was to bring the twelve coil outlet temperatures of the furnace closer to a desired temperature, thus creating a more uniform temperature field. The furnace was divided into two zones, with the coils in each zone receiving the same fuel flow rate, which were the design variables for this study. The furnace was modelled using a steady state, turbulent, incompressible reacting flow code, while the optimization was carried out using a quasi-Newton algorithm. A sixty percent improvement was made to the objective function. The burner was then divided into four zones, splitting the existing zones in half, to try and improve the objective function further, however no significant improvement was made.

Another study involving optimizing combustion devices was carried out on molten carbonate fuel cells (MCFC) (Gemmen [66]). The study involved designing a burner that could combust the excess fuel in MCFC's by injecting air into plug flow reactors (PFR). The objective function was to minimize the amount of hydrogen and carbon monoxide leaving the combustor, while the design variables were the amount of air going into each stage of the purposed combustor. The optimization, however, was carried out heuristically; the flow rate for one of the air injectors was perturbed slightly and then the other injector's flow rates were changed to ensure that the same total amount of air was injected for each iterate design. If the modified design was better than the current one then the modification becomes the new current design. This process was carried out until no significant improvement could be made. The final design reduced the amount of hydrogen and carbon monoxide to less than 1ppm at the burner exit. Although this method did lead to a design improvement, it is not true optimization since there is no guarantee of optimality; due to the heuristic nature, different answers can be reached depending on which iterates are selected, therefore the true minimum may not be found. Unfortunately, this procedure represents a very common type of "optimization" used today in industrial combustion.

A more rigorous method for optimizing combustion devices are genetic algorithms, which are based on biological processes. Several parent designs are selected from the design space and their objective value, or fitness, is calculated. Based on the principle of survival-of-the-fittest, the designs are then "bred" to produce new designs by mixing the

attributes of the parents. Mutation is also introduced during the "breeding" process by randomly perturbing a subset of variables. This process continues until the best design is found. In one study Büche et al. [67] used a genetic algorithm to minimize the amount of NOx produced and the amount of pulsation in the burner. The design variables were the fuel flow rates to eight different sections of the burner. Due to the competing nature of the objectives no true minimum was found, but a Pareto front did form where all designs along the front have an equal minimum value for the objective function. The design could then be chosen from this front based on the design needs of the engineer.

Finally, Catalano et al. [68] used progressive optimization to optimize the design of duct-burners. In progressive optimization, optimization is carried out concurrently with the solution to the combustion problem, so that when the problem is in its early stages of solving the combustion problem the optimization can be quite coarse since the "exact" optimum solution is not needed, while the optimization tolerance is reduced as the solver converges, thus saving computational effort. They performed two different optimizations: the first was to flatten the outlet temperature profile of the burner while changing the height of the slit form gap and the crosswise dimension of the flame-holder; and the second was to reduce the near-wall temperatures while altering the same variables as the previous study. Both tests were successful, and the combustion problem was only solved to convergence once, thereby causing a considerable time savings over regular optimization techniques.

Therefore it is evident that the thermal characterization of PRBs has received significant attention in research community. However, as was pointed out by Horsman and Daun [69], simple parametric analysis by varying a single parameter, while holding other constant, neglects the nonlinear interaction between parameters, apart from being very time-consuming. That necessitates design optimization, with simultaneous estimation of multiple parameters. Apart from the Response Surface Modeling approach of Horsman and Daun [69], hardly any optimization effort relevant to PRBs can be identified in open literature, and even the above work only adopt 1-D simulation. Inverse analysis has become a vital tool for engineers in selecting suitable material and ranges of operating parameters in numerous complicated heat transport systems [70 – 72]. Therefore, in order to optimize the design of a PRB according to the requirement, while taking care of the

multi-dimensional nature of the temperature distribution, present work focuses on the development of a numerical model of a 2-D axisymmetric PRB and simultaneous optimization of multiple parameters.

1.4 Objectives and Organization of the Thesis

Development of thermal systems like a porous radiant burner, heat exchangers, insulations, etc., quantitative knowledge of heat and/or mass transfer, temperature field are essential. With geometric details, thermo-physical and optical properties, and initial and boundary conditions known, the desired results, viz., temperature and heat flux distributions are known by numerically solving a set of governing equations. However, when a thermal system is designed, a priori knowledge of some or all of the geometric parameters, and thermos-physical and optical properties of the material, and even initial and/or boundary conditions may not be known. Experimental route to optimize these parameters with trial and error approach for the desired outcome is not scientific. Recourse of an inverse analysis is the most preferred option by the scientific community. With thermo-physical properties and initial and boundary conditions known, calculations of the desired velocity field, temperature field or heat and mass flow rates, come under solving a direct problem. However, when either of the desired quantities (temperature, velocity fields, heat and mass transfer rates), and one or more of the properties or initial or boundary conditions are unknown, problem becomes an inverse one. In the direct problem, causes are known, and getting the outcomes are straightforward. On the contrary, in inverse problems, the outcome is known, but not the cause(s). Estimation of cause(s) is relatively, a difficult task. Mathematically, inverse problems are ill-posed. With even a slight variations in governing parameters, solution goes astray.

Over the last five decades, many researchers have studied heat and mass transfer in porous media. They have considered different geometric and thermal configurations. However, study on estimation of parameters in a combined mode conduction and radiation heat transfer with or without a volumetric heat generation is scarce. With its application in porous radiant burners in mind, the present work, is aimed at heat transfer analyses as well as estimation of thermo-physical and optical properties in a combined mode conduction and radiation heat transfer in porous media. With aforementioned objective in mind, in the present work, seven problems pertaining to combined mode

conduction and radiation heat transfer with or without heat generation, and simultaneous estimation of thermos-physical and optical properties are reported. The geometry of the porous media considered are 1-D planar, 2-D rectangular and 2-D axisymmetric. In problems 1and 2, the geometry of the porous medium/media is 1-D planar. 2-D rectangular geometry of the porous matrix is considered in problem 3. In problem 4, the geometry considered is 2-D axisymmetric.

In problem 1, heat transfer in a 1-D planar porous medium with a localized volumetric heat generation zone is studied. Flow of air through the porous matrix gives rise to convection. Upstream of the heat generation zone, heat transfer is by conduction and radiation, and solid temperature is more than that of the gas. In the heat generation zone, and in the region downstream to it, conduction and radiation combined with advection raise the temperature of the gas, and heat transfer is from the gas to the solid. Distributions of gas- and solid-temperatures, for a range of governing parameters are studied. Distributions of conductive, convective and radiative heat fluxes for both gas- and solid-phases are analyzed. With volumetric radiative information needed in the solid-phase energy equation computed using the discrete transfer method, the gas-phase and the solid-phase energy equations are solved using the finite difference method. Two of the three optical properties, i.e. extinction coefficient β , scattering albedo ω and exit emissivity ε_e are simultaneously estimated at a time. In the estimation of parameters, the objective function is analyzed using the genetic algorithm. Effect of number of generations, population size, mutation probability and crossover probability on accuracy of estimation and CPU time are reported. Effect of the measurement errors on accuracy of results is considered. Then in second part, simultaneous estimation of three parameters are reported in problem 1. Parameters considered are solid conductivity P_4, scattering albedo ω, and exit emissivity ε_e. Effectiveness in terms of CPU time and accuracy of genetic algorithm and global search algorithm is reported. Global search algorithm is found to have an edge over the genetic algorithm.

In many porous radiant burners, a two-layer porous matrix is used. The layer 1, preheats the incoming air-fuel mixture, and combustion starting at the interface of the two layers, and remains submerged in the second layer. With CH_4 as the fuel, problem 2 deals with

its combustion in a two-layer porous matrix. CH_4 combustion is analyzed using single-step global mechanism. Like problem 1, the radiative information (the divergence of radiative heat flux) needed in the solid-phase energy equation is computed using the discrete transfer method, and the energy equations are simultaneously solved using the finite difference method. Three parameters, viz., gas velocity, scattering albedo and downstream pore diameter are simultaneously estimated. In this problem efficacies of 7 optimization tools, viz., genetic algorithm, the genetic algorithm parallel, the simulated annealing, the multiple starting point algorithm parallel, the pattern search algorithm, pattern search algorithm parallel and the global search algorithm, in terms of accuracy and CPU time are assessed. Pattern search algorithm is found to be the best.

Having studied combined mode heat transfer in a single as well as a two-layer 1-D planar porous matrix, and examined the effectiveness of optimization tools in simultaneous estimation of 2-3 parameters in problems 1 and 2, 2-D rectangular porous matrix with a centrally localized volumetric heat generation zone is considered in problem 3. Here finite volume method is used to compute the radiative information needed for the solid-phase energy equation. Governing equations for the solid- and gas-phase are solved using Gauss-Seidel iterative method. In problem 3, results of detailed heat transfer analysis are provided. In later part of problem 3, simultaneous estimation of four parameters, viz., the scattering albedo, the emissivity, the solid conductivity and the heat transfer coefficient are simultaneously estimated. Efficacy of the genetic algorithm and global search algorithm are considered. Global search algorithm is found to be superior than the genetic algorithm. In applications like cooking stoves, porous radiant burners have cylindrical geometry. Problem 4 pertain to analyses of combined mode heat transfer and estimations of parameters in 2-D axisymmetric 2-layer porous matrix. Finite volume method is used to compute the volumetric radiative information required in the solid-phase energy equation. The solid-phase and gas-phase energy equations are also solved using the finite volume method. In problem 4, volumetric heat source is the combustion of CH_4. It is simulated using single-step global mechanism. Effectiveness of the genetic algorithm, global search algorithm and pattern search algorithm in simultaneous estimation of downstream pore diameter and equivalence ratio are assessed. Patten search algorithm yields the best estimation, and it also has computational advantage over others. With brief

descriptions of seven problems considered presented before, in the following, organization of the thesis is presented.

The thesis is organized in 7 chapters. In Chapter 1, titled Introduction, the need for analyzing combined mode heat transfer, and simultaneous estimation of parameters is justified first. Important studies relevant to the present work by researchers are revived next. Based on the literature review, objectives for the present work are laid out at the end.

In the second chapter, a general methodology is presented for the solution of a combined mode conduction and radiation heat transfer problem in a conducting, convecting and radiating porous matrix. Temperatures of gas and solid need not be the same in heat transfer in a porous matrix. To account for this non-local thermal equilibrium, separate energy equations for the gas- and the solid-phase are considered. The two equations are coupled through a convective term. The gas being transparent to thermal radiation, volumetric radiative source term appears only in the solid-phase energy equation. In 1-D planar porous medium, discrete transfer method is used to compute the radiative information. In 2-D rectangular and 2-D axisymmetric porous geometry, the same is calculated using the finite volume method. Formulation details of the discrete transfer method and the finite volume method are provided in this chapter 2. Solution details of energy equations in 1-D, 2-D rectangular and 2-D axisymmetric geometry are provided at the end.

Results of problem 1 are presented and physically analyzed in Chapter 3. Heat transfer analysis and parameter estimation in combined mode heat transfer in 1-D planar porous medium which are covered in problem 2 are reported in Chapter 4. Chapter 5 contains details of problem 3 and its results and discussion. Chapter 6 contain results of problem 4. Finally in Chapter 7, overall conclusions of the entire study, and scope for the future work are presented

1.5 Summary

Combustion in porous media is a technology with very promising solutions of present society problems like, environmental concerns and depleting fossil fuels reserves. Different porous materials with various strength and weakness' are finding its use in

porous radiant burners. Due to its advantages, it finds applications in wide variety of fields. The present porous burner technology is a result of research that taken place over the last four decade. The concept that started with the insertion of a highly conductive solid into the flame and finally developed into a multi-staged porous ceramic burner with a submerged flame. Further improvement in the design of these burners have been explored through parametric studies and trial and error path, which ignores the non-linear coupling effects of the equations. They have considered different geometric and thermal configurations. However, study on estimation of parameters in a combined mode conduction and radiation heat transfer with or without a volumetric heat generation is scarce. With its application in porous radiant burners in mind, the present work, is aimed at heat transfer analyses as well as estimation of thermo-physical and optical properties in a combined mode conduction and radiation heat transfer in porous media.

Chapter 2

NUMERICAL METHODOLOGY FOR COMBINED-MODE PROBLEMS

2.1 Introduction

In a heat transfer problem involving thermal radiation, owing to the volumetric nature of the phenomenon, solution of the relevant equation of energy conservation is quite intricate, in comparison to its conventional version [74, 75]. The medium properties and associated initial and boundary conditions are typically known. Then the theoretical framework reduces to the determination of the temperature and/or heat flux distribution, which can be cited as the example of a direct problem. It is generally mathematically well-posed. An inverse problem, on the contrary, is mathematically ill-posed, invariably requiring the adoption of some kind of regularization or optimization procedure, along with some method(s) to solve the direct problem itself [76, 77].

Present chapter details the mathematical formulation developed for the solution of an inverse transient conduction-radiation heat transfer problem. Finite difference method (FDM) is employed in constructing the discrete version of the governing energy equation, whereas either the finite volume method (FVM) or the discrete transfer method (DTM) is used to compute the radiative information. Different optimization tools have their own advantages, and hence several of them are attempted with to recognize the most suitable one for a specific situation. In the following sections, the mathematical formulation of FDM for energy equation and FVM/DTM for RTE are discussed in respect to the direct problem. Subsequently the methodology adopted for solving the inverse problem is deliberated with.

2.2 Conservation of Energy

The general form of energy conservation equation, with the assumption of constant thermophysical properties involving steady state conduction-radiation problem with gas flow can be written as ,

$$\phi\rho cu\frac{\partial T}{\partial z} = k\nabla^2 T - \nabla\cdot\vec{q}_R \tag{2.1}$$

The first term is convective term which takes care of heat transfer due to bulk motion of fluid. The divergence of radiative heat flux $\nabla.\vec{q}_R$ is computed using the discrete transfer method (DTM) or the finite volume method (FVM). Formulation for both the DTM and the FVM are discussed systematically in the following sections with the assumptions considered for the problem.

2.2.1 Assumptions

a) Transient terms in all the equations are neglected.
b) Working gas is nonradiating and behave as ideal gases.
c) Thermo-physical properties of the gas and the solid phase are constant over the range of temperature considered in this study.
d) Catalytic effects of the high temperature solid are negligible.
e) The permeability of the porous matrix is so large that the pressure drops because of interaction of gas with the matrix is negligible.

2.3 Discrete Transfer Method (DTM)

Discrete transfer method, proposed by Shah and coworkers [78, 79] requires the calculation of the radiative heat flux and involves the tracing of representative rays from one surface to another throughout the domain of interest. Every bounding control surface is viewed to be the source of a number of rays, which divide the hemisphere about a grid point into the same number of equal solid angles. The discretized version of the RTE needs to be solved to estimate the intensity distribution along each such rays.

The divergence of the radiative heat flux can be expressed as,

$$\nabla\cdot\vec{q}_R = (1-\omega)\beta\left(4\sigma T^4 - G\right) \tag{2.2}$$

Radiation can be considered to be azimuthally symmetric in a 1-D planar geometry. Accordingly the incident radiation can numerically be computed as,

$$G = 2\pi \int_{\alpha=0}^{2\pi} I(\alpha)\sin\alpha\, d\alpha \approx 4\pi \sum_{m=1}^{M} I^m \sin\alpha^m \sin\left(\frac{\Delta\alpha}{2}\right) \tag{2.3}$$

where M is the selected number of discrete divisions of width $\Delta\alpha\left(=\frac{\pi}{M}\right)$ in the polar space $0 \le \alpha \le \pi$, and I^m is the discrete intensity averaged over a division with polar angle as $\left(m-\frac{1}{2}\right)\Delta\alpha$. Fig. 2.1 illustrates this with 4 token intensities for two different sample control volumes.

Following the DTM formulation, m, the intensity I_D^m at any downstream location is computed in terms of the upstream intensity I_U^m and the average source term S_{av} as,

$$I_D = I_U \exp(-\beta ds) + S_{av}\left[1-\exp(-\beta ds)\right] \tag{2.4}$$

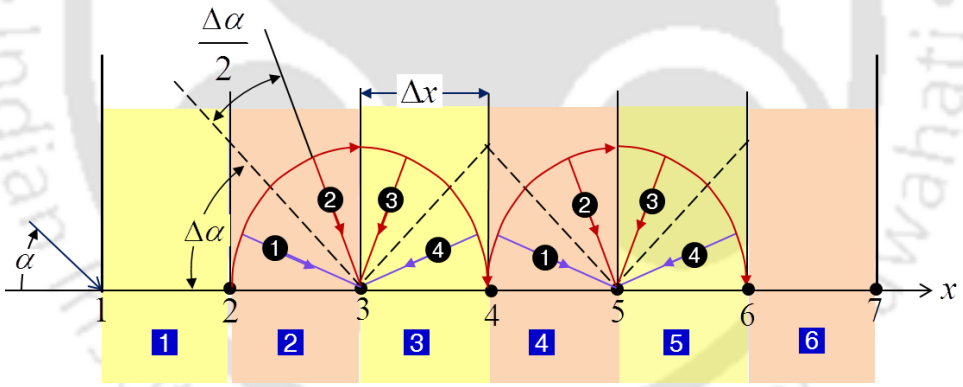

Figure 2.1. Ray tracing in the DTM.

where $ds = \frac{dx}{|\cos\alpha|}$ is the distance between the upstream and downstream nodes and $S_{av} = \frac{S_U + S_D}{2}$ is the source term averaged over two nodes. Here the grid points are the interface of the two control volumes and the upstream and downstream nodes are identified based on the marching directions, i.e., from west to east for $0 \le \alpha \le \frac{\pi}{2}$ or from

east to west for $\frac{\pi}{2} \le \alpha \le \pi$. With reference to Fig. 2.1, for the two token intensities (1, 2) shown in the polar space $0 \le \alpha \le \frac{\pi}{2}$ that are eastbound, $S_{av} = \frac{S_2 + S_3}{2}$,; while for the intensities 3 and 4 in the polar space $\frac{\pi}{2} \le \alpha \le \pi$ that are westbound, $S_{av} = \frac{S_3 + S_4}{2}$. If the scattering is isotropic, the source term S is given by

$$S(x) = (1-\omega)\beta \frac{\sigma T^4}{\pi} + \left(\frac{\omega\beta}{4\pi}\right) G \tag{2.5}$$

2.4 Finite Volume Method (FVM) in Cartesian Co-ordinate

The methodology of computing the radiative information using the FVM was initially formulated by Raithbay and Chui [80], and was subsequently modified and proposed by Chai and coworkers [81, 82]. The FVM involves exact integration over both spatial control volume and the solid angle in the angular direction. Because there is no loss of radiative information, the FVM methodology is fully conservative. The details of the FVM formulation is presented below employing the coordinate system shown in Fig. 2.2. The two dimensional geometry is divide into a number of control volumes. The angular domain is discretized into control angles.

The radiative transfer equation (RTE) governing the radiative energy balance for the intensity field in an absorbing, emitting and scattering medium is given by,

$$I(s+ds,\Omega) - I(s,\Omega) \equiv \frac{\partial I}{\partial s} ds = \kappa I_b(s) ds - \kappa I(s,\Omega) ds - \sigma_s I_b(s,\Omega) ds + \left(\frac{\sigma_s}{4\pi}\right) \int_{\Omega'=4\pi} I(s,\Omega') p(\Omega' \to \Omega) d\Omega' \tag{2.6}$$

where, Ω represents direction, I_b is the boundary intensity, and $d\Omega'$ is the elemental solid angle. This particular equation can be re-written as,

$$\frac{dI(s,\Omega)}{ds} = \kappa I_b(s) - \beta I(s,\Omega) + \left(\frac{\sigma_s}{4\pi}\right) \int_{\Omega'=4\pi} I(s,\Omega') p(\Omega' \to \Omega) d\Omega' \tag{2.7}$$

where $\beta = \kappa + \sigma$, is the effective extinction coefficient of the medium.

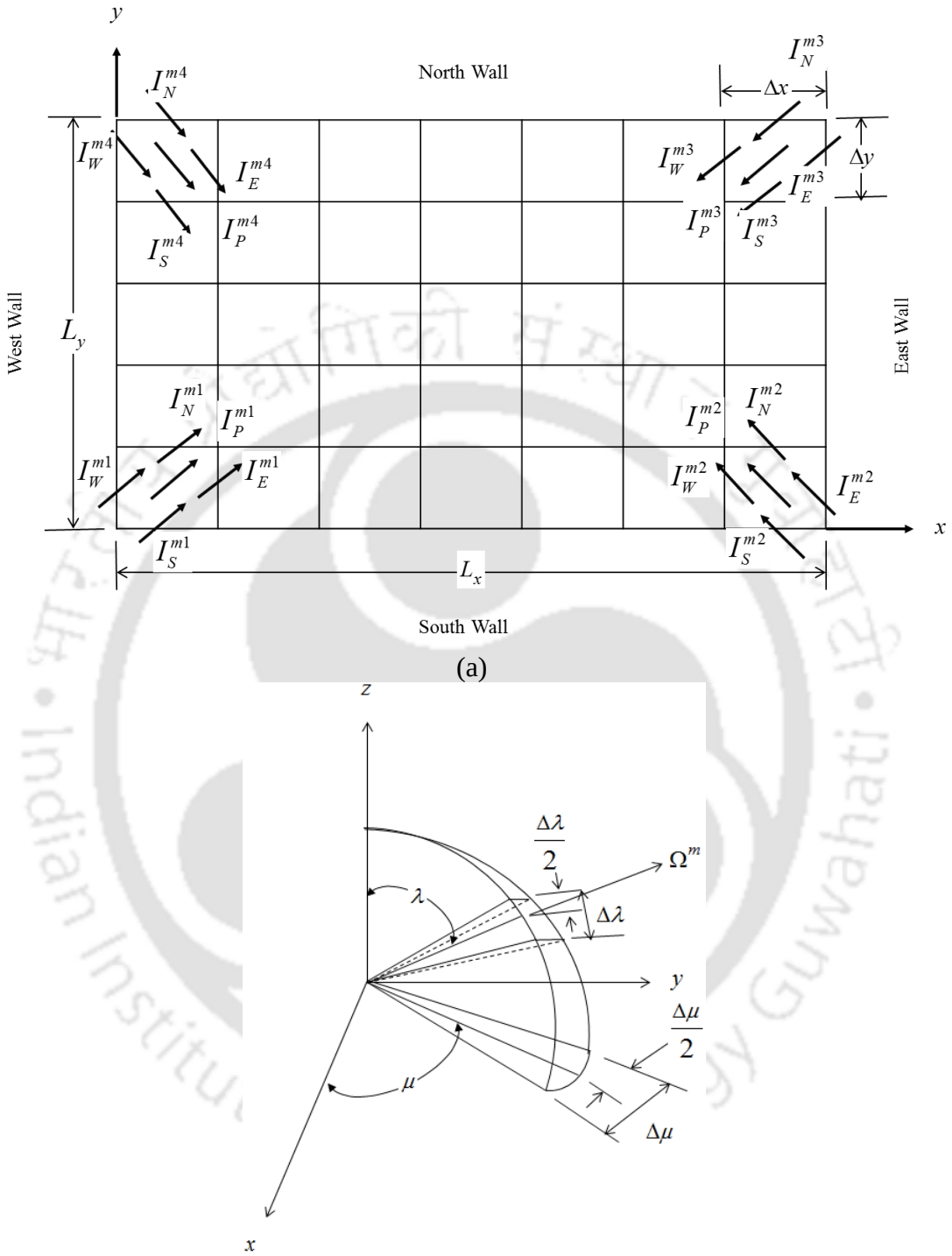

Figure 2.2. (a) Schematic of a 2D rectangular cavity, (b) ray tracing in the FVM

Eq. (2.7) can be converted to the differential form of RTE for any direction $\hat{s}$ and for any solid angle Ω about an elemental solid angle $d\Omega$ is given by,

$$\frac{dI}{ds} = -\beta I + S \tag{2.8}$$

where S is the source term which is given by,

$$S = \kappa\left(\frac{\sigma T^4}{\pi}\right) + \frac{\sigma_s}{4\pi}\int_{\Omega'=4\pi} I(\Omega')\Phi(\Omega,\Omega')\,d\Omega' \tag{2.9}$$

Resolving Eq. (2.8) (Fig. 2.2b) along the Cartesian coordinate and integrating it over the elemental solid-angle $\Delta\Omega^j$,

$$\frac{\partial I^j}{\partial x}D_x^j + \frac{\partial I^j}{\partial y}D_y^j + \frac{\partial I^j}{\partial z}D_z^j = -\beta I^j \Delta\Omega^j + S^j\Delta\Omega^j \tag{2.10}$$

If $\hat{n}$ is the outward normal to a surface, then D^j is given by,

$$D^j = \int_{\Delta\Omega^j}\left(\hat{n}.\hat{s}^j\right)d\Omega \tag{2.11}$$

where the direction $\hat{s}^j = \left(\sin\lambda^j\cos\mu^j\right)\hat{i} + \left(\sin\lambda^j\sin\mu^j\right)\hat{j} + \left(\cos\lambda^j\right)\hat{k}$. When $\hat{n}$ is pointing towards one of the positive coordinate directions, D_x^j, D_y^j and D_z^j are given as,

$$D_x^j = \int_{\Delta\Omega^j}\sin\lambda\cos\mu\,d\Omega = \int_{\mu^j-\frac{\Delta\mu^j}{2}}^{\mu^j+\frac{\Delta\mu^j}{2}}\int_{\lambda^j-\frac{\Delta\lambda^j}{2}}^{\lambda^j-\frac{\Delta\lambda^j}{2}}\cos\mu\sin^2\lambda\,d\lambda\,d\mu$$
$$= \cos\mu^j\sin\left(\frac{\Delta\mu^j}{2}\right)\left[\Delta\lambda^j - \cos 2\lambda^j\sin(\Delta\lambda^j)\right] \tag{2.12a}$$

$$D_y^j = \int_{\Delta\Omega^j}\sin\mu\sin\phi\,d\Omega = \int_{\mu^j-\frac{\Delta\mu^j}{2}}^{\mu^j+\frac{\Delta\mu^j}{2}}\int_{\lambda^j-\frac{\Delta\lambda^j}{2}}^{\lambda^j-\frac{\Delta\lambda^j}{2}}\sin\mu\sin^2\lambda\,d\lambda\,d\mu$$
$$= \sin\mu^j\sin\left(\frac{\Delta\mu^j}{2}\right)\left[\Delta\lambda^j - \cos 2\lambda^j\sin(\Delta\lambda^j)\right] \tag{2.12b}$$

$$D_z^j = \int_{\Delta\Omega^j}\cos\lambda\,d\Omega = \int_{\mu^j-\frac{\Delta\mu^j}{2}}^{\mu^j+\frac{\Delta\mu^j}{2}}\int_{\lambda^j-\frac{\Delta\lambda^j}{2}}^{\lambda^j-\frac{\Delta\lambda^j}{2}}\cos\lambda\sin\lambda\,d\lambda\,d\mu = \sin\lambda^j\cos\lambda^j\sin\left(\Delta\lambda^j\right)\Delta\mu^j \tag{2.12c}$$

For $\hat{n}$ pointing towards the negative coordinate directions, signs of D_x^j, D_y^j and D_z^j are reversed. In Eq. (2.10), $\Delta\Omega^j$ is given by,

$$\Delta\Omega^j = \int_{\Delta\Omega^j} d\Omega = \int_{\mu^j-\frac{\Delta\mu^j}{2}}^{\mu^j+\frac{\Delta\mu^j}{2}} \int_{\lambda^j-\frac{\lambda^j}{2}}^{\lambda^j+\frac{\lambda^j}{2}} \sin\lambda d\lambda d\mu = 2\sin\lambda^j \sin\left(\frac{\Delta\lambda^j}{2}\right)\Delta\mu^j \qquad (2.13)$$

Integrating Eq. (2.10) over control volume following the concept of FVM,

$$\left[I_E^j - I_W^j\right]A_{EW}D_x^j + \left[I_N^j - I_S^j\right]A_{NS}D_y^j + \left[I_F^j - I_B^j\right]A_{FB}D_z^j = \left[-\beta V I_P^j\right]\Delta\Omega^j \qquad (2.14)$$

where A_{EW}, A_{NS} and A_{FB} are the areas of the *x*-, *y*- and *z*-faces of a 3-D control volume, respectively. In Eq. (2.14), I with suffixes E, W, N, S, F and B designate intensities averaged over the east, west, north, south, front and back control surfaces respectively. On the right-hand side of Eq. (2.14), $V = dx \times dy \times dz$ is the volume of the cell, and I_P^j and S_P^j are the intensities and source terms at the cell centre P, respectively.

In any discrete direction Ω^j, if a linear relationship among the two cell-surface intensities and cell-centre intensity I_P^j is assumed, then

$$I_P^j = \chi_x I_E^j + (1-\chi_x) I_W^j = \chi_y I_N^j + (1-\chi_y) I_S^j = \chi_z I_F^j + (1-\chi_z) I_B^j \qquad (2.15)$$

Here χ is the finite-difference weighting factor and its value is normally considered to be 0.5. While marching from the first octant of a 3-D enclosure, for which D_x^j, D_y^j and D_z^j are all positive, I_P^j in terms of known cell-surface intensities can be written as,

$$I_P^m = \frac{\frac{D_x^j A_{EW}}{\chi_x} I_W^j + \frac{D_y^j A_{NS}}{\chi_y} I_S^j + \frac{D_z^j A_{FB}}{\chi_z} I_B^j + \left(V\Delta\Omega^j\right) S_P^j}{\frac{D_x^j A_E}{\chi_x} + \frac{D_y^j A_N}{\chi_y} + \frac{D_z^j A_F}{\chi_z} + \beta V \Delta\Omega^j} \qquad (2.16)$$

where the averaged areas can be expressed as,

$$A_{E,W} = (1-\chi_x)A_E + \chi_x A_W,\ A_{NS} = (1-\chi_y)A_N + \chi_y A_S,\ A_{FB} = (1-\chi_z)A_F + \chi_y A_B \qquad (2.17)$$

If any one of the D_x^j, D_y^j or D_z^j is negative, marching needs to start from the other corner of the computational domain. Correspondingly a general expression of I_P^j in terms of the known intensities and source term can be constructed as,

$$I_P^j = \frac{\frac{\left|D_x^j\right| A_x}{\chi_x} I_{xi}^j + \frac{\left|D_y^j\right| A_y}{\chi_y} I_{yi}^j + \frac{\left|D_z^j\right| A_z}{\chi_z} I_{zi}^j + \left(V \Delta\Omega^j\right) S_P^j}{\frac{\left|D_x^j\right| A_E}{\chi_x} + \frac{\left|D_y^j\right| A_N}{\chi_y} + \frac{\left|D_z^j\right| A_F}{\chi_z} + \beta V \Delta\Omega^j} \tag{2.18}$$

Here x_i, y_i and z_i are the suffixes over I^j for the intensities entering the control volume through *x*-, *y*- and *z*-faces respectively and the averaged areas are given as,

$$A_x = \left(1-\chi_x\right) A_{x_e} + \chi_x A_{x_i}, A_y = \left(1-\chi_y\right) A_{y_e} + \chi_y A_{y_i} = A_z = \left(1-\chi_z\right) A_{z_e} + \chi_z A_{z_i} \tag{2.19}$$

Here A with suffixes x_i, y_i and z_i represent control surface areas through which intensities enter the control volume, while A with suffixes x_e, y_e and z_e represent control surface areas through which intensities leave the control volume.

Therefore, for a 1-D control volume, the cell-center intensity can be expressed as ,

$$I_P^j = \begin{cases} \dfrac{2D_x^j I_W^j + S_P^j \Delta\Omega^j dx}{2D_x^j + \beta \Delta\Omega^j dx}, & D_x^j > 0 \\ \dfrac{2\left|D_x^j\right| I_E^j + S_P^j \Delta\Omega^j dx}{2\left|D_x^j\right| + \beta \Delta\Omega^j dx}, & D_x^j < 0 \end{cases} \tag{2.20}$$

Similarly, for a 2-D control volume, four possible forms of the cell-center intensity can be summarized as,

$$I_P^j = \frac{2D_x^j A_x I_W^j + 2D_y^j A_y I_S^j + \left(V \Delta\Omega^j\right) S_P^j}{2D_x^j A_x + 2D_y^j A_y + \beta V \Delta\Omega^j}, \text{ 1st quadrant: } D_x^j > 0, \; D_y^j > 0 \tag{2.21a}$$

$$I_P^j = \frac{2\left|D_x^j\right| A_x I_E^j + 2D_y^j A_y I_N^j + \left(V \Delta\Omega^j\right) S_P^j}{2\left|D_x^j\right| A_x + 2D_y^j A_y + \beta V \Delta\Omega^j}, \text{ 2nd quadrant: } D_x^j < 0, \; D_y^j > 0 \tag{2.22b}$$

$$I_P^j = \frac{2\left|D_x^j\right| A_x I_E^j + 2\left|D_y^j\right| A_y I_N^j + \left(V\Delta\Omega^j\right) S_P^j}{2\left|D_x^j\right| A_x + 2\left|D_y^j\right| A_y + \beta V \Delta\Omega^j}, \text{ 3rd quadrant: } D_x^j < 0,\ D_y^j < 0 \qquad (2.23c)$$

$$I_P^j = \frac{2D_x^j A_x I_W^j + 2\left|D_y^j\right| A_y I_N^j + \left(V\Delta\Omega^j\right) S_P^j}{2D_x^j A_x + 2\left|D_y^j\right| A_y + \beta V \Delta\Omega^j}, \text{ 4th quadrant: } D_x^j > 0,\ D_y^j < 0 \qquad (2.24d)$$

For a linear anisotropic phase function $\Phi\left(\Omega,\Omega'\right) = 1 + a\cos\lambda\cos\lambda'$, the source term S at any location $\vec{r}$ is given as,

$$S = \kappa_a\left(\frac{\sigma T^4}{\pi}\right) + \left(\frac{\sigma_S}{4\pi}\right)\int_0^{2\pi}\int_0^{\pi} I\left(\lambda',\mu'\right)\left(1 + a\cos\lambda\cos\lambda'\right)\sin\lambda' d\lambda' d\mu' \qquad (2.25)$$

Modifying it in terms of the incident radiation and net radiative heat flux,

$$S = \left(\frac{\sigma_S}{4\pi}\right)\left[G + a\cos\lambda q_R\right] \qquad (2.26)$$

Discretizing the complete span of polar angle $\left(0 \le \lambda \le \pi\right)$ and azimuthal angle $\left(0 \le \mu \le 2\pi\right)$, by M_λ and M_μ number of discrete points respectively, and hence a total $M_\lambda \times M_\mu$ number of discrete directions for intensities at any point, the incident radiation can numerically be computed in FVM as,

$$\begin{aligned} G &= \int_{\Omega=0}^{4\pi} I\left(\Omega\right) d\Omega = \int_{\mu=0}^{2\pi}\int_{\lambda=0}^{\pi} I\left(\lambda,\mu\right)\sin\lambda d\lambda d\mu \\ &\approx \sum_{k=1}^{M_\mu}\sum_{l=1}^{M_\lambda} I^m\left(\lambda_l^m,\mu_k^m\right) 2\sin\lambda_l^m \sin\left(\frac{\Delta\lambda}{2}\right)\Delta\mu_k^m \end{aligned} \qquad (2.27)$$

Similarly the net radiative heat flux can be computed as,

$$\begin{aligned} q_R &= \int_{\Omega=0}^{4\pi} I\left(\Omega\right)\cos\lambda d\Omega = \int_{\mu=0}^{2\pi}\int_{\lambda=0}^{\pi} I\left(\lambda,\mu\right)\cos\lambda\sin\lambda d\lambda d\mu \\ &\approx \sum_{k=1}^{M_\mu}\sum_{l=1}^{M_\delta} I^m\left(\lambda_l^m,\mu_k^m\right) 2\sin\lambda_l^m \cos\lambda_l^m \sin\left(\Delta\lambda_l^m\right)\Delta\mu_k^m \end{aligned} \qquad (2.28)$$

Radiation being azimuthally symmetric for a 1-D planar geometry, above two equations can be simplified as,

$$G = 2\pi \int_{\lambda=0}^{\pi} I \sin\lambda d\lambda \approx 4\pi \sum_{j=1}^{M} I^j \sin\lambda^j \sin\left(\frac{\Delta\lambda^j}{2}\right) \quad (2.29)$$

$$q_R = 2\pi \int_{\lambda=0}^{\pi} I \cos\lambda \sin\lambda d\lambda \approx 2\pi \sum_{j=1}^{M} I^j \sin\lambda^j \cos\lambda^j \sin\left(\Delta\lambda^j\right) \quad (2.30)$$

The knowledge of boundary intensity is required to evaluate Eq. (2.30), while marching from any of the corners. For a diffuse-gray boundary/wall with temperature T_b and emissivity ε_b, the boundary intensity I_b is computed from ,

$$I_b = \frac{\varepsilon_b \sigma T_b^4}{\pi} + \left(\frac{1-\varepsilon_b}{\pi}\right) \sum_{k=1}^{M\mu} \sum_{l=1}^{M_\lambda/2} I^m\left(\lambda_l^m, \mu_k^m\right) \sin\lambda_l^m \cos\lambda_l^m \sin\Delta\lambda_l^m \Delta\mu_k^m \quad (2.31)$$

The two terms on the right-hand side of Eq. (2.31) represent the emitted and reflected components of the boundary intensity respectively. With the knowledge of intensity distribution, radiative information $\nabla.\vec{q}_R$ required for Eq. (2.1) can finally be computed as,

$$\nabla.\vec{q}_r = \beta(1-\omega)\left(4\pi \frac{\sigma T^4}{\pi} - G\right) \quad (2.32)$$

where $\omega = \frac{\sigma_s}{\beta}$ is the scattering albedo.

2.5 Finite Volume Method in Cylindrical Coordinate

For a radiatively active medium inside a cylindrical enclosure as shown in Fig. 2.3, the radiative heat flux is defined as [83, 84],

$$q_r^R = \int_{\Omega=4\pi} I(\vec{r},\vec{s})(\vec{s}.\vec{e}_r) d\Omega \quad 2.33$$

where $I(\vec{r},\vec{s})$ is the radiative intensity at position $\vec{r} = \vec{e}_r r + \vec{e}_{\alpha 0}\alpha_0 + \vec{e}_z z$ in the direction $\vec{s} = \vec{e}_r \sin\theta\cos\alpha + \vec{e}_{\alpha 0} \sin\theta\sin\alpha + \vec{e}_z \cos\theta$, and $d\Omega = \sin\theta\, d\theta\, d\alpha$ is the solid angle. The spatial (r, α_0, z) and angular (θ, α) coordinates are selected and

defined here based on the cylindrical base vectors $\vec{e}_r, \vec{e}_{\alpha 0}$, and $\vec{e}_r$. In this case, since the direction of $\vec{e}_r$ and $\vec{e}_{\alpha 0}$ changes as the spatial azimuthal angle α_0 changes, the direction $\vec{s}$ defined by a set of (θ, α) changes as α_0 changes as shown in Fig. 2.4. Therefore, it can be found that the angular azimuthal angles, α and α_Ω, defined relative to cylindrical and Cartesian coordinates, respectively, are related to the spatial azimuthal angle, α_0 through the relation of $\alpha = \alpha_\Omega - \alpha_0$.

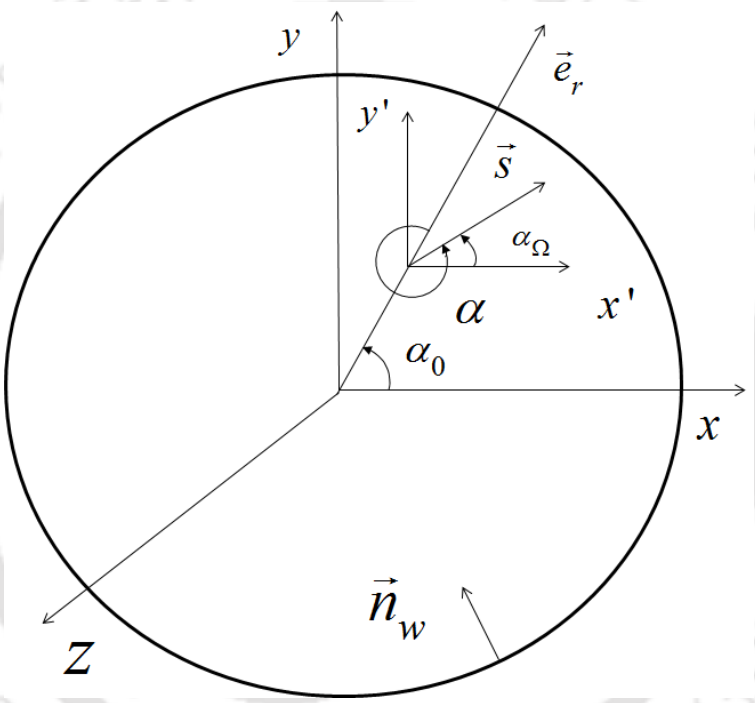

Figure 2.3. Schematic of coordinate system

The cylindrical version of the RTE for an absorbing, emitting, and scattering medium can be presented as,

$$\frac{1}{r}\frac{\partial}{\partial r}[\mu \mathrm{rI}(\vec{\mathrm{r}},\vec{\mathrm{s}})]+\frac{1}{r}\frac{\partial}{\partial \varphi_0}[\eta \mathrm{I}(\vec{\mathrm{r}},\vec{\mathrm{s}})]+\frac{\partial}{\partial z}[\xi \mathrm{I}(\vec{\mathrm{r}},\vec{\mathrm{s}})]-\frac{1}{r}\frac{\partial}{\partial \alpha}[\eta \mathrm{I}(\vec{\mathrm{r}},\vec{\mathrm{s}})]$$
$$=-\beta(\vec{\mathrm{r}})\mathrm{I}(\vec{\mathrm{r}},\vec{\mathrm{s}})+\kappa_a(\vec{\mathrm{r}})\mathrm{I}_b(\vec{\mathrm{r}})+\frac{\sigma_s(\vec{\mathrm{r}})}{4\pi}\int_{\Omega'=4\pi}\mathrm{I}(\vec{\mathrm{r}},\vec{\mathrm{s}}')\,d\Omega' \qquad 2.34$$

Here, $\mu = \sin\theta\cos\alpha, \eta = \sin\theta\sin\alpha$, and $\xi = \cos\theta$ are the direction cosines of a path $\vec{s}$, and $\beta(\vec{r}) = \kappa_a(\vec{r}) + \sigma_s(\vec{r})$ is the extinction coefficient of the participating medium.

$\kappa_a(\vec{r})$ and $\sigma_s(\vec{r})$ are the absorption and scattering coefficients respectively. For an axisymmetric geometry, the $\partial/\partial\alpha_0$ term of the above equation is eliminated, thereby removing one spatial coordinate from the system. For a diffusely emitting and reflecting wall the above RTE is subject to the following boundary condition:

$$I_W(\mathrm{r}_W,\vec{s}) = \varepsilon_w I_b(\mathrm{r}_W) + \frac{1-\varepsilon_w}{\pi} \int_{\vec{n}_W \bullet \vec{s}' < 0} I(\mathrm{r}_W,\vec{s}')\,|\vec{\eta}\bullet\vec{s}'|\,\mathrm{d}\Omega' \text{ for } \vec{\eta}\bullet\vec{s} > 0 \qquad 2.35$$

Subscripts b and w denote the black body and bounded wall respectively. r_W is the radial distance to the bounded wall and $\vec{n}_W$ is the unit normal vector towards medium at the bounding cylindrical wall as shown in Fig. 2.5.

The 2-D axisymmetric mesh on the r - z plane, employed for the present analysis, is shown in Fig. 2.4a. To formulate the discretization equation describing the axisymmetric behavior, however, three-dimensional control volume shown in Fig. 2.4b is considered firstly, and then the axisymmetric solution method is discussed. Here the intensity is independent of spatial azimuthal angle α_0 and is therefore completely specified by $r, z, \theta, \text{and}\,\alpha$. Thereby, the intensity $I(\vec{r},\vec{s})$. can be expressed as $I(r,z,\theta,\alpha)$. All the intensities denoted by $I_2^1, I_3^1, I_4^1, \text{and} I_5^1$ shown in Fig. 2.4b correspond to the same radius of *r*. The spatial azimuthal angle between consecutive points being $\pi/4$, successive nodal points, 2, 3, 4, and 5 are located at $\alpha_0 = 7\pi/8, 5\pi/8, 3\pi/8, \text{and}\,\pi/8,$ respectively, where α_0 is measured from the positive *x*-axis. The angular azimuthal angle measured from the Cartesian *x*-axis is $\alpha_0 = 0$ for all intensities. Therefore, the angle of $\alpha = \alpha_\Omega - \alpha_0$ is $9\pi/8, 11\pi/8, 13\pi/8, \text{and} 15\pi/8$ for the intensities $I_2^1, I_3^1, I_4^1, \text{and}\, I_5^1,$ respectively. The intensities at point 1 in Fig. 2.4a all have the same radius of r, but are now all located at $\alpha_0 = \pi/2$ with the angular azimuthal angle of $\alpha = 15\pi/8, 13\pi/8, 11\pi/8, \text{and}\, 9\pi/8$ for intensities $I_1^5, I_1^4, I_1^3, \text{and}\, I_1^2,$ respectively. Thereby it follows that I_m^1 and I_1^m have the same value of $r, z, \theta,$ and α where m = 2, 3, 4, and 5, leading to $I_m^1 = I_1^m$. A simple mapping therefore exists between the intensities in Fig. 2.4a and 2.4b.

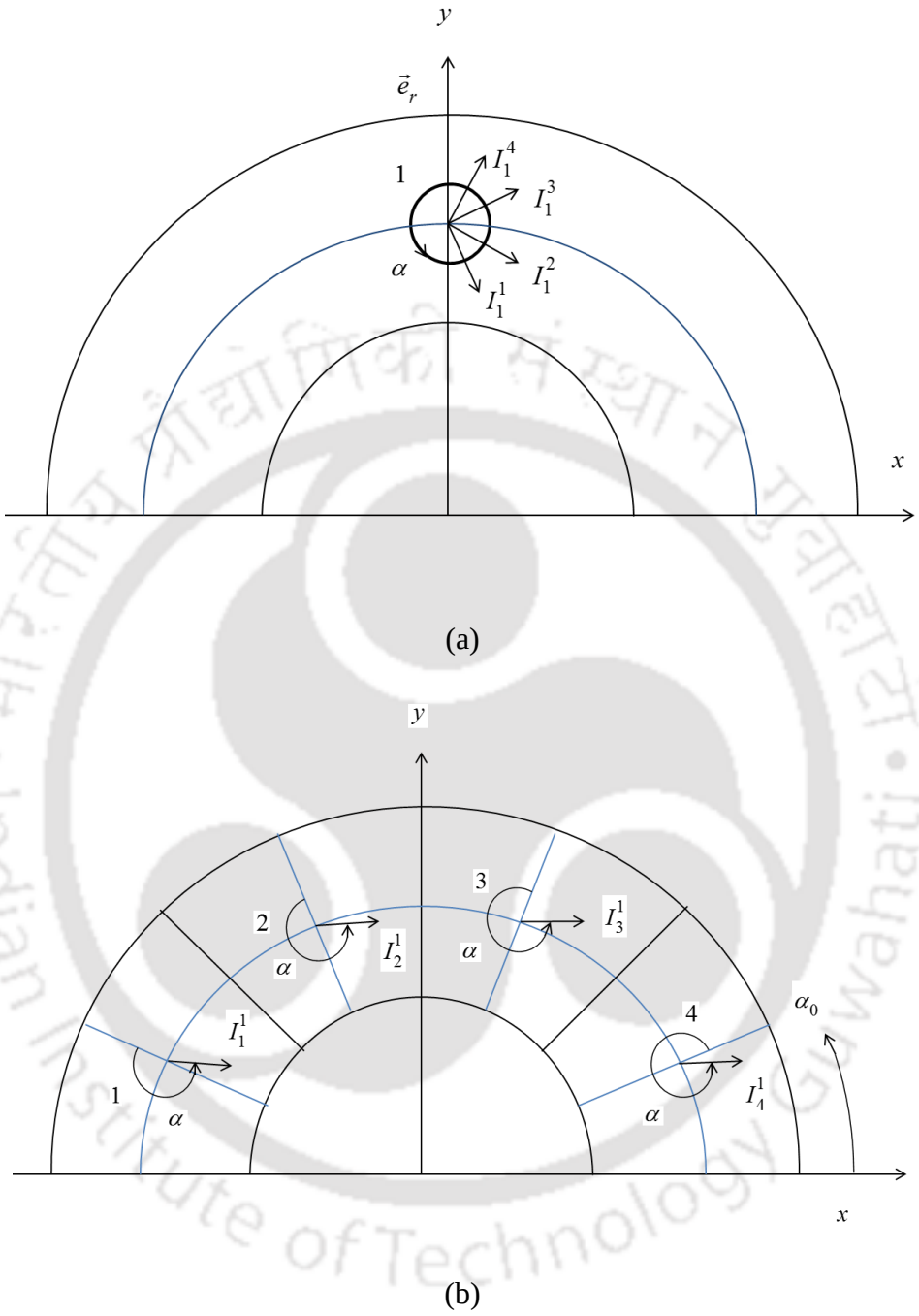

Figure 2.4. (a) Two dimensional distribution of intensities (b) Three dimensional distribution of intensities. Mapping shows that I_j^k of (a) is equals to I_k^j of (b).

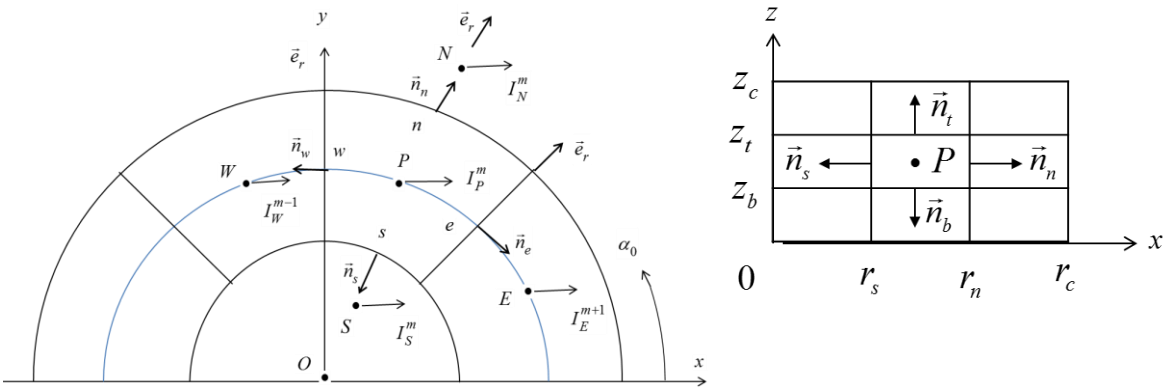

(a) (b)

Figure 2.5: Schematic of a control volume in a cylindrical enclosure with P located at the control volume center (a) top view and (b) side view

The control volume shown in Fig. 2.5 shows the radiative intensities at each nodal point, P, E, W, N, S, T, and B with the unit normal vectors $\vec{n}_i$ at face *i*. The control volume represented by the nodal point, P, is enclosed by six control faces denoted by e, w, n, s, t, and b. By using the cylindrical base vectors, $\vec{s} = \vec{e}_r \sin\theta\cos\alpha + \vec{e}_{\alpha 0} \sin\theta\sin\alpha + \vec{e}_z \cos\theta$, the unit normal vector at each face is expressed as $\vec{n}_i = \vec{e}_r n_{r,i} + \vec{e}_{\alpha_0} n_{\alpha_0,i} + \vec{e}_z n_{z,i}$, so that $\vec{n}_n = -\vec{n}_n = \vec{e}_r, \vec{n}_t = -\vec{n}_b = \vec{e}_z$ and $\vec{n}_e = -\vec{n}_w = -\vec{e}_{\alpha_0}$. Fig. 2.6a shows the polar m^{th} and azimuthal n^{th} control angle ranging from $\theta^{m-1/2}$ to $\theta^{m+1/2}$ and from $\alpha^{n-1/2}$ to $\alpha^{n+1/2}$ respectively, which is typically used in the finite volume radiation methods. The angular azimuthal angle measured from the *r*-axis can vary from 0 to 2π. Here, it is noted that the angular azimuthal angle α varies for a different r-axis as the spatial polar angle, α_0, varies as shown in Fig. 2.4b. Thereby, the intensities at point E and W are represented by I_E^{m+1} and I_W^{m-1}, respectively. Similarly, the intensities at face e and w are expressed by $I_e^{m+1/2}$ and $I_w^{m-1/2}$, respectively. Here, it is explained that the increment of spatial and angular azimuthal angle is chosen to be equal to each other, i.e., $\Delta\alpha_0 = \Delta\alpha$. Fig. 4b illustrates the control angle located at an arbitrary point, for example, face w with total number of control angle of $N_\alpha = N_{\alpha_0} = 4$. The

$\alpha = n+1/2$th control angle, which is enlarged in Fig. 2.6b, is an edge control angle ranging from α^n to α^{n+1}.

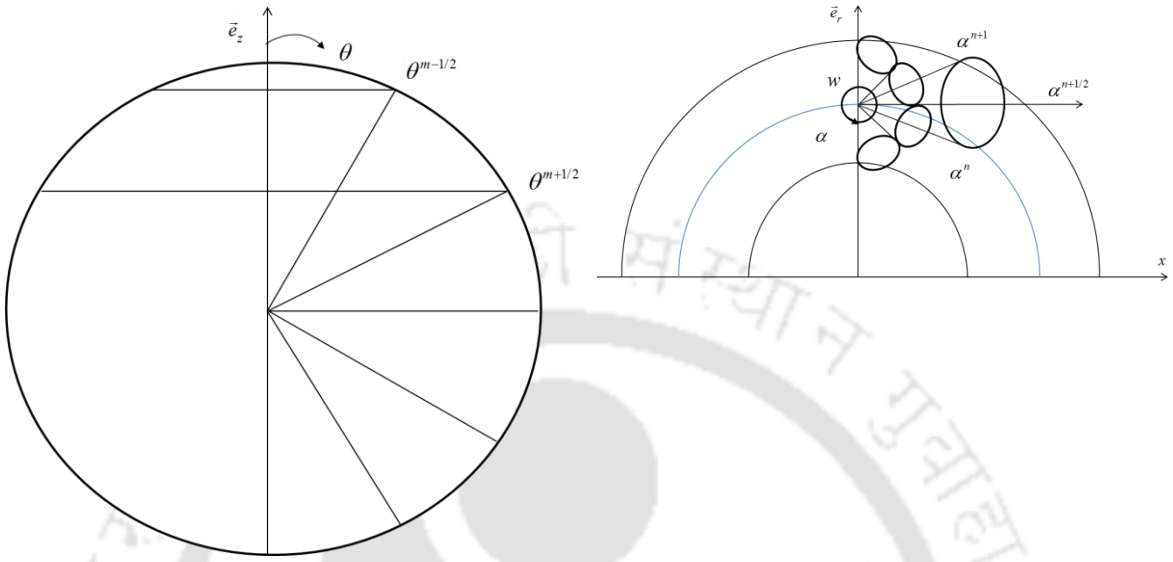

(a) (b)

Figure 2.6: Schematics of the control angle. The angular polar angle θ in (a) is measured from *z*-axis, while azimuthal angle α in (b) is measured from *r*-axis. The polar angle θ^m is between $\theta^{m-1/2}$ and $\theta^{m+1/2}$. Note that while the azimuthal angle α^n ranges from $\alpha^{n-1/2}$ to $\alpha^{n+1/2}$, the range of angular edge control angle $\alpha^{n+1/2}$ is between α^n and α^{n+1}.

Attention is now turned to the directional weight at face $i = n,s,t,$and b through (m,n)th control angle, D_i^{mn}, to give further explanation for the current solution method. This directional weight, D_i^{mn}, denotes the inflow or outflow of radiant energy across the control volume face depending on its sign as defined in the form:

$$D_i^{mn} = \int_{\alpha^{n-1/2}}^{\alpha^{n+1/2}} \int_{\theta^{m-}}^{\theta^{m+}} (\vec{s}.\vec{n}_i)\sin\theta\, d\theta\, d\alpha \qquad (2.36)$$

where the unit direction vector, $\vec{s}$, and outward unit normal vector, $\vec{n}$, at face i are based on cylindrical coordinates as explained above. Hereafter, D_i^{mn} in each control volume face is discretized as:

$$D_n^{mn} = -D_s^{mn} = \int_{\theta^{m-1/2}}^{\theta^{m+1/2}} \sin^2\theta\, d\theta \int_{\alpha^{n-1/2}}^{\alpha^{n+1/2}} \cos\alpha\, d\alpha$$
$$= [\frac{1}{2}(\theta^{m+1/2} - \theta^{m-1/2}) - \frac{1}{4}(\sin 2\theta^{m+1/2} - \sin 2\theta^{m-1/2})](\sin\alpha^{n+1/2} - \sin\alpha^{n-1/2}) \quad (2.37)$$

$$D_t^{mn} = -D_b^{mn} = \int_{\theta^{m-1/2}}^{\theta^{m+1/2}} \sin\theta\cos\theta\, d\theta \int_{\alpha^{n-1/2}}^{\alpha^{n+1/2}} d\alpha = \frac{1}{2}(\sin^2\theta^{m+1/2} - \sin^2\theta^{m-1/2})(\alpha^{n+1/2} - \alpha^{n-1/2}) \quad (2.38)$$

Based on this spatial and angular considerations, angular derivative term can be modeled by using the directional weights, which can be obtained through the integration process over a control volume ΔV and a control angle $\Delta\Omega^{mn}$ such that:

$$-\int_{\Delta\Omega}\int_{\Delta V} \frac{1}{r}\frac{\partial}{\partial\alpha}(\eta I)\, dV d\Omega \simeq \Delta A_e D_e^{mn+1/2} I_e^{mn+1/2} + \Delta A_w D_w^{mn-1/2} I_w^{mn-1/2} \quad (2.39)$$

where

$$D_e^{mn+1/2} = -\int_{\theta^{m-1/2}}^{\theta^{m+1/2}} \sin^2\theta\, d\theta \int_{\alpha^n}^{\alpha^{n+1}} \sin\alpha\, d\alpha$$
$$= -[\frac{1}{2}(\theta^{m+1/2} - \theta^{m-1/2}) - \frac{1}{4}(\sin 2\theta^{m+1/2} - \sin 2\theta^{m-1/2})] \times (\cos\alpha^n - \cos\alpha^{n+1}) \quad (2.40)$$

$$D_w^{mn-1/2} = \int_{\theta^{m-1/2}}^{\theta^{m+1/2}} \sin^2\theta\, d\theta \int_{\alpha^{n-1}}^{\alpha^n} \sin\alpha\, d\alpha$$
$$= [\frac{1}{2}(\theta^{m+1/2} - \theta^{m-1/2}) - \frac{1}{4}(\sin 2\theta^{m+1/2} - \sin 2\theta^{m-1/2})] \times (\cos\alpha^{n-1} - \cos\alpha^n) \quad (2.41)$$

are the angular edge directional weights at east and west faces and $\Delta A_e = \Delta A_w = (r_n - r_s)\Delta z$ is the surface area of east and west faces, respectively. Here, it is necessary to emphasize that the angular direction $\alpha^{n+1/2}$ ranges from α^n to α^{n+1} as shown in Fig. 4b. It is found that this $\alpha^{n+1/2}$ direction is the angular edge where the two control angles meet between $\alpha^{n-1/2} < \alpha^n < \alpha^{n+1/2}$ and $\alpha^{(n+1)-1/2} < \alpha^{n+1} < \alpha^{(n+1)+1/2}$. Therefore, $\Delta A_w D_w^{mn-1/2} I_w^{mn-1/2}$ and $\Delta A_e D_e^{mn+1/2} I_e^{mn+1/2}$ represent the inflow and outflow of the radiant energy through these control faces, i.e., edge control angles, since $D_w^{mn-1/2} < 0$ and $D_e^{mn+1/2} > 0$ are always satisfied regardless of the spatial α_0 locations. Fig. 2.6 illustrates the angular edge directional weights, $D_e^{mn+1/2}$ and $D_w^{mn-1/2}$ with $D_n^{mn} = -D_s^{mn}$. Here, it can be found that $D_e^{mn+1/2} = -D_w^{mn-1/2}$ is satisfied from the geometrical point of view as shown in Fig. 2.6. Also, it is noted that $D_w^{mn-1/2} = D_e^{mN_\alpha+1/2} = 0$ is always satisfied because the azimuthal angular range of $D_w^{mn-1/2}$ and $D_e^{mN_\alpha+1/2}$ are perpendicular to the outward unit normal vector at each face,

i.e., $\vec{n}_w$ and $\vec{n}_e$. Thereby, the face intensities $I_w^{m1-1/2}$ and $I_e^{mN_\alpha+1/2}$ are not necessary to specify for the present computation.

To obtain the finite volume discretized form of the RTE, Eq. (2.34) is integrated over a control volume, ΔV, and a control angle, $\Delta\Omega^{mn}$, assuming that the magnitude of intensity is constant within ΔV, and $\Delta\Omega^{mn}$, but allowing its direction to vary by following the conventional practice of the FVM , and then Eq. (2.39) is substituted into the integrated form of Eq. (2.34). Thereby, the following equation can be obtained:

$$\sum_{i=n,s,t,b} I_i^{mn}\Delta A_i D_i^{mn} + [\Delta A_e D_e^{mn+1/2} I_e^{mn+1/2} + \Delta A_w D_w^{mn+1/2} I_w^{mn-1/2}] + \beta I_P^{mn}\Delta V\,\Delta\Omega^{mn} = S_P^{mn}\Delta V\,\Delta\Omega^{mn} \tag{2.42}$$

where $\Delta A_n = \mathrm{r}_n\,\Delta\alpha\,\Delta z, \Delta A_s = \mathrm{r}_s\,\Delta\alpha\,\Delta z,$ and $\Delta A_t = \Delta A_b = \pi(\mathrm{r}_n^2 - \mathrm{r}_s^2)/2N_\alpha$ are the surface areas of north, south, top, and bottom faces, respectively. $\Delta V = \pi(\mathrm{r}_n^2 - \mathrm{r}_s^2)\Delta z / 2N_\alpha$ is the volume of the control volume P and $\Delta\Omega^{mn} = (\cos\theta^{m-1/2} - \cos\theta^{m+1/2})(\alpha^{n+1/2} - \alpha^{n-1/2})$ is the discrete solid angle.

To relate the facial intensity, I_i^{mn}, and the angular edge intensity, $I_i^{mn\pm1/2}$, to the nodal intensity, I_i^{mn} the following simple step scheme popularly used in the DOM and FVM is introduced to ensure positive intensity:

$$\begin{aligned} I_i^{mn} D_i^m &= I_P^{mn}\max(D_i^{mn},0) - I_I^{mn}\max(-D_i^{mn},0) \\ I_e^{mn+1/2} &= I_P^{mn} \\ I_w^{mn-1/2} &= I_W^{mn-1} = I_P^{mn-1} \end{aligned} \tag{2.43}$$

In Eq. (2.43), subscript i represents n,s,t and b, while I does the corresponding N, S, T and B. By using this scheme, Eq. (2.42) can be recast into the following general discretization equation:

$$a_P^{mn} I_P^{mn} = \sum_{I=N,S,T,B} a_I^{mn} I_I^{mn} + b_P^{mn} \tag{2.43}$$

where

$$a_P^{mn} = \sum_{i=n,s,t,b} \max(\Delta A_i D_i^{mn},0) + \beta\Delta V\,\Delta\Omega^{mn} + \Delta A_e D_e^{mn+1/2} \tag{2.44a}$$

$$a_I^m = \max(-\Delta A_i D_i^{mn},0) \tag{2.44b}$$

$$b_P^{mn} = S_P^{mn}\Delta V\Delta\Omega^{mn} - \Delta A_w D_w^{mn-1/2} I_P^{mn-1} \tag{2.44c}$$

$$S_P^{mn} = \kappa_a I_b + \int_{\Omega'=4\pi} I(\vec{r},\vec{s}')\, d\Omega' \tag{2.44d}$$

In these formulations the last terms in Eqs. (2.44b) and (2.44d) indicate the angular flux of radiant energy, which results from the modeling of angular redistribution term in Eq. (2.39) to Eq. (2.41).

The boundary condition in Eq. (2.35) for a diffusely reflecting and emitting wall can be arranged to

$$I_w^{mn} = \varepsilon_w I_{b,w} + \frac{1-\varepsilon_w}{\pi} \sum_{m'n', D_w^{m'n'}<0} I_w^{m'n'} |D_w^{m'n'}| \quad \text{for } D_w^{mn} > 0 \tag{2.45}$$

where

$$D_w^{mn} = \int_{\Delta\Omega^{mn}} (\vec{s}\bullet\vec{n}_w)\, d\Omega \tag{2.46}$$

is the directional weight at wall and it becomes $-D_n^{mn}, -D_b^{mn}$, and $-D_t^{mn}$ at side ($r = r_c$), bottom ($z = 0$), and top ($z = z_c$) walls of the cylindrical enclosure, respectively.

2.6 Solution Methodology

The procedure adopted for solving the direct problem can sequentially be described as follows (Fig. 2.7) :

1. Divide the computational domain into finite number of control volumes.
2. Start with a guessed temperature field.
3. Solve the RTE by using the DTM of the FVM to compute $\nabla.q_R$.
4. Solve the energy equation for updated temperature fields using Gauss-Siedel method.
5. Check the convergence criterion and if so, terminate the process.
6. If not converged, go to step 3.

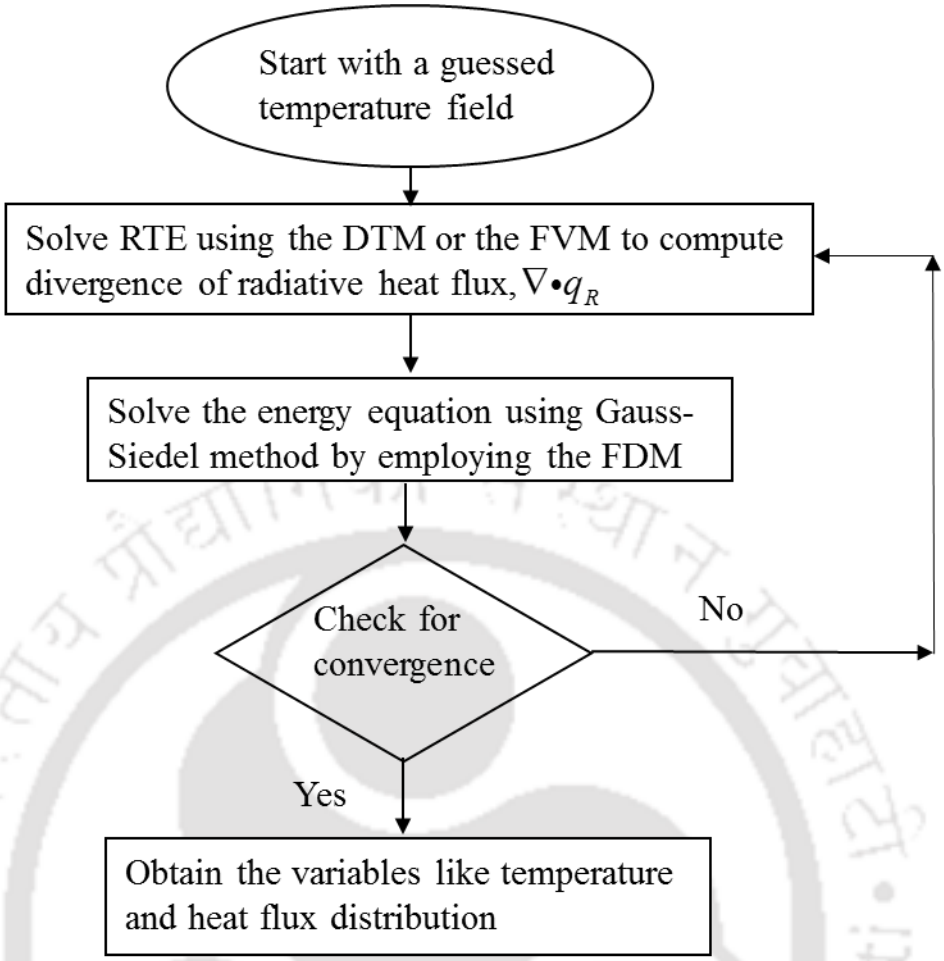

Figure 2.7: Flowchart of the solution procedure for direct problem.

The temperature distribution can be obtained in the direct method using the knowledge of the exact values of medium properties, along with the specified initial, as well as, boundary conditions. The inverse method simultaneously estimates multiple unknown parameters for a known temperature distribution. Present study assumes that the temperature distribution provided by the direct method is accurate and hence can be employed as the exact value. Therefore its difference with an initially guessed and sequentially updated temperature distribution needs to be minimized in the inverse method following a suitably chosen optimization algorithm. Following section discusses the relevant algorithms.

2.7 Brief Discussion of Optimization

Inverse heat transfer problems are ill-posed and hence requires special methods. Various methods like iterative regularization [85], conjugate gradient iterative algorithm [86, 87], function specification method [88, 89], combined regularization and function estimation method [90, 91] and filtering techniques [92 – 94] have been used to obtain stable solution. These conventional methods are very efficient computationally and applied to almost all types of problems [95]. Many books dealing with such methods are available [87, 96, 97].

Although these conventional methods are efficient, it was found that some of these conventional methods are not able to converge to the global optimum. Apart from this, conventional methods requires information regarding the gradients (which are sometimes hard to determine or involves more computational time) and are problem specific. Situations can become complex when problem involves non-linearity and large number of parameters [96]. It is very hard (if not impossible) to apply such methods in problems involving shape optimization of heat exchangers [98], discrete optimal locations of the heat sources [99, 100] and size and location of tumors [101, 102]. Stochastic search based methods (Genetic algorithm, ant colony optimization, particle swarm optimization, simulated annealing, etc.) with a suitable ‘‘governing mechanism’’ leading to the optimal solution are good alternatives. These methods usually does not suffer with the problem of local convergence. Moreover, these methods are blind (not problem specific) and gradient information is not required. Hence, these methods are more robust. Computational time is of course a concern for these methods [100] but with ever growing computational power, parallelization [103], modifications [104 – 106] and development of hybrid methods [107 – 109], these methods can substitute the conventional methods. Growing interest in metaheuristic algorithms in the field of heat transfer (including inverse heat transfer) is already evident from almost ten percent increase in the articles published using such methods in the last decade [110]. Various algorithms were developed in the past like multiple starting point algorithm (MSPA), pattern search algorithm (PSA), genetic algorithm (GA), simulated annealing algorithm (SAA), global search algorithm (GSA) etc.

2.7.1 Algorithms

2.7.1.1 Genetic Algorithm (GA)

The genetic algorithm is probably the most popular stochastic optimization method. It is also widely used in many heat transfer applications, including inverse heat transfer analysis. The GA starts its search from a randomly generated population. This population evolves over successive generations (iterations) by applying three major operations. The first operation is selection, which mimics the principle of "survival of the fittest" in nature. It finds the members of the population with the best performance, and assigns them to generate the new members for future generations. This is basically a sort procedure based on the obtained values of the objective function. The number of elite members that are chosen to be the parents of the next generation is also an important parameter. Usually, a small fraction of the less fit solutions are also included in the selection, to increase the global capability of the search and prevent premature convergence. The second operator is called reproduction or crossover, which imitates mating and reproduction in biological populations. It propagates the good features of the parent generation into the offspring population. In numerical applications, this can be done in several ways. One way is to have each part of the array coming from one parent. This is normally used in binary-encoded algorithms. Another method that is more popular in real encoded algorithms is to use a weighted average of the parents to produce the children. The latter approach in used in this research. The last operator is mutation, which allows for global search of the best features, by applying random changes in random members of the generation. This operation is crucial in avoiding the local minima traps. More details about the algorithm may be found in [111, 112].

2.7.1.2 Global Search Algorithm (GSA)

The main idea behind Global Search Algorithm (GSA) [113, 114] is to find starting points for gradient based local NLP solvers. The GSA uses OptQuest, which is a scatter search, and is used to find the starting point for such gradient search algorithm. The combination of global optimization along with powerful local search makes this algorithm very effective. In this reference it has been proved that this algorithm is capable

of solving complex optimization problem with linear and non linear constraints easily. The Scatter Search is an augmentation of GA where new population is generated in a deterministic way rather than the random way. The most general problem this algorithm can solve has the form:

$$\text{minimize } f(x, y) \tag{2.47}$$

Subjected to the nonlinear constraints:

$$\text{gl} \le G(x, y) \le \text{gu} \tag{2.48}$$

The linear constraints:

$$\text{l} \le Ax + Ay \le \text{u1 2} \tag{2.49}$$

$$x \in S, y \in Y \tag{2.50}$$

Where:

$x =$ An n-dimensional vector of continuous decision variables

$y =$ A p-dimensional vector of discrete decision variables and the vectors gl, gu, l and u contain upper and lower bounds for the nonlinear and linear constraints, respectively

The matrices 1A and 2A are 2m by n and 2m by p respectively and contain the coefficients of any linear constraints. The set S is defined by simple bounds on x and assume that it is closed and bounded, i.e., that each component of x has a finite upper and lower bound. This is required by the OptQuest scatter search procedure.

The set Y is assumed to be finite and is often the set of all p-dimensional binary or integer vectors y which satisfy finite bounds. The objective function f and the 1 m –dimensional vector of constraint functions G are assumed to have continuous first partial derivatives at all points in This is necessary so that a gradient-based local NLP solver can be applied to the relaxed NLP sub-problems formed from (Eq.(2.47) –Eq. (2.50)) by allowing the y variables to be continuous.

2.7.1.3 Pattern Search Algorithm (PSA)

Pattern search algorithm is a heuristic that can provide useful approximate solutions for some problems, but can fail on others. Pattern search algorithm is not an iterative method

that converges to a solution; indeed, pattern search methods can converge to non-stationary points on some relatively tame problems.

The name, pattern search, was coined by Hooke and Jeeves [115]. An early and simple PS variant is attributed to Fermi and Metropolis when they worked at the Los Alamos National Laboratory as described by Davidon [116] who summarized the algorithm as follows:

"They varied one theoretical parameter at a time by steps of the same magnitude, and when no such increase or decrease in any one parameter further improved the fit to the experimental data, they halved the step size and repeated the process until the steps were deemed sufficiently small."

2.7.1.4 Simulated Annealing Algorithm (SAA)

Simulated annealing (SA) [117 – 119] is a method for solving unconstrained and bound-constrained optimization problems. The method models the physical process of heating a material and then slowly lowering the temperature to decrease defects, thus minimizing the system energy.

At each iteration of the simulated annealing algorithm, a new point is randomly generated. The distance of the new point from the current point, or the extent of the search, is based on a probability distribution with a scale proportional to the temperature. The algorithm accepts all new points that lower the objective, but also, with a certain probability, points that raise the objective. By accepting points that raise the objective, the algorithm avoids being trapped in local minima in early iterations and is able to explore globally for better solutions.

2.7.1.5 Multiple Starting Point Algorithm (MSPA)

When the functions are smooth a very practical means of addressing the global optimization problem is to use a local optimization routine but start it from many different points. If the best of the resulting solutions is retained, then we might be willing to accept this as a global solution. Of course there is no guarantee that a global minimum has been

found, but increased confidence might be gained by using more starting points or by running the program again with different starting points. Frequently this technique will prove to be faster and as reliable as other methods. We offer a multi-start routine, e05ucc, in the NAG C Library (at Mark 23). This routine uses a sequential QP algorithm for finding the local minimum of a general nonlinear function subject to linear, nonlinear and simple bound constraints. The user has the option to retain not just the best solution, but any specified number of solutions, ordered to reflect the value of the objective at the minimum. Such a facility might be useful when there are other criteria, not specified in the mathematical solution, that the user would like in an acceptable solution. An example might be a solution that is 'good', but stable in the sense that small changes in the variables do not cause a large change in the objective. So, for example, small errors in manufacturing a part might not diminish performance of the assembled product. More details about this algorithm can be found in [120, 121].

2.8 Formulation of Inverse Problem

In the combined-mode conduction-radiation heat transfer problem, the temperature distributions can be obtained from the direct method, as mentioned earlier. For the correct value of the unknown parameters, with given initial and boundary conditions, let $\tilde{\theta}_p$, $p=1,2,.....N$ be the known temperature at the west boundary of the p^{th} control volume. For the same initial and boundary conditions, in the inverse problem, the objective is to estimate the correct values of the unknown parameters for the known temperature $\tilde{\theta}_p$ field. Initially a guessed value of unknown parameters is taken and then the guessed temperature field is calculated. Since θ_p is based on guess values of unknown parameters, the exact value $\tilde{\theta}_p$ and the estimated value θ_p are not expected to coincide. In order to minimize the difference between $\tilde{\theta}_p$ and θ_p, an objective function J can be defined for a 1-D system as,

$$J=\sum_{p=1}^{N}\left(\tilde{\theta}_p-\theta_p\right)^2 \tag{2.51}$$

Similarly for a 2-D geometry the above equation is expanded as;

$$J=\sum_{p}^{N+1}\sum_{q}^{N+1}\left(\tilde{\theta}_{p,q}-\theta_{p,q}\right)^2 \tag{2.52}$$

In the above equation, $\tilde{\theta}_{p,q}$ is the exact temperature and $\theta_{p,q}$ is based on some guessed values of the unknown parameters at any node of the control volume in the FVM.

The accuracy of the estimated parameters depends on how accurately the temperature field is measured. If $\pm E$ is the error in the measurement of temperature profile, then

$$\theta_{\text{measured}} = \tilde{\theta} + E \tag{2.53}$$

where $\tilde{\theta}$ is the exact temperature. With θ_{measured} defined as above, if the measured temperature field contains an error $\pm E$, in Eq. (2.51 and 2.52), $\tilde{\theta} = \theta_{\text{measured}}$. It should be noted that a measurement error of $E = 2.0,$ indicates that if the exact temperature is 500 K, then the measured temperature is 510 K with an error of 10 K. Therefore, the objective function with the inclusion of the measurement error takes the following form:

$$J = \left[\left(\tilde{\theta} \pm E\right) - \theta\right]^2 \tag{2.54}$$

The above equation can be re-arranged as:

$$J = \left[\tilde{\theta} - \left(\theta \mp E\right)\right]^2 \tag{2.55}$$

It is clear from the above expression that, for minimizing the objective function, the optimization algorithm must be robust enough to take care of the increased uncertainties due to the measurement errors. The steps involved in solving the inverse problem are mentioned below.

2.9 Solution Methodology to Solve Inverse Problem

Stepwise procedure for solving an inverse problem is explained below (Fig. 2.8)

1. Obtain any temperature field from the direct method. It is this field corresponding to which unknown parameters need to be obtained.
2. Induce perturbations on the above temperature field. Therefore, this becomes the measured temperature field or experimental data.
3. Start with a guessed temperature field. This will correspond to some arbitrary values of the parameters to be determined.
4. Mininimize/ Regularize/ Optimize the objective function.
5. Define the desired value of the objective function.

6. Check if the objective function value changes in successive iterations.
7. If the objective function value remains nearly constant for sufficient finite number of iterations terminate the algorithm.
8. Get the values of the unknown parameters.
9. If the objective function value keeps changing, discard the old values and assume other values of parameters and go to step 2.

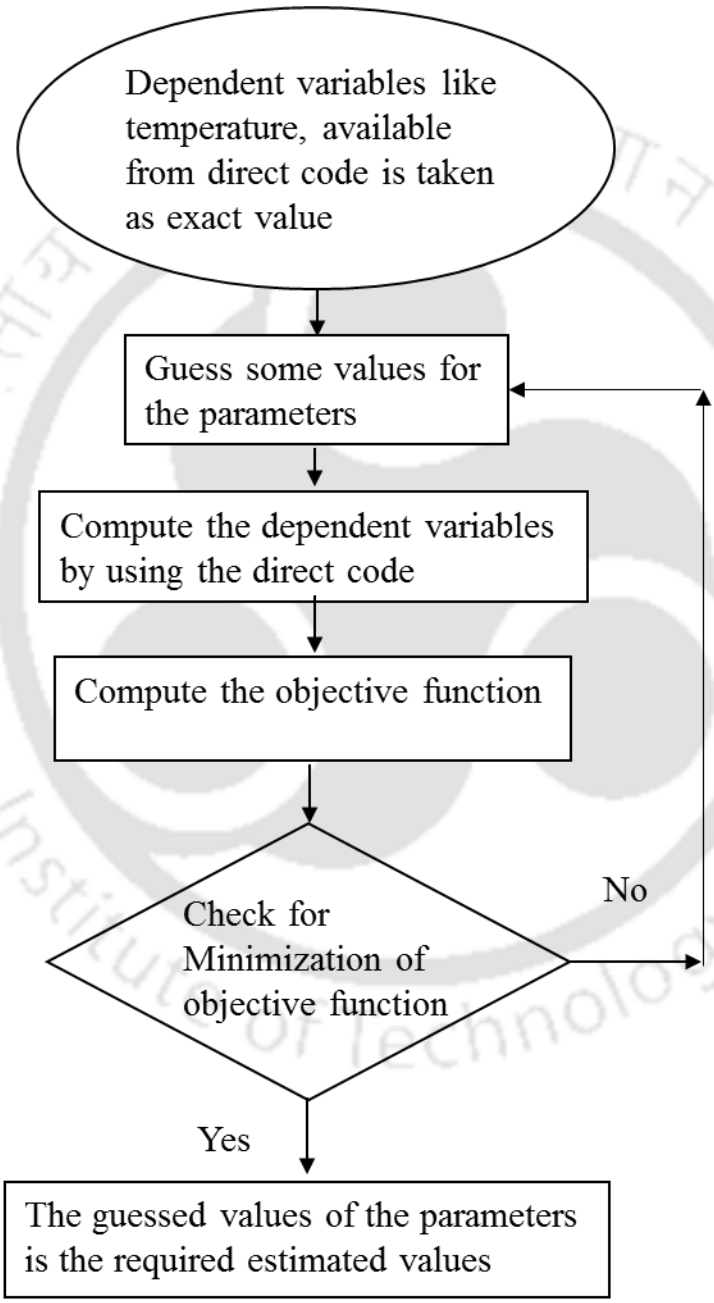

Figure 2.8: Flowchart of the solution procedure of inverse problem.

2.10 Summary

The present chapter dealt with complete mathematical formulation of inverse analysis in conduction-radiation problem. It started with the direct problem involving the FDM and the FVM/DTM methods to solve the energy equation and the equation of obtaining the radiative information, respectively. Then, the formulation of the inverse problem and the construction of the objective function were described. Various optimization algorithms were explained briefly. In the next chapter, we will study the application of the inverse method to a conduction-radiation problem in a 1-D planar porous medium.

Chapter 3

1-D PLANAR POROUS MEDIUM WITH HEAT GENERATION

3.1 Introduction

Numerical analysis plays a vital role in the design and development of any device. This is also true with the development of a porous radiant burner (PRB). For a given power (wattage), design of a PRB working on a specific fuel requires knowledge of thermo-physical and optical properties like thermal conductivity, density, specific heat, extinction coefficient, scattering albedo and emissivities of the porous matrix. Geometric details like the porosities and the dimensions are also required. For the maximum thermal efficiency, and thereof, minimal emissions from the burner, these parameters need to be optimized. Optimization of these parameters is effected using the inverse analysis. In the inverse analysis, based on the knowledge of known distribution of the dependent variable, such as temperature or/and heat fluxes in case of a PRB, unknown parameters, like thermophysical and optical properties or the boundary conditions that yield the temperature field are estimated. Dependent variable obtained from experimental measurement or some other approach is required in framing the objective function. The computed temperature based on the estimated values are fed to the objective function, and the process is repeated until the objective function approaches its set minimum value.

In an effort towards simultaneously estimating the parameters in a PRB, in the present work, estimation of optical parameters is done for a 1-D planar PRB model in which the energy source is taken as a uniform volumetric heat generation zone. Separate energy equations for gas-phase and solid-phase account for non-local thermal equilibrium between the two phases, and they are solved simultaneously [122]. The heat exchange between the gas and the solid is by convection. The porous matrix acts like an optically

participating medium. Thus, the volumetric radiative source term, i.e., the divergence of radiative heat flux $\nabla \cdot q_R$ appears only in the solid-phase energy equation.

With volumetric radiative source term $\nabla \cdot q_R$ known in the solid-phase energy equation, the two energy equations are solved simultaneously. In this Chapter, $\nabla \cdot q_R$ information is computed using the DTM. For estimation of parameters, to minimize the objective function in inverse analysis the GA, and the GSA is employed.

In the following, formulation to solve heat transfer problem in a 1-D planar porous matrix with imbedded heat generation zone is provided. Convective heat transfer from gas to solid is effected by introducing convective heat exchange term in both gas- and solid-phase energy equations. The volumetric radiative source term $\nabla \cdot q_R$ appears only in the solid-phase energy equation. Steady-state temperature distribution, heat fluxes at the exit due to solid conduction and radiation, obtained in the direct method is utilized as known temperature and heat fluxes distribution in the inverse analysis using the GA, and the GSA. Next under results and discussion, for a very strong convective coupling, temperature distribution is validated against the literature. Effects of different parameters on distributions of temperature and different terms of the gas- and solid-phase energy equations are analyzed next. Following that results of simultaneous estimation of two parameters by employing the GA and then three parameters estimation using the GA and the GSA are presented after that. The two optimization algorithms are compared and shown that the GSA performs better than the GA. Conclusions are made at the end.

3.2 Formulation

Consideration is given to an inert porous matrix of thickness *L* (Fig. 3.1). A gas with density ρ_g, specific heat c_g and thermal conductivity k_g passes with uniform

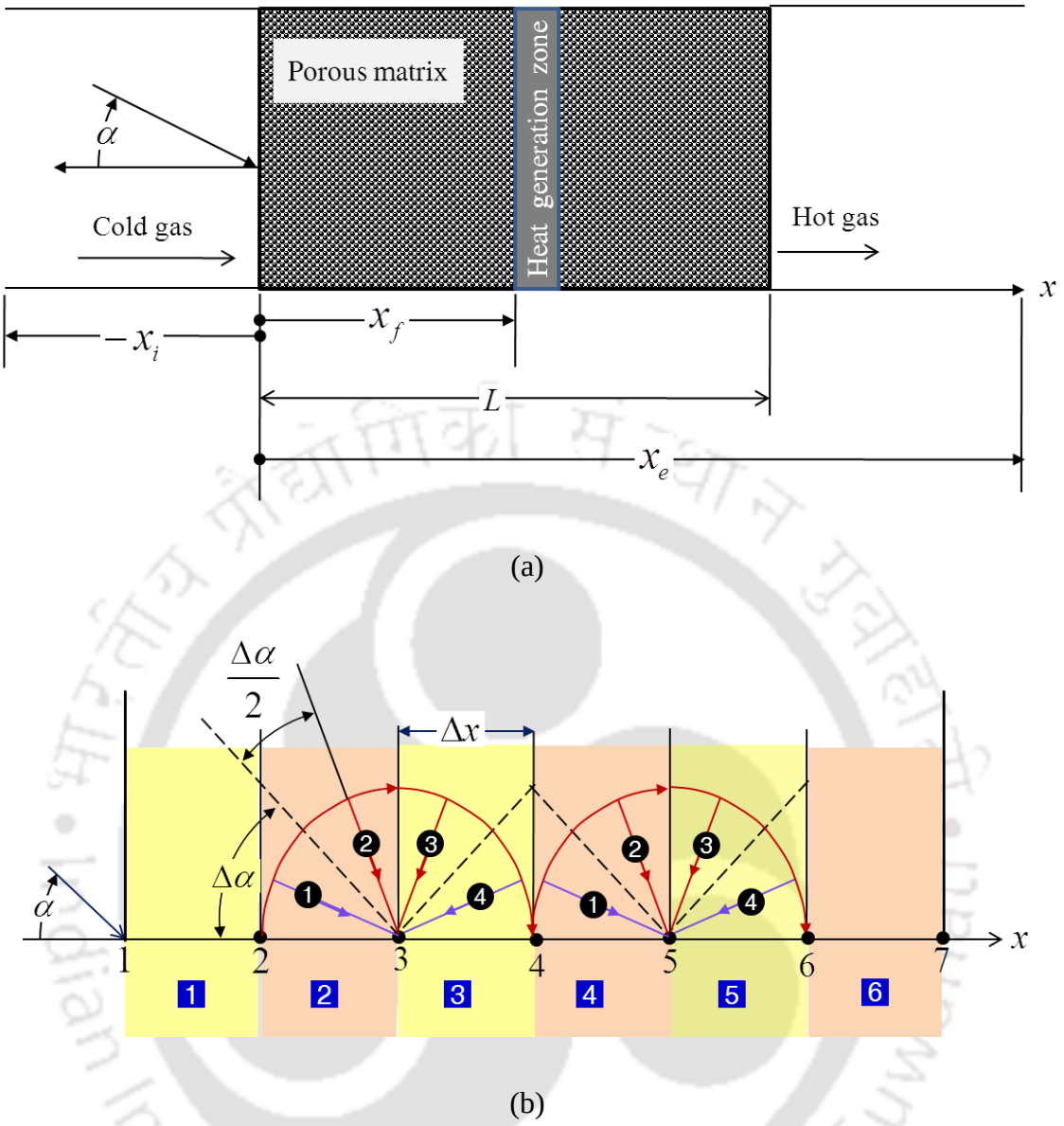

Figure 3.1. (a) Schematic of the porous matrix, computational domain $\left(-x_i \le x \le x_e\right)$ and coordinate system used and (b) ray tracing in the DTM.

velocity u through the porous matrix having density ρ_s, specific heat c_s, thermal conductivity k_s and porosity φ. A centrally located uniform volumetric heat generation zone (Fig. 3.1) in the porous matrix serves as the source of thermal energy. Porous matrix with extinction coefficient β, scattering albedo ω is radiatively participating. It absorbs, emits and scatters radiation. Gas is radiatively transparent, and therefore, does not take part in the volumetric radiative transfer process. The heat transfer between the solid and

the gas is through convection. Since the local value of the solid and the gas temperatures could be different, non-local thermal equilibrium between them is accounted by considering separate energy equations for both the phases. The solid- and gas-phase equations are coupled through a convective heat transfer term. For the problem under consideration, at the steady-state, the energy equations for the gas and solid phases can be written as.

$$\text{Gas phase: } \varphi\rho_g c_g u\frac{dT_g}{dx}+(1-\varphi)Ah\left(T_g-T_s\right)=\varphi\dot{Q}\delta(x)+\varphi k_g\frac{d^2T_g}{dx^2} \tag{3.1}$$

$$\text{Solid phase: } (1-\varphi)Ah\left(T_g-T_s\right)+(1-\varphi)k_s\frac{d^2T_s}{dx^2}=\frac{dq_R}{dx} \tag{3.2}$$

where A is the pore area per unit volume of porous matrix, $\dot{Q}$ is the heat generation rate per unit volume, $\delta(x)$ is the Dirac-delta function defined as unity for $0.45L<x\le 0.55L$ and zero elsewhere. In Eq. (3.2) $\frac{dq_R}{dx}$ represents the volumetric radiative source term, and it is given by

$$\frac{dq_R}{dx}=(1-\omega)\beta\left(4\sigma T^4-G\right) \tag{3.3}$$

where $\sigma=5.67\times10^{-8}\,\mathrm{W\cdot m^{-2}\cdot K^{-4}}$ is the Stefan-Boltzmann constant, and G is the incident radiation.

With volumetric radiative information $\frac{dq_R}{dx}$ computed from the above (Eq. (3.3)), energy equations Eqs. (3.1) and (3.2) can be simultaneously solved. With non-dimensional temperature θ, distance η, radiative heat flux Ψ_R, advection parameter P_1, convective coupling P_2, gas conduction P_3, solid conduction P_4 and Biot number P_5 defined as:

$$\theta=\frac{T-T_i}{T_i}\qquad \eta=\frac{x}{L}\qquad \Psi_R=\frac{q_R}{\dot{Q}L}\qquad P_1=\frac{\rho_g c_g u T_i}{\dot{Q}L}$$
$$P_2=\frac{hAT_i}{\dot{Q}}\qquad P_3=\frac{k_g T_i}{\dot{Q}L^2}\qquad P_4=\frac{k_s T_i}{\dot{Q}L^2}\qquad P_5=\frac{hL}{k} \tag{3.4}$$

the governing equations (3.1) and (3.2) in non-dimensional form are written as

Gas phase: $$\varphi P_1 \frac{d\theta_g}{d\eta} + (1-\varphi) P_2 (\theta_g - \theta_s) = \varphi\delta(\eta) + \varphi P_3 \frac{d^2\theta_g}{d\eta^2} \quad (3.5)$$

Solid phase: $$(1-\varphi)\frac{P_2}{P_3}(\theta_g - \theta_s) + (1-\varphi)\left(\frac{P_4}{P_3}\right)\frac{d^2\theta_s}{d\eta^2} = \frac{1}{P_3}\frac{d\Psi_R}{d\eta} \quad (3.6)$$

For the gas-phase energy equation (Eq. (3.5)), the computational domain is extended to the distance $-x_i$ on the left of the porous matrix and x_e on the right of it (Fig. 3.1a). The same for the solid-phase energy equation (Eq. (3.6)) is $0 \le x \le L$. Far away from the porous matrix, at the inlet $\eta_i \left(= \frac{-x_i}{L}\right)$, the gas is at the ambient temperature $\theta_i = 0.0$, and at the outlet $\eta_e \left(= \frac{x_e}{L}\right)$, the gas temperature gradient $\left.\frac{d\theta_g}{d\eta}\right|_{\eta_e} \to 0.0$ is assumed to prevail. Accordingly, the boundary conditions for the gas-phase energy equation are the followings.

$$\theta_g(\eta_i) = 0.0, \quad \left.\frac{d\theta_g}{d\eta}\right|_{\eta_e} = 0.0 \quad (3.7)$$

For the solid-phase, at locations $\eta = 0$ and $\eta = 1$, heat transfer between the gas and the solid is by convection [122, 69], accordingly the boundary conditions for Eq. (3.6) are the following:

$$\left.\frac{d\theta_s}{d\eta}\right|_{\eta=0} = -P_5(\theta_g - \theta_s), \quad \left.\frac{d\theta_s}{d\eta}\right|_{\eta=1} = P_5(\theta_g - \theta_s) \quad (3.8)$$

Following Eqs. (3.3) and (3.4), in non-dimensional volumetric radiative term $\frac{d\Psi_R}{d\eta}$ appearing in the solid-phase energy equation (Eq. (3.6)) takes the form

$$\frac{d\Psi_R}{d\eta} = \beta L(1-\omega)\left[4\pi\Phi(1+\theta_s)^4 - G^*\right] \quad (3.9)$$

where $\Phi = \frac{\sigma T_i^4}{\dot{Q}L}$ is the non-dimensional emissive power at the inlet η_i and $G^* = \frac{G}{\dot{Q}L}$ is the non-dimensional incident radiation.

With non-dimensional terms defined in Eq. (3.4), the source term in non-dimensional form is written as

$$S^*(\tau) = (1-\omega)\frac{\Phi(1+\theta)^4}{\pi} + \left(\frac{\omega}{4\pi}\right)G^* \tag{3.10}$$

Like any other numerical approach, in the DTM, intensities are always traced from the boundaries, and the boundary intensities are calculated from the radiative boundary condition. For a diffuse-gray boundary with emissivity ε, the radiative boundary condition is the following:

$$\begin{aligned} I_0^* &= \varepsilon\frac{\Phi}{\pi} + \frac{(1-\varepsilon)}{\pi}2\pi\int_{\alpha=0}^{\pi/2} I^*\sin\alpha\cos\alpha\ d\alpha \\ &\approx \varepsilon\frac{\Phi}{\pi} + 2(1-\varepsilon)\sum_{m=1}^{\frac{M}{2}} I^{*,m}\sin\alpha^m\cos\alpha^m\sin(\Delta\alpha) \end{aligned} \tag{3.11}$$

where in Eq. (3.11), $I^* = \dfrac{I}{\dot{Q}L}$ is the non-dimensional intensity. On the downstream side, the burner is assumed to be seeing a black environment at 298 K.

3.3 Results and Discussion

In the present work, in the simultaneous estimation of parameters using the inverse analysis, gas temperature distribution $\theta_g(\eta)$ is the known quantity. Subject to the boundary conditions stated above in Eqs. (3.7), (3.8) and (3.11), $\theta_g(\eta)$ distribution is obtained from the simultaneous solution of Eqs. (3.5) and (3.6). Numerical approach is always susceptible to the number of control volumes / grids, and also to the number of intensities in the $4\pi-$spherical space when the problem involves volumetric radiation. In the present work, for the solid-phase energy equation in the computational domain $0 \le \eta \le 1$, 300 grid points and 20 intensities were found sufficient. In the computational domain $-1 \le \eta \le 2$ of the gas-phase energy equation 900 grid points were used.

3.3.1 Simultaneous estimation of two parameters

In the problem under consideration, the extinction coefficient β, the scattering albedo ω and the emissivity ε are the optical properties of interest, and using the inverse analysis, two of them (β, ε) and (ω, ε) are simultaneously estimated. In the estimation using the inverse analysis, the objective function J is constructed like the following:

$$J = \sum_{i=1}^{N} \left(\tilde{\theta}_{g,i} - \theta_{g,i} \right)^2 \tag{3.12}$$

where $\tilde{\theta}_{g,i}$ and $\theta_{g,i}$ are the exact and unknown gas temperatures, respectively.

In the inverse analysis, the estimated temperature θ_i distribution has been calculated using the FDM-DTM, and the GA has been used to minimize the objective function J.

Before we present results of the simultaneous estimations of parameters, validation of the FDM-DTM formulation is done first. Governing parameters greatly influence the gas and the solid temperatures and the heat flux distributions. These results are presented and analyzed next. Results on estimation of parameters are provided after that.

For extinction coefficient $\beta = 1.0$ and a very strong convective coupling $P_2 = 500.0$, the gas and the solid temperatures distributions obtained using the FDM-DTM approach is compared against the results of Tong and Sathe [122] in Fig. 3.2a. Fig. 3.2b shows this comparison for the distributions of gas and solid conductive heat fluxes $\left(\Psi_{g,\text{cond}}, \Psi_{s,\text{cond}} \right)$, convective heat flux Ψ_{conv} and radiative heat flux Ψ_{rad}. Table 3.1 shows the values of different parameters used for these results. When the convective coupling is strong, θ_g and θ_s are almost the same. From Fig. 3.2, it is observed that the results of the present work match very well with those of Tong and Sathe [122].

Parametric variation has also been carried out to understand the relative influence of the system parameters. The focus is given to P_2 and β, as they are representative of the

convective coupling between both the phases and the extinction coefficient, respectively. Results are presented in Fig. 3.3. For a weak convective coupling $(P_2 = 1.0)$, in Figs. 3.3a

Table 3.1. Parameter values used for simulations.

Parameters	Values
P_1	0.01
P_3	2.5 x 10^{-4}
P_4	0.02
P_5	5
ω	0.5
ε	1.0
$\Phi_i = \Phi_e$	2.98x10^{-5}

and 3.3b, θ_g and θ_s distributions are shown for $\beta = 0.0$ and 1000.0, respectively. For a strong convective coupling $(P_2 = 500.0)$, for $\beta = 0.0$ and 1000.0, θ_g and θ_s distributions are shown in Figs. 3.3c and 3.3d, respectively. An observation of results in Figs. 3.3a and 3.3b shows that upstream to the heat generation zone $(0.45 < \eta \le 0.55)$, the heat transfer is from the solid to the gas, and inside the heat generation zone and downstream beyond that opposite is the trend. Also in the upstream portion, $\beta = 1000.0$ (Fig. 3.3b), the solid and gas temperature are higher than that for $\beta = 0.0$ (Fig. 3.3a), an opposite trend is observed beyond that. The observed trend is attributed to the fact that in the absence of radiation $(\beta = 0.0)$, the heat generation zone does not preheat solid and gas regions upstream to it, and in the downstream region the energy transport is mainly by convection. When the radiation is present $(\beta = 1000.0)$, both upstream and the downstream regions get radiative heating, as a result temperatures θ_g and θ_s are higher in the upstream and lower in the downstream. It is to be noted that when radiation is absent $(\beta = 0.0)$, in the upstream to the heat generation zone, as observed in Fig. 3.3a, the solid and the gas do get heated. The solid gets heated by conduction and the gas by convective heat exchange.

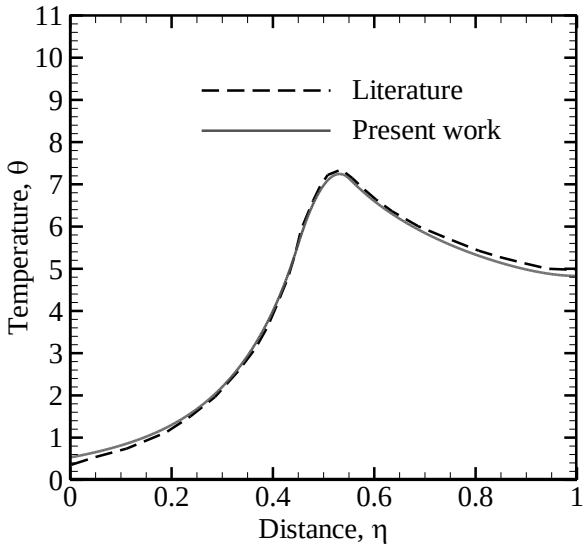

(a)

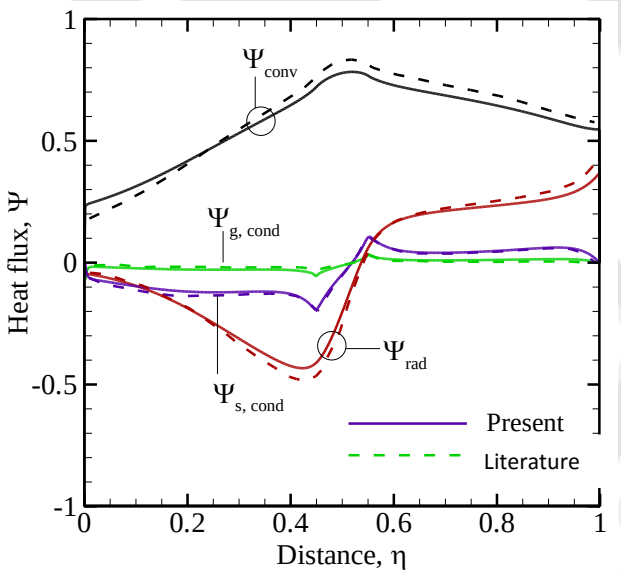

(b)

Figure 3.2. Comparison of (a) temperature distribution θ; $P_2 = 500$ and τ = 1.0 and (b) convective heat flux Ψ_{conv}, radiative heat flux Ψ_{rad}, gas conduction heat flux $\Psi_{g,\,cond}$ and solid conduction heat flux $\Psi_{s,\,cond}$; $P_2 = 500$ and τ = 10 with Ref. [122].

Having analyzed distributions of temperature and various terms of the energy equations, we next provide results of simultaneous estimation of parameters. Two sets of optical

properties of the porous matrix, viz., (β, ε) and (ω, ε) are estimated. First, estimation is done for (β, ε). The exact values for these parameters are: (10, 0.5). Values of other parameters are given in Table 3.1. With four different population sizes, namely, 100, 200, 300 and 400, results are shown in Table 3.2.For every population, results are shown for four different generations, viz., 50, 100, 150 and 200. Reasonably accurate estimation has been obtained. A comparison between the temperature profiles obtained by direct method (FDM-DTM) and inverse method (FDM-DTM-GA) is presented in Fig. 3.5 for a population size of 100 and generation of 200. Excellent degree of conformity can be clearly observed.

When the convective coupling is strong $(P_2 = 500.0)$, irrespective of the value of the extinction coefficient β, θ_g and θ_s distributions are almost the same. However, for the reasons given above, upstream and downstream of the heat generation zone, radiative preheating is achieved for $(\beta = 1000.0)$.

The gas phase energy equation consists of terms owing to convection, conduction, convective heat exchange and heat generation. Whereas, the solid phase energy equation (Eq. (3.6)) has terms owing to conduction, convective heat exchange and volumetric radiation. In the combined mode heat transfer in a porous matrix, contributions of different components in the energy equations for both solid and gas phases provide a useful insight. For strong convective coupling ($P_2 = 500$) and radiation ($\beta = 1000$),for the gas and the solid phase equations, results are shown in Figs. 3.4a and 3.4b, respectively. An observation of Figs. 3.4a and 3.4b shows that the energy input to the gas stream in form of heat generation is primarily balanced by convective heat exchange to the solid (second term on the left-hand-side of Eqn. (3.5) and the first term on the left-hand-side of Eq. (3.6)). Upstream to the heat generation zone, preheating is significant, and accordingly, heat transfer is from solid to the gas. In Fig. 3.4a, the convective heat exchange term has a positive magnitude, whereas as shown in Fig. 3.4b, the same has negative magnitude for the solid phase energy equation.

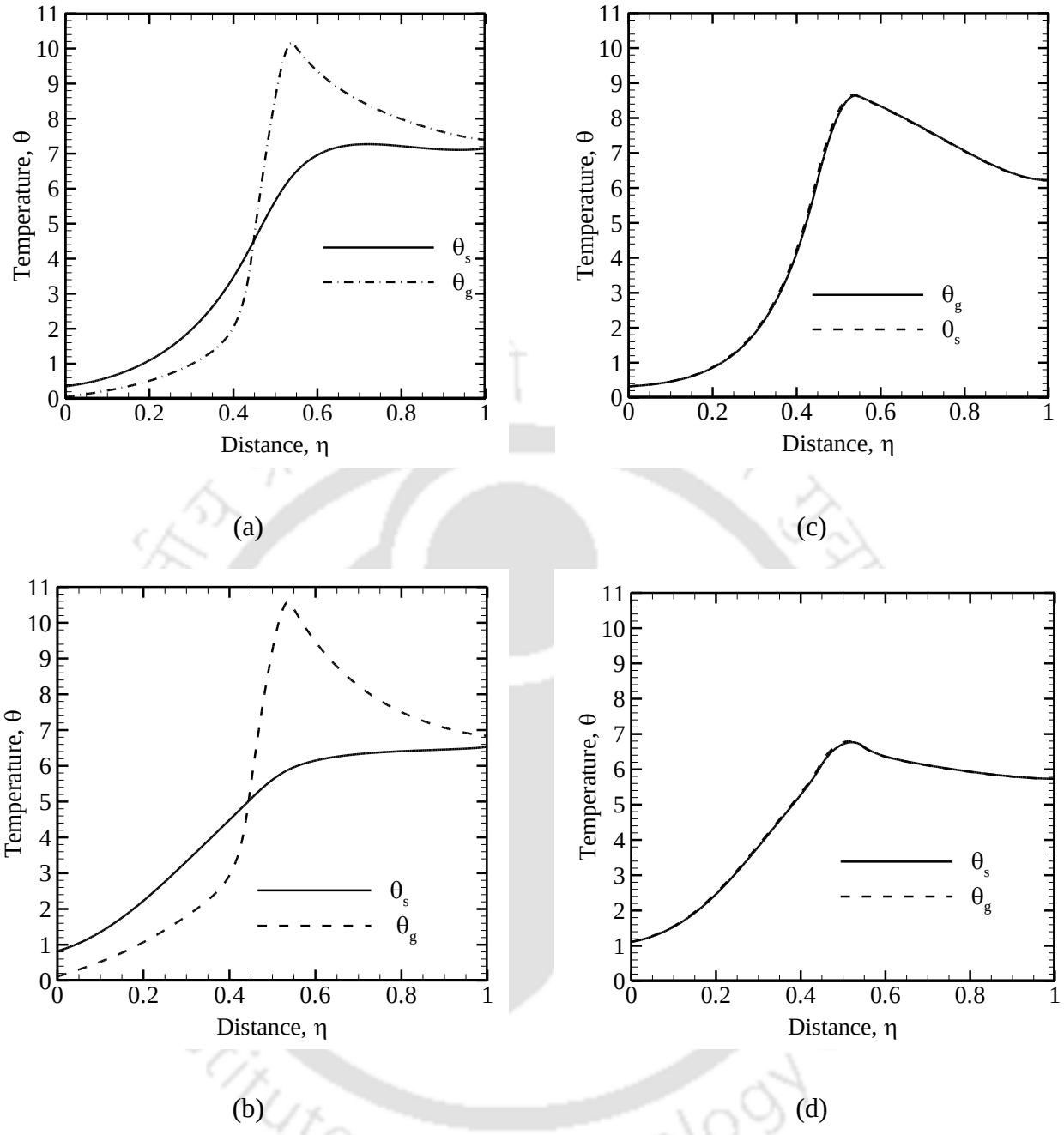

Figure 3.3: Distributions of gas and solid temperatures for (a) $\beta = 0.0, P_2 = 1.0$, (b) $\beta = 1000.0, P_2 = 1.0$, (c) $\beta = 1.0, P_2 = 500.0$ and (d) $\beta = 1000.0, P_2 = 500.0$.

A comparison of Figs. 3.4a and 3.4b shows that beyond the heat generation zone, the gas-phase conduction is insignificant compared to conduction in the solid phase. This is attributed to low gas thermal conductivity combined with low gas temperature gradient. Convection, however, is quite significant, particularly on the upstream-side. As energy is

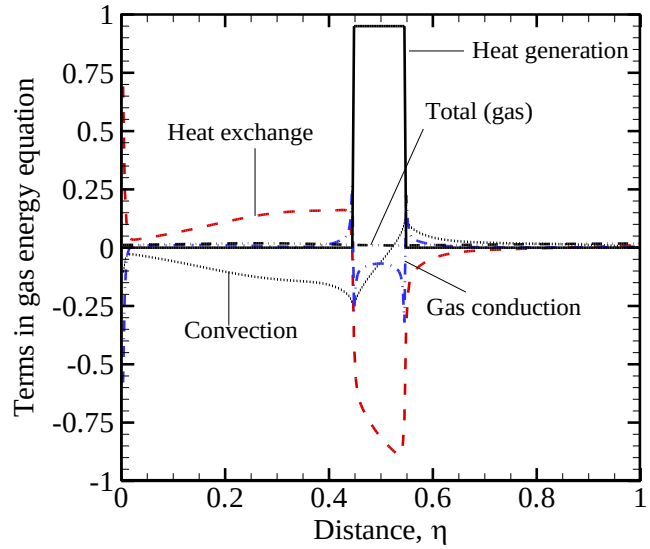

(a)

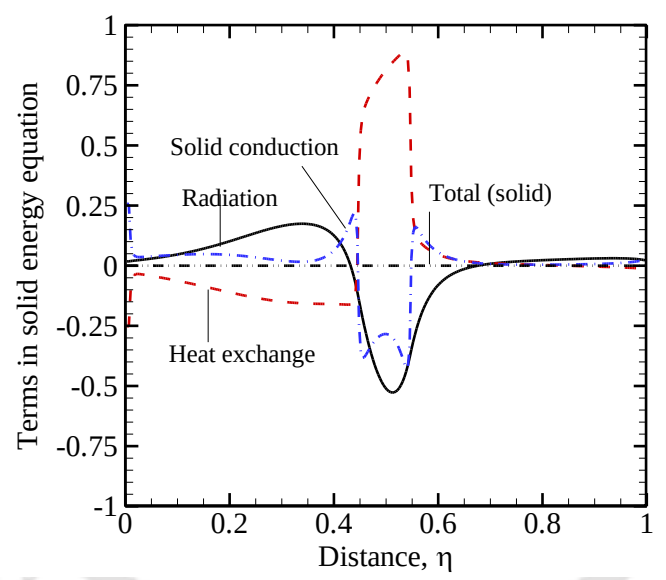

(b)

Figure 3.4: Comparison of different components in energy equations for $P_2 = 500$ and $\beta = 1000$ (a) gas energy equation and (b) solid energy equation

carried with gas stream towards the central zone, convection curve is negative. It rises to positive value on the downstream-side with the influx of energy in the heat generation zone. The large amount of energy received by the solid in the heat generation zone is dispersed by radiation and solid conduction. Very high temperature of the porous matrix in the heat generation zone causes significant emission of radiation in both upstream and downstream directions. Upstream-side temperature being lower, it receives higher amount of energy, and hence corresponding radiation term is positive. It is very much negative in

the heat generation zone due to the release of energy in both directions. Entry region, despite being at the lowest temperature, receives very little radiation energy due to high optical thickness. Solid conduction is also found to have substantial contribution, particularly in and around the heat-generation zone due to higher solid temperature. Both radiation and solid conduction profiles are negative in the heat generation zone, as energy is only released from this particular section due to high temperatures.

An important aspect to consider while using computational optimization tools, is the amount of computational time required during simulation. It is obvious that the CPU time should increase both with population size and number of generations. Computational time has been found to increase linearly with both the factors (Fig. 3.6). All runs were taken on 2.1 GHz processor with 2 GB RAM, and both results correspond to ε_e 0.9 and $\omega = 0.5$. Variation in the fitness function (objective function) with increasing number of generations is also an important consideration, as proper choice of the number of generations can save computational time, without affecting the accuracy of the results. As

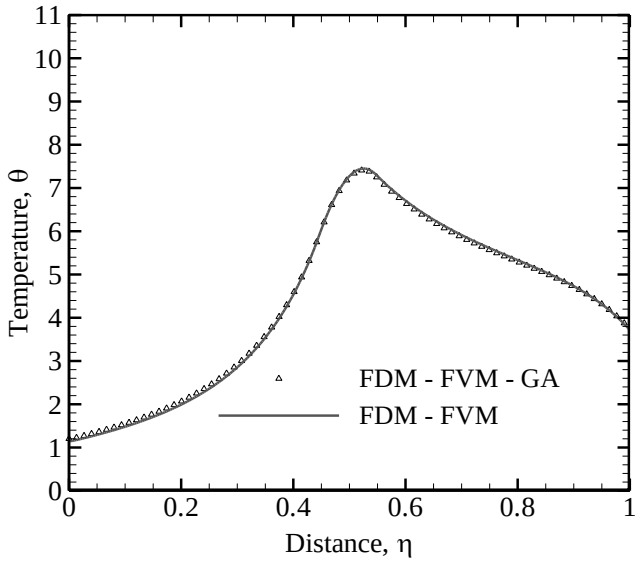

Figure 3.5: Comparison of non-dimensional gas or solid temperature from direct and inverse method

can be seen from Fig. 3.7, fitness function converges towards a satisfactory level after about 200 generations. Similarly, a population size of 75 can be found to be sufficient (Fig. 3.8). The effect of population size and number of generations on the accuracy of the

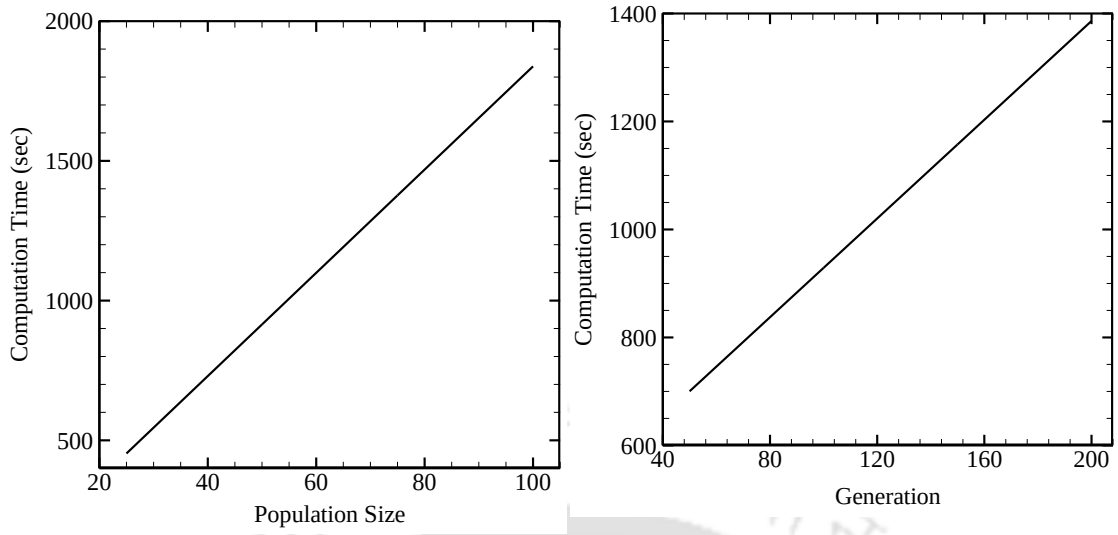

(a) (b)

Figure 3.6: Variation of the computational time involved in the inverse method with (a) population size for number of generations = 100 and (b) number of generations; population size = 50.

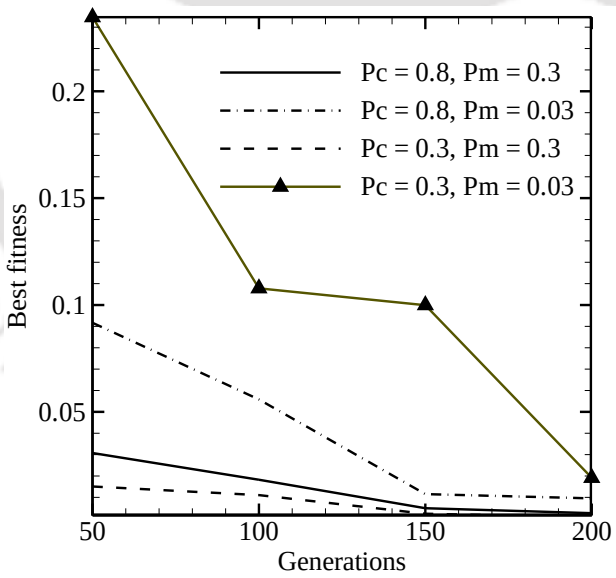

Figure 3.7: Effect of crossover probability and mutation probability on variations of best fitness with number of generations.

estimated parameters is summarized in Tables 3.3 and 3.4, respectively. Here, the measurement errors lie in the range of [0-5]. It is evident that the accuracy in the

Table 3.2. Estimated values of ε_e and β for different population size and generations.

Size	Generations	Estimated values of (ε_e, β)	Fitness function
100	50	(0.579079, 9.920512)	0.000632
200		(0.562116, 9.937569)	0.000005
300		(0.581497, 9.631286)	0.000013
400		(0.438786, 10.061989)	0.000002
100	100	(0.621322, 9.734553)	0.000004
200		(0.465693, 10.476927)	0.000087
300		(0.550000, 10.151184)	0.000003
400		(0.485526, 10.014625)	0.000004
100	150	(0.494759, 9.618251)	0.000047
200		(0.432738, 10.068141)	0.000002
300		(0.474768, 9.782056)	0.000007
400		(0.525722 9.974085)	0.000005
100	200	(0.634804, 9.556698)	0.000018
200		(0.581496, 10.205456)	0.000032
300		(0.567955, 9.931726)	0.000005
400		(0.639154, 9.860777)	0.000043

Table 3.3: Effect of population size and measurement error for exact value of (ε_e, ω) = (0.9, 0.5), number of generations = 200, $P_c = 0.80$ and $P_m = 0.03$.

Population size	± *E*	Estimated values of (ε_e, ω)	% Error in (ε_e, ω)	CPU time (s)
25	0	0.7702,0.383	-14.42,-23.4	510
	1	0.7262,0.3106	-19.31,-37.88	561
	2	0.7143,0.3394	-20.63,-32.11	589
	5	0.792,0.429	-12,-14.21	4100
50	0	0.7613,0.3738	-15.41,-25.24	948
	1	0.6758,0.2247	-24.91,-55.05	1059
	2	0.6178,0.151	-31.36,-69.81	1086
	5	0.8787,0.5022	-2.36,0.44	5351
75	0	0.5971,0.0341	-33.66,-93.17	1387
	1	0.619,0.0856	-31.22,-82.88	1569
	2	0.9004,0.5174	0.04,3.47	1834
	5	0.6287,0.1828	-30.15,-63.45	7086
100	0	0.9126,0.5082	1.4,1.63	2104
	1	0.795,0.4035	-11.67,-19.29	2316
	2	0.6224,0.1598	-30.84,-68.03	3434
	5	0.9743,0.5584	8.26,11.69	11603

measurement of ε_e and ω increases with larger choice for the population size, but at the expense of higher CPU time. Computational time also increases with increase in the measurement error. Proper choices for crossover probability and mutation probability are also important here. As is shown in Table 3.5 for a case with 200 number of generations

Table 3.4. Effect of number of generations and measurement error for exact value of (ε_e, ω) = (0.9, 0.5), population size = 100, $P_c = 0.80$ and $P_m = 0.03$.

Number of generations	± *E*	Estimated values of (ε_e, ω)	% Error in (ε_e, ω)	CPU time (s)
50	0	0.6016,0.0506	-33.16,-89.87	967
	1	0.8973,0.4922	0,-0.02	1045
	2	0.6991,0.351	-0.22,-0.3	1108
	5	0.9471,0.5369	0.05,0.07	1175
100	0	0.5945,0.0258	-33.94,-94.85	1917
	1	0.9224,0.5097	0.02,0.02	1993
	2	0.9874,0.5762	0.1,0.15	2217
	5	0.7984,0.4253	-0.11,-0.15	2269
150	0	0.882,0.4872	-1.99,-2.57	2175
	1	0.688,0.249	-0.24,-0.5	2210
	2	0.7908,0.45	-0.12,-0.1	2239
	5	0.7491,0.3755	-0.17,-0.25	2286
200	0	0.9232,0.5157	2.57,3.15	2214
	1	0.66,0.1901	-0.27,-0.62	2228
	2	0.6102,0.1763	-0.32,-0.65	2254
	5	0.7496,0.373	-0.17,-0.25	2333

Table 3.5. Effect of crossover probability P_c and mutation probability P_m for exact value of (ε_e, ω) = (0.9, 0.5); number of generations = 200, population size = 50.

P_c	P_m	Estimated values of (ε_e, ω)	% Error in (ε_e, ω)
0.3	0.3	0.7613,0.3738	-15.41,-25.24
0.3	0.03	0.5987,0.0349	-33.48,-93.02
0.8	0.3	0.7616,0.372	-15.38,-25.6
0.8	0.03	0.8104,0.4306	-9.96,-13.88

and a population size of 50, percentage error decreases with higher value of crossover probability. Crossover probability $P_c = 0.8$ and mutation probability $P_m = 0.03$ have been found to be sufficient for the porous matrix, under consideration.

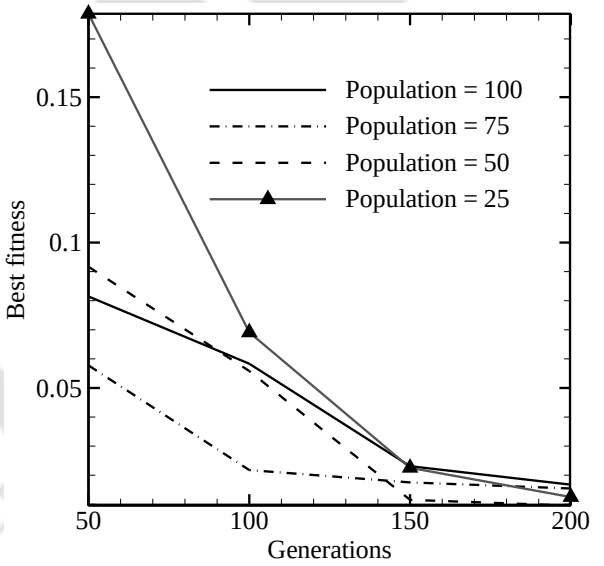

Figure 3.8: Effect of population size on variations of best fitness with number of generations.

3.3.2 Simultaneous estimation of three parameters

For the simultaneous estimation of three parameters, such as the emissivity ε_e, the scattering albedo ω and the non-dimensional solid conductivity P_4, the inverse analysis

utilizes knowledge of the gas temperature distribution $\theta_g(\eta)$, and the radiative heat flux Ψ_R and the convective heat flux Ψ_{conv} at the right $(\eta = 1.0)$ boundary of the porous matrix.

In the problem under consideration, the emissivity ε, the scattering albedo ω and the non-dimensional solid conduction P_4 are simultaneously estimated. In the estimation using the inverse analysis, the first objective function J_1 is constructed like the following:

$$J_1 = \sum_{i=1}^{N} \left(\tilde{\theta}_{g,i} - \theta_{g,i} \right)^2 \tag{3.13}$$

where $\tilde{\theta}_{g,i}$ and $\theta_{g,i}$ are the exact and unknown gas temperatures, respectively and N is the number of CVs. The second objective function J_2 is constructed as:

$$J_2 = \left(\tilde{\Psi}_{rad} - \Psi_{rad} \right)^2 + \left(\tilde{\Psi}_{conv} - \Psi_{conv} \right)^2 \tag{3.14}$$

where $\tilde{\Psi}_{rad}$ and Ψ_{rad} are the exact and the unknown radiative heat fluxes, respectively at the outer boundary $(\eta = 1)$ of the porous matrix, whereas $\tilde{\Psi}_{conv}$ and Ψ_{conv} are the exact and unknown convective heat fluxes, respectively at the same $(\eta = 1)$ location. With objective functions J_1 and J_2 defined as above, the new objective function J is defined as:

$$J = \frac{(2 \times J_1) + (N \times J_2)}{N + 2} \tag{3.15}$$

Accuracies of the estimated parameters in the GA depend on the population size and the number of generations, whereas in the GSA, the same depend on the number of starting points. Computational time also depends on these variables. With values of other parameters as listed in Table 3.1, results of simultaneous estimation of three parameters viz., $\varepsilon_e = 1.0$, $\omega = 0.5$ and $P_4 = 0.02$ using the GA and the GSA are presented in

Tables 3.6 and 3.7, respectively. Computational time corresponding to these variables are also shown.

In the GA, in Table 3.6, results are shown for 4 different values of the population size, viz., 50, 100, 150 and 200. For any population size, the number of generations considered are 50, 100, 150 and 200. In Table 3.7, in the GSA, the number of starting points considered are 100, 150, 200 and 250. Estimated values of each of the three parameters $(\varepsilon_e, \omega, P_4)$ under consideration and their percentage errors with respect to corresponding exact values $(\varepsilon_e = 0.9, \omega = 0.5, P_4 = 0.02)$ are also provided. Accuracy of results and associated computational time along with the convergence of fitness function are essential in judging the performance of the solution scheme. An observation of Tables 3.6 shows that in the GA, the estimations are best for population size 150 and the number of generations 200. The associated computational time is 4827 s. Computational time increases with increase in the population size and the number of generations. For the same level of accuracy, Table 3.7 shows that in the GSA, 100 starting points are good enough, and for this the associated computational time 628 s is almost 8 times lower than that of the GA.

For the problem under consideration, a better picture of variation of computational time in the GA emerges from the results shown in Figs. 3.9a and 3.9b. With 100 generations, variation of the computational time with population size is shown in Fig. 3.9a, and Fig. 3.9b shows this variation with the number of generations for the population size 50. With increase in the population size, increase in the computational time is almost linear. A similar trend is observed with increase in the number of generations. However, with 50 populations and 200 generations, the computational time 1256 s is 3 times less than that with 100 generations and population size 200.

Best fitness J (Eq. (3.15)) provides a better option for deciding on the final values of the generation and the population. It is observed from Fig. 3.10 that for any population, the best fitness decreases with increasing number of generations, and it is essential to have at least 200 generations to ensure sufficient accuracy $\mathrm{O}\left(10^{-4}\right)$. The population size of 150

is found to provide the best fitness among all considered cases, and hence can be suggested for optimization.

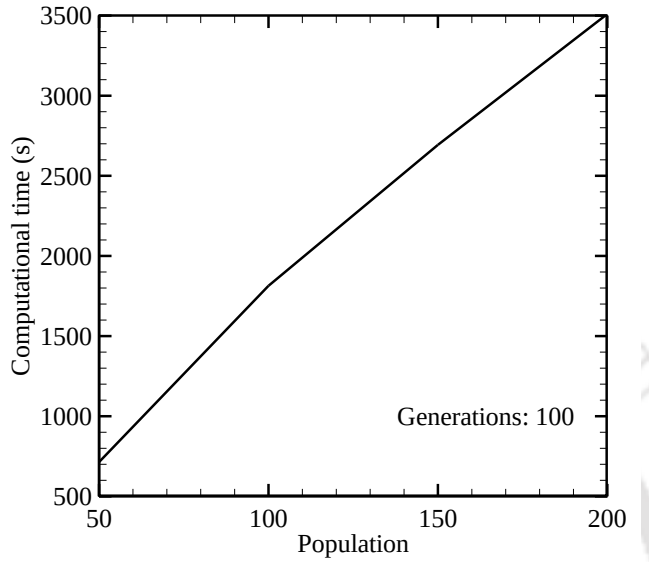

(a)

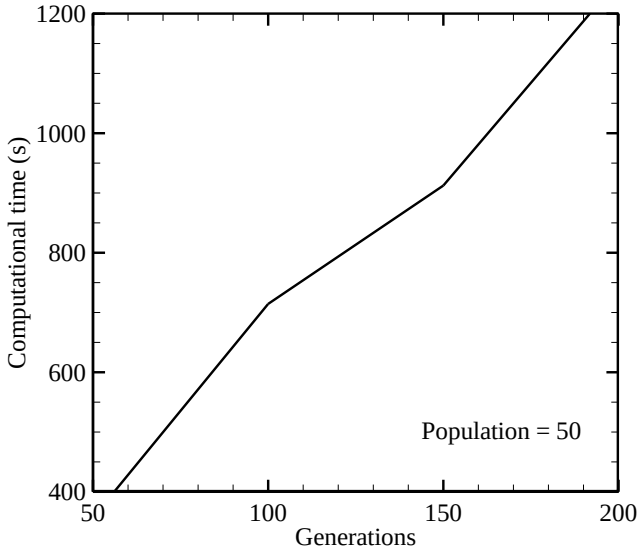

(b)

Figure 3.9. Variation of computational time with (a) population size and (b) number of generations in GA.

Table 3.6. Estimated values of ε_e, ω and P_4 for different population size and generations using the GA.

Population	Generations	Estimated value			% Error			Time (s)
		ε_e	ω	P_4	ε_e	ω	P_4	
50	50	0.8974	0.4876	0.0204	-0.2890	-2.4862	1.9250	357
	100	0.7654	0.0758	0.0267	-14.9513	-84.8362	33.2600	714
	150	0.9002	0.5004	0.0200	0.0221	0.0804	-0.0650	912
	200	0.8135	0.2501	0.0250	-9.6089	-49.9846	24.9650	1256
100	50	0.8275	0.2966	0.0249	-8.0509	-40.6770	24.7150	777
	100	0.8992	0.4978	0.0201	-0.0896	-0.4436	0.3950	1814
	150	0.8319	0.3041	0.0246	-7.5666	-39.1890	22.8100	2169
	200	0.9000	0.5000	0.0200	0.0009	-0.0076	0.0100	3287
150	50	0.8757	0.4300	0.0221	-2.6973	-14.0022	10.4450	1263
	100	0.9002	0.5002	0.0200	0.0249	0.0486	-0.0200	2693
	150	0.9002	0.5002	0.0200	0.0232	0.0450	-0.0150	3970
	200	0.9000	0.5000	0.0200	-0.0007	0.0016	-0.0050	4827
200	50	0.8966	0.4847	0.0200	-0.3770	-3.0510	0.0200	1687
	100	0.8992	0.4956	0.0201	-0.0874	-0.8840	0.6400	3510
	150	0.8991	0.4931	0.0203	-0.0978	-1.3784	1.3300	5083
	200	0.9001	0.4997	0.0200	0.0149	-0.0522	0.0800	4796

Table 3.7. Estimated values of ε_e, ω and P_4 for different number of starting points using the GSA.

Number of starting points	Estimated value			% Error			Time (s)
	ε_e	ω	P_4	ε_e	ω	P_4	
100	0.899986	0.500006	0.019999	-0.0016	0.0012	-0.005	628
150	0.899986	0.500004	0.019999	-0.0016	0.0008	-0.005	759
200	0.899988	0.500006	0.019999	-0.0013	0.0012	-0.005	980
250	0.899987	0.500006	0.019999	-0.0014	0.0012	-0.005	1358

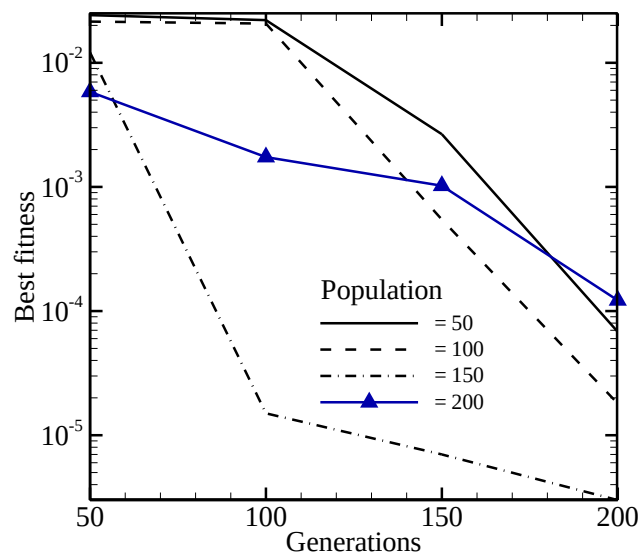

Figure 3.10. Effect of population size on variations of best fitness with number of generations for GA.

In the GSA, computational time depends on the number of initial points. It is observed from Fig. 3.11a that the computational time increases with increase in the number of

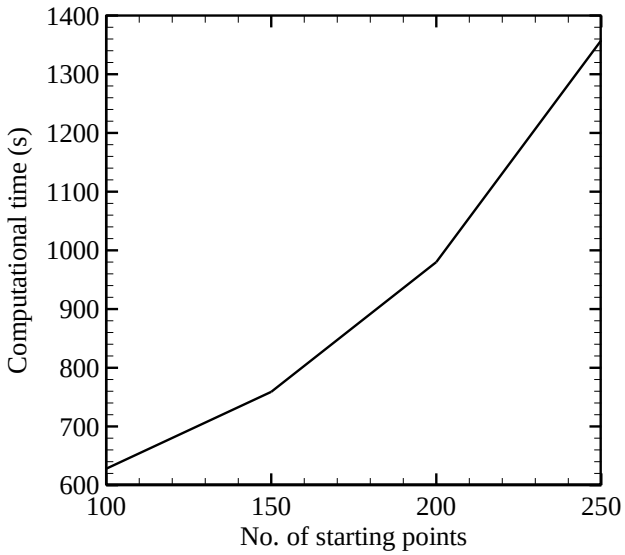

(a)

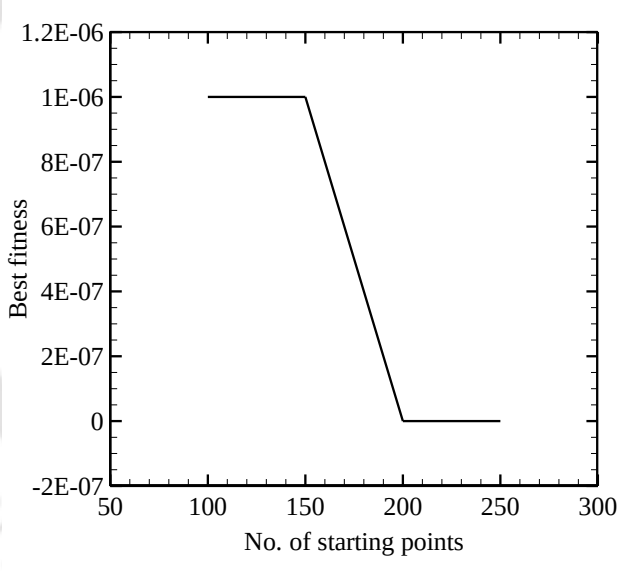

(b)

Figure 3.11. Variation (a) of computational time with number of starting points, and (b) best fitness with the number of starting points in GSA.

initial points, and this increase is steeper as this value increases. A comparison of Figs. 3.9a and 3.11a shows that the GSA is about 3 times faster than the GA. The variation of best fitness with the number of starting points is shown in Fig. 3.11b. It is observed that

for the number of starting points 200, the best fitness is almost zero, making GSA a better choice compared to GA in terms of solution accuracy.

To have a better idea of the how the best fitness J varies with the computational time in the GA and the GSA, comparison is shown in Fig. 3.12. It is observed that in comparison to the GA, the best fitness for the GSA remains almost constant with value approximately 10^{-7}. This observation further substantiate that for the problem under consideration, the GSA has an edge over the GA.

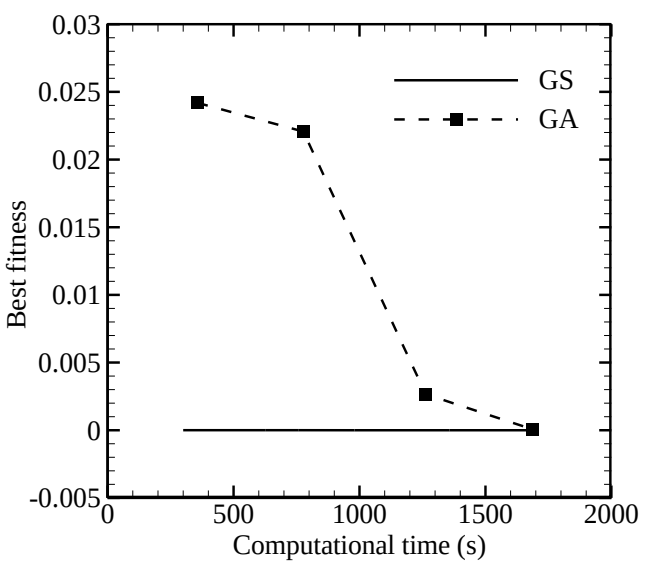

Figure 3.12. Variation of best fitness with computational time.

3.4 Summary

Combined mode conduction and radiation heat transfer in a 1-D planar porous medium was studied. A centrally located uniform volumetric heat generation zone acted as the source of energy in the medium. To account for the non-local thermal equilibrium, separate energy equations for gas-phase and solid-phase were considered. With volumetric radiative term appearing in the solid-phase energy equation computed using the DTM, the gas- and the solid-phase energy equations were simultaneously solved using the FDM. In the direct method, effects of convective coupling and extinction

coefficient on gas and solid temperatures, and various terms in the energy equations were analyzed.

- Two parameters (β, ε) and (ω, ε) were simultaneously estimated by employing the GA as the optimization tool in the inverse analysis.
- Effects of measurement error and other GA parameters such as, population size, number of generation, crossover probability and mutation probability, on variations of the best fitness with the number of generations were also studied.
- Effects of population size and number of generations on CPU time was also studied.
- Simultaneous estimation of three parameters, viz., emissivity ε_e, scattering albedo ω and non-dimensional thermal conductivity P_4 was carried out in the inverse analysis, by employing the GA and the GSA.
- For the same level of accuracy, the GSA was found to be computationally much more efficient than the GA.

Chapter 4

1-D PLANAR POROUS MEDIUM WITH COMBUSTION

4.1 Introduction

In the present Chapter, a more realistic model of 1D-planar PRB is developed. Instead of single stage porous matrix, a two stage porous matrix with different porosity for the upstream and downstream section is used. The properties of the two porous matrixes are used based on correlations available in the literature. The heat generation zone of the model developed in the previous Chapters is replaced by simulation of combustion of methane gas by using single step global mechanism. Moreover motivated by the findings of the Chapter 2, that GSA was performing better than the GA, in the present Chapter more wide search for better optimization algorithms is done.

Intricate design of the PRBs necessitates the simultaneous identification of several parameters like porosity, pore diameter, solid and gas conductivity, radiative properties of both phases, equivalence ratio of the combustible mixture etc., for maximizing its performance. Inverse analysis can play a crucial role precisely in this context. Using prior knowledge/guess about the possible/required outputs, such as temperature profiles and/or heat flux components, an objective function can be constructed, which is subsequently minimized employing a suitable algorithm. One important point to note here is that the inverse analysis is a computer-intensive procedure and different optimization algorithm may respond differently for any given problem. Hence it is imperative to identify the best optimization algorithm concerned with PRBs and present work focuses on the same. The study considers a one-dimensional, premixed methane-air flame model. Combustion is simulated using a single-step, irreversible reaction. Radiative information is computed by numerically solving radiative transport equation (RTE) using discrete transfer method (DTM). Several optimization tools are used here for comparison, namely, genetic

algorithm (GA), genetic algorithm parallel (GAP), pattern search algorithm (PSA), pattern search algorithm parallel (PSAP), multiple starting point algorithm parallel (MSPAP), simulated annealing algorithm (SAA) and global search algorithm (GSA). Effort is made to identify the best one in terms of computational time requirement and accuracy of solution during simultaneous estimation of one to three parameters, including gas phase velocity, downstream pore diameter and scattering albedo.

4.2 Formulation

Schematic of a two-layer porous matrix (PM) under consideration is shown Fig. 4.1(a). It consists of a preheating zone (PZ) (thickness: 3.5 cm, pore density = 25.6 ppc, Pore diameter, $d_p = 0.029$ cm, Porosity, $\phi =$ 0.835, scattering albedo, $\omega = 0.8$) and a combustion zone (CZ) (thickness: 2.55 cm, pore density = 3.9 ppc, Pore diameter, $d_p =$ 0.152 cm, porosity, $\phi =$ 0.87, and scattering albedo, $\omega = 0.8$). Methane-air mixture flows through the two-layer PM, and it gets preheated in the PZ. Combustion starts at the interface of the two layer, and spreads to the entire volume of the CZ. A single-step reaction chemistry is used to simulate the combustion of methane. Considering each mole of oxygen in air to be accompanied by 3.76 moles of nitrogen, the relevant chemical reaction can be written as

$$\mathrm{CH_4} + \underbrace{2\mathrm{O_2} + 2(3.76)\mathrm{N_2}}_{\text{Air}} \Rightarrow \mathrm{CO_2} + 2\mathrm{H_2O} + 2(3.76)\mathrm{N_2} \tag{4.1}$$

The reaction constant for the above equation is $k_c = 1.8\times10^8 \exp\left(\frac{-125600}{RT_g}\right)[\mathrm{CH_4}]\,\mathrm{mol\cdot m^{-3}\cdot s^{-1}}$, and the equivalence ratio is taken to be 0.65.

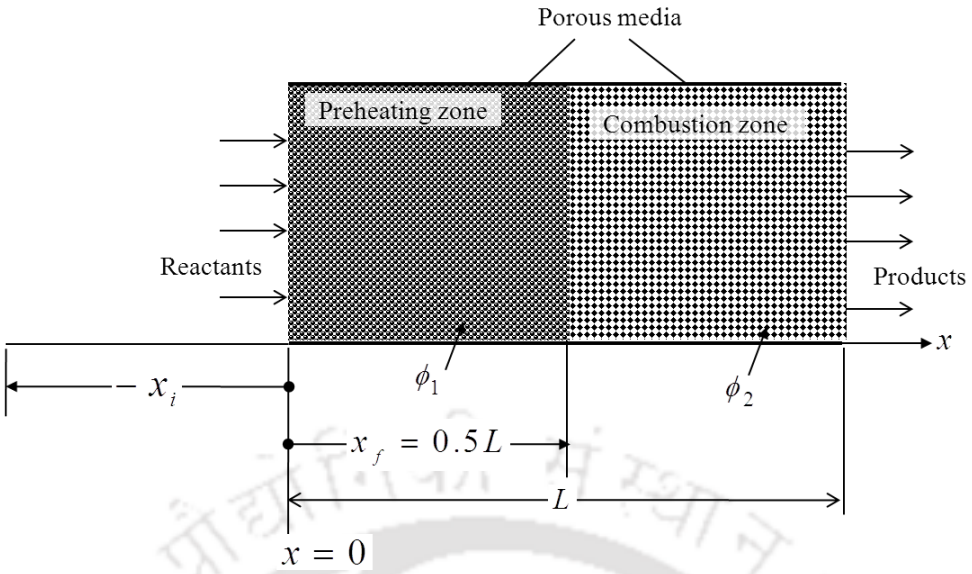

(a)

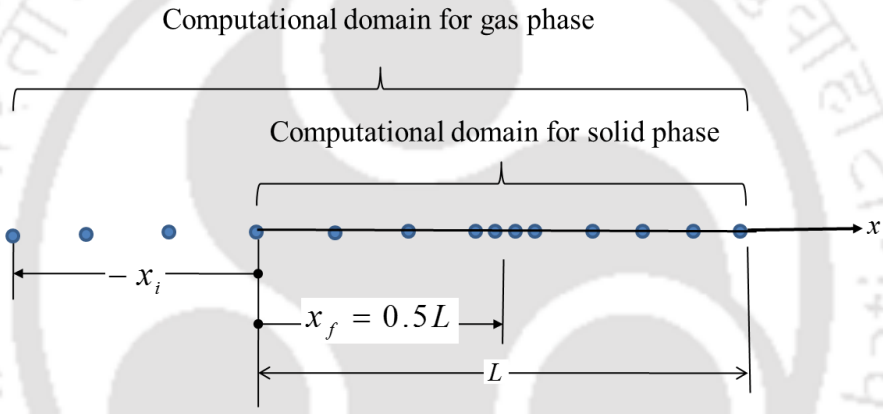

$$C\left(\frac{\Delta x_{i+1}}{\Delta x_i}\right) = \begin{cases} 0.1429, \text{for } x = 0.5L \\ 7.0, \quad \text{for } x = 0.7L \\ 1.0, \text{for all other values of } x \end{cases}$$

(b)

Figure 4.1. (a) Schematic of two-layer porous matrix with computational domain $(-x_i \le x \le x_e)$, and (b) computational domain.

In the PM, exothermic reaction (Eq. (4.1)) is the source of energy, and this causes manifestation of all three modes of heat transfer, i.e., conduction, convection and radiation. In the reaction zone, and in its downstream, the gas temperature is more than that of the solid, thus the convective heat transfer is from the gas to the solid. In upstream of the reaction zone, i.e., in the PZ, opposite is the case. In the PZ, heat transfer by conduction and volumetric radiation increases the temperature of the solid. Thus,

throughout the PM, non-local thermal equilibrium between the two phases exists. This necessitates consideration of separate energy equations for the gas and the solid phases. The solid phase is radiatively participating, while the gas phase remains transparent to it. Thus to account for the radiative heat transfer, the volumetric radiative source term appears only in the solid phase energy equation.

With ϕ as the porosity, ρ_g as the density of the gas, u as the mixture velocity, A as the pores surface area per unit volume of porous matrix, $\dot{\omega}_k$ as the molecular generation rate for k_{th} species, h as the heat transfer coefficient, k_g as the thermal conductivity of the gas and k_s as the thermal conductivity of the solid and q_R as the radiative heat flux, for the problem under consideration, the relevant conservation equations and boundary conditions are the following:

Continuity equation: $$\frac{d(\phi\rho \mathrm{u})}{dx} = 0 \tag{4.2}$$

Gas-phase energy equation:

$$\phi\rho_g c_g u\frac{dT_g}{dx} + (1-\phi)Ah(T_g - T_s) = -\phi\sum_{k=1}^{N_s}\dot{\omega}_k h_k + \phi k_g\frac{d^2T_g}{dx^2} \tag{4.3}$$

Solid-phase energy equation: $$(1-\phi)Ah(T_g - T_s) = (1-\phi)k_s\frac{d^2T_s}{dx^2} - \frac{dq_R}{dx} \tag{4.4}$$

Species conservation equation: $$\frac{d(\phi\rho u Y_k)}{dx} = \frac{d\left(\phi k_g\frac{dY_k}{dx}\right)}{dx} + \dot{\omega}_k, \qquad k \in [1, \mathrm{N}_s] \tag{4.5}$$

Equation of state: $$\rho = \frac{\bar{W}p}{RT_g} \tag{4.6}$$

where $\bar{W}$ is the mixture-averaged molecular weight, and is given by

$$\bar{W} = \sum_{k=1}^{N_s} W_k X_k \tag{4.7}$$

In Eq. (4.4), the radiative source term $\frac{dq_R}{dx}$ is given by

$$\frac{dq_R}{dx} = (1-\omega)\beta\left(4\sigma T^4 - G\right) \tag{4.8}$$

where ω is the scattering albedo, β is the extinction coefficient, $\sigma = 5.67\times10^{-8}\,\mathrm{W\cdot m^{-2}\cdot K^{-4}}$ is the Stefan-Boltzmann constant and G is the incident radiation.

Solutions of the governing equations (4.3), (4.4), (4.5) and (4.8) requires boundary conditions. These are the following:

Gas-phase energy equation (Eq. (4.3)):
$$T_g\Big|_{-x_i} = 300K, \quad \frac{dT_g}{dx}\Big|_{x=L} = 0.0 \tag{4.9a}$$

Solid-phase energy equation (Eq. (4.4)):
$$-k_s\frac{dT_s}{dz}\Big|_{z=0} = hA(T_g - T_s), k_s\frac{dT_s}{dz}\Big|_{z=L} = hA(T_g - T_s) \tag{4.9b}$$

Species conservation equation (Eq. (4.5)):
$$Y_k\Big|_{x=-x_i} = Y_{k,i}, \quad \frac{dY_k}{dx}\Big|_{x=L} = 0.0 \tag{4.9c}$$

West boundary:
$$I_{0,W} = \varepsilon\frac{\sigma T^4}{\pi} + \frac{(1-\varepsilon)}{\pi}\sum_{m=1}^{\frac{M}{2}} I^m \sin\alpha^m \cos\alpha^m \sin(\Delta\alpha) \tag{4.9d}$$

East boundary:
$$I_{0,E} = \varepsilon\frac{\sigma T^4}{\pi} + \frac{(1-\varepsilon)}{\pi}\sum_{m=\frac{M}{2}}^{M} I^m \sin\alpha^m \cos\alpha^m \sin(\Delta\alpha) \tag{4.9e}$$

4.2.1 Solution Procedure

With volumetric radiative information $\frac{dq_R}{dx}$ needed in the solid-phase equation computed using the DTM, subject to the boundary conditions, Eqs. (4.9a) – (4.9c), conservation

equations (4.2) - (4.5) are solved simultaneously using the FDM. Computational domains for the gas and the solid phases are shown in Fig. 4.1b. 300 equally spaced nodes are used each within the CZ, for both solid and the gas phase energy equations. Apart from CZ, 200 and 400 nodes were taken for the sold and the gas phase, respectively, while 20 number of rays were found to be perfect. With geometric parameter values outlines before, based on Hsu and Howell [123], the following correlations were used to compute thermal conductivity k_s, extinction coefficient β of the PM, and heat transfer coefficient h [124] between solid and gas.

$$k_s\left(d_p\right) = 0.188 - 17.5 d_p \tag{4.10}$$

$$\beta(d_p) = \frac{0.0044}{d_p}(1-\phi) \tag{4.11}$$

$$Nu = \frac{Ah\, {d_p}^2}{k_g} = 0.819\left[1 - 7.33\left(\frac{d_p}{L}\right) Re^{0.36\left\{1+15.5\left({}^{d_p}/_{L}\right)\right\}}\right] \tag{4.12}$$

where with μ as the viscosity, the Reynolds number Re is [124]

$$\mathrm{Re} = \frac{\rho u d_p}{\mu} \tag{4.13}$$

Simultaneous solution of the conservation equations (Eqs. (4.3) - (4.5)), is iterative. At every iteration, radiative information $\frac{dq_R}{dx}$ needed in the solid-phase energy equation is computed first. In the first iteration, the temperature field for the solid and the gas phases are guessed, and the

governing equations are solved simultaneously by Gauss-Seidel method. The iterative process continues till the desired convergence level is attained. This required the attainment of each of the following three criterion: (a) change in T_g at $x = 0$ is $\leq 10^{-6}$, (b) change in $\frac{dT_g}{dx}$ at $x = 0$ $\leq 10^{-6}$, and (c) overall energy balance is less than 0.1%.

Towards simultaneous estimation of parameters, and performance evaluation of the optimization methods, the objective functions are constructed first. With $\tilde{\theta}_{g,i}$ and $\tilde{\theta}_{s,i}$ as the gas and the solid temperatures, respectively known at every node i, and as the convective heat flux $\tilde{q}_{conv,e}$ and the radiative heat flux $\tilde{q}_{rad,e}$ also known at the exit point $(x = L)$, the objective function are the following:

$$J_1 = \sum_{i=1}^{N} \left(\tilde{\theta}_{g,i} - \theta_{g,i} \right)^2 \tag{4.14a}$$

$$J_2 = \sum_{i=1}^{N} \left(\tilde{\theta}_{s,i} - \theta_{s,i} \right)^2 \tag{4.14b}$$

$$J_3 = \frac{J_1 + J_2}{2} \tag{4.14c}$$

$$J_4 = \left(\tilde{q}_{conv,e} - q_{conv,e} \right)^2 + \left(\tilde{q}_{rad,e} - q_{rad,e} \right)^2 \tag{4.14d}$$

$$J = \frac{\left(2 \times J_3 \right) + \left(N \times J_4 \right)}{2} \tag{4.14e}$$

The known values in Eqs. (4.14a) – (4.14e) required to define the objective function are computed through the direct method.

4.3 Results and Discussion

For the geometric parameters stated before, with $u = 0.45\,\text{m/s}$, solid temperature distribution resulting from combustion of methane is compared with the experimental results (Fig. 4.2) [125]. Separate measurements of the gas- and the solid-phase temperatures in an experimental setup is difficult, and is not available in the literature. Because of this, for the validation of the present numerical model, a qualitative trend with the experimental data is shown. Use of qualitative trend of the experimental data for the validation purpose for such complicated cases is also reported in [50, 126, 127].

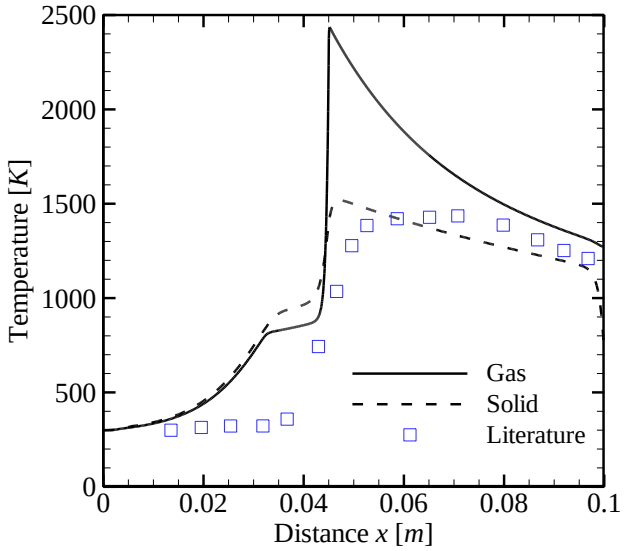

Figure 4.2. Comparison of temperature distribution with experimental results [125].

In the present work, in the simultaneous estimation of parameters, apart from the distribution of solid and gas temperature distributions, knowledge about convective and radiative heat fluxes at the outer boundary of the of PM is also needed. Distributions of convective and radiative heat fluxes, along with the distributions of conductive gas and solid heat fluxes are shown in Fig. 4.3. All the parameters required for the simulation are listed in Table 4.1. It is concluded from the Fig. 4.3, that conductive heat fluxes both in the gas- and the solid-phase are low due to low thermal conductivity of gas and the ceramic, while convective and radiative components are high, and thus they are more important in the study of PRBs.

Results on estimation of the scattering albedo ω, using optimization algorithms, viz., GSA, SAA, MSPAP, GA, GAP, PAS and PSAP are shown in quantitatively in Table 4.2, and qualitatively in Fig. 4.4. CPU times (s) of these methods are also shown. All runs were taken on 2.1 GHz processor with 2 GB RAM. All algorithms are able to estimate ω with a very good accuracy. However, computationally, PSA is the most efficient, and the GSA, the most time consuming.

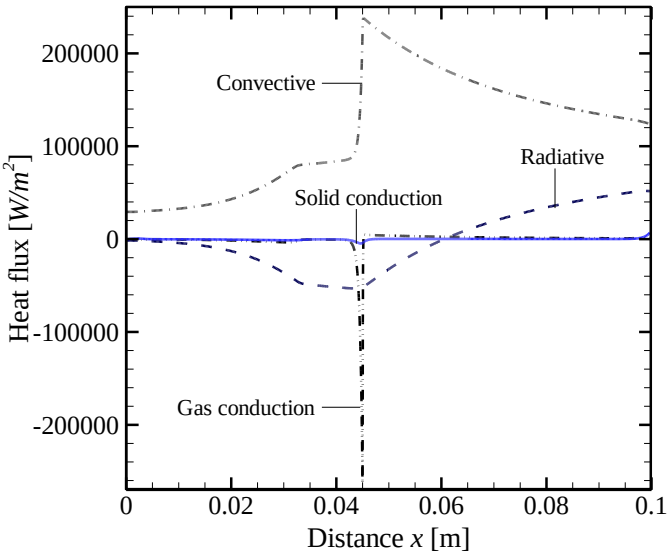

Figure 4.3. Different heat fluxes in the PRB.

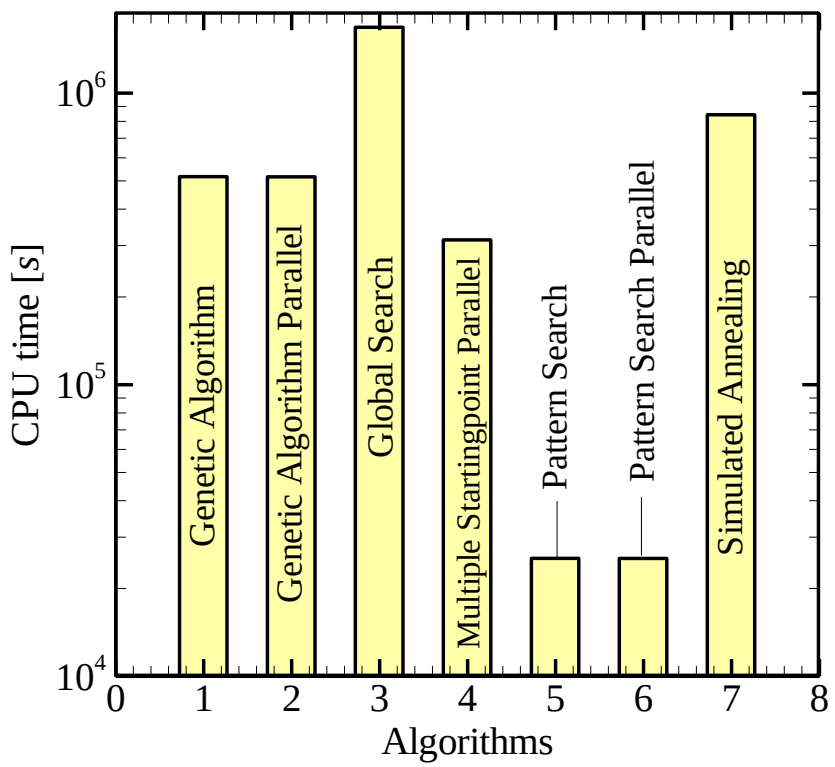

Figure 4.4. Performance comparison of various optimization algorithm.

Table 4.1. Parameter values used for simulations.

Property	Upstream	Downstream
Pore density	25.6 ppc	3.9 ppc
Pore diameter, d_p	0.029 cm	0.152 cm
Porosity, ϕ	0.835	0.87
Scattering albedo, ω	0.8	0.8
Length of porous matrix	3.5 cm	2.55 cm

Having known that among 7 optimization tools, the PSA is computationally the most efficient, next variation in CPU time with increase in 1 parameter to the simultaneous estimation of 2 and 3 parameters is shown. In Table 4.3 and Fig. 4.5 show these results. The gas velocity u, the scattering albedo ω and the downstream pore diameter d are the parameters of concern. It is observed that the simultaneous estimation of two parameter estimation takes more time than that for the three parameters.

Table 4.4 shows how CPU time and accuracy depend on the selection of a parameter. Two different cases are studied, in one case, the scattering albedo ω, the downstream pore diameter d and the gas velocity u are simultaneously estimated, while in the second case, the scattering albedo ω is replaced with stoichiometric ratio Φ. It is noticed that, in the second case, estimation is better and reduction in CPU time is significant. Multiplying the objective function with a number (multiplying factor (MF)) alters the computation time. With PSAP, this change is shown in Fig. 4.6. Drastic reduction in CPU time is observed.

Performances of MSPA, GA, PSA and GSA in the simultaneous estimation of three parameters, viz., stoichiometric ratio Φ, downstream pore diameter d and the gas velocity u are presented in Table 4.5 and Fig. 4.7. It is observed that for three parameter estimation, GA gives most accurate result. In one test case, experimental data is used to fabricate objective function. PSA is able to estimate the gas velocity with very high accuracy and in very less time. The details of the performance are shown in Table 4.6.

Table 4.2. Comparison of different optimization algorithm for true value of $\omega = 0.8$.

Different Optimization Techniques	**Estimated** ω	**% Error in Estimation of** ω	**Best fitness** $F(\times 10^{-6})$	**CPU Time (s)**
Global Search Algorithm	0.7999	-0.001	16	1022994
Simulated Annealing	0.7999	-0.002	19	509983
Multiple Starting point Algorithm Parallel	0.7999	-0.001	16	216644
Genetic Algorithm	0.7999	-0.003	24	89614
Genetic Algorithm Parallel	0.8000	0.006	47	86010
Pattern Search Algorithm Parallel	0.7999	0.000	16	9981
Pattern Search Algorithm	0.7999	0.000	16	9962

Table 4.3. Estimated values of ω, d and u using the PSA.

No. of parameter estimated	**True value**			**Estimated values**			**% Error in estimated values**			**Best fitness** f $(\times 10^{-6})$	**CPU Time (s)**
	ω	d $(\times 10^{-3})$ [m]	u [m/s]	ω	d $(\times 10^{-3})$ [m]	u [m/s]	ω	d	u		
1	0.8			0.7999			-0.0003			16	9962
2	0.8	1.52		0.4970	1.83		-37.8663	20.3998		8265	225856
3	0.8	1.52	0.45	0.3717	1.875	0.4480	-53.5375	23.3552	-0.43289	4159	128308

Table 4.4. Effect of selection of parameters for estimation, on PSA.

Parameters estimated	**% Error in parameters**			**Total Error** $E\left(=\sqrt{E_1^2+E_2^2+E_3^2}\right)$	**Best fitness** $f\ (\times 10^{-6})$	**CPU Time (s)**
	E_1	E_2	E_3			
$\omega, \mathrm{d}, \mathrm{u}$	-53.53	23.35	-0.43	58.41	4159	128308
$\Phi, \mathrm{d}, \mathrm{u}$	-23.07	0.00	0.00	23.07	2	26945

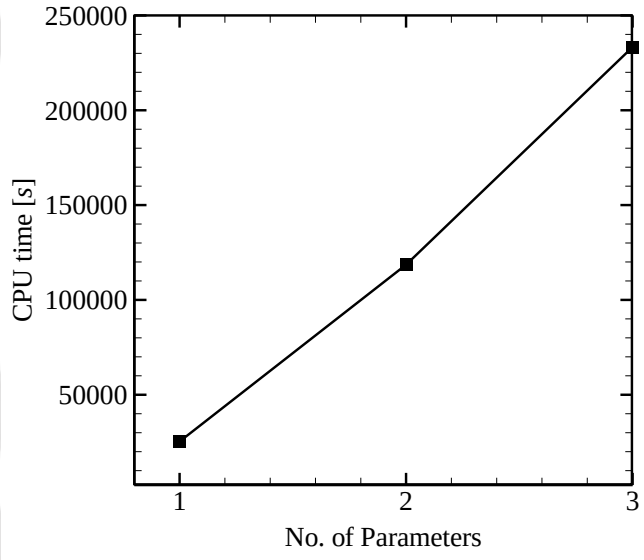

Figure 4.5. Relation between number of estimated parameters and CPU time (s) for PSAP.

Table 4.5. Performance comparison of different optimization techniques on estimation three parameters.

Different Optimization Techniques	**True value**			**Estimated value**			**% Error in estimation**			**Total Error** E $\left(=\sqrt{E_1^2+E_2^2+E_3^2}\right)$	**Best fitness** $f\ (\times 10^{-6})$	**CPU Time (s)**
	Φ	d $(\times 10^{-3})$ [m]	u[m/s]	Φ	d $(\times 10^{-3})$ [m]	u[m/s]	$\Phi(E_1)$	$d\,(E_2)$	$u\,(E_3)$			
Multiple Starting point Algorithm	0.65	1.52	0.45	0.0564	1.5199	0.4499	-91.32	0.00	0.00	91.32	1	365726
Genetic Algorithm	0.65	1.52	0.45	0.6883	1.5201	0.4501	5.90	0.01	0.03	5.90	446	145431
Pattern Search Algorithm	0.65	1.52	0.45	0.5000	1.5199	0.4499	-23.07	0.00	0.00	23.07	2	26945
Global Search Algorithm	0.65	1.52	0.45	0.9953	1.5199	0.4499	53.13	0.00	0.00	53.13	1	894567

Table 4.6. Use of Pattern search algorithm for estimation of parameter using experimental.

True value of Φ	Estimated value of Φ	% Error in estimation of Φ	Best fitness f	CPU Time (s)
0.65	0.65	0.00	18.93	9793

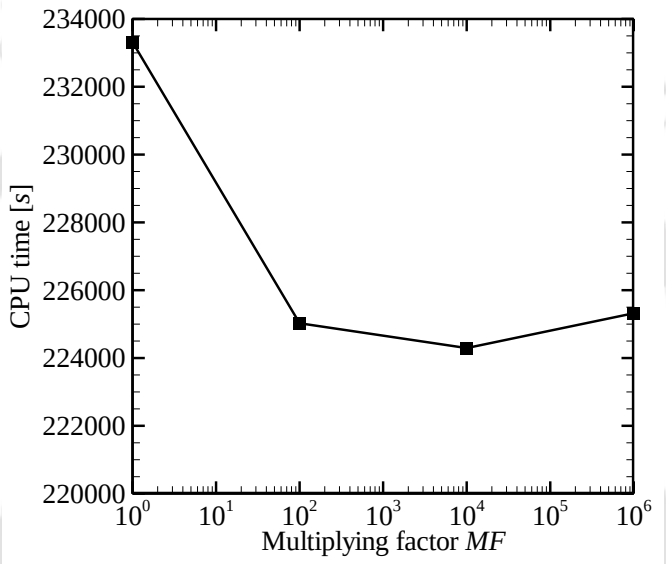

Figure 4.6. Relation between Multiplying factor and CPU time (s) for PSAP.

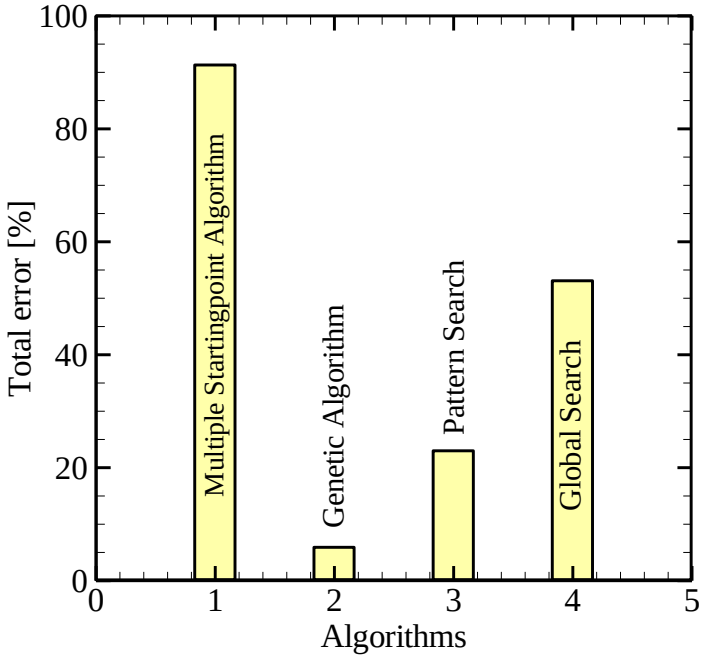

Figure 4.7. Comparison of different optimization algorithms in estimation of three parameters.

4. 4 Summary

Attention was given to the inverse analysis of two layered 1D planar PRB. Combustion of methane was simulated by single step mechanism. The RTE was solved using the DTM and other governing equations was solved by the FVM. The objective function was constructed by utilizing the gas- and the solid- phase temperature, and convective and radiative heat flux at the outer (downstream) surface of the PRB. Performances of 7 different optimization algorithms in estimation of single and/or simultaneous estimation of two as well as three parameters were assessed. All optimization methods estimated scattering albedo with a high accuracy. However, computationally, PSA was the best. Multiplying the objective function with a suitable number was found to reduce the computational time drastically. Effect of increasing the number of estimated parameters on the CPU time (s) was also studied. With increase in number of parameters, CPU time increased significantly.GA was found to give better accuracy in simultaneous estimation of three parameters. PSA provided highly accurate estimation of one variable using experimental data.

Chapter 5

2-D RECTANGULAR POROUS MEDIUM WITH HEAT GENERATION

5.1 Introduction

In the previous Chapters, a robust model of 1D-planar PRB was developed and performance of various optimization algorithms was accessed. Moving to the direction of more realistic numerical model, in the present Chapter, a 2D-rectangular model of PRB is developed.

Present work focuses on numerically simulating a 2-D porous matrix. Separate energy equations for the gas and solid phases are considered to account for local thermal non-equilibrium, with coupling through convective heat exchange. Combustion is modeled in the form of a centrally-located zone of constant volumetric heat generation. The volumetric radiative information for the solid materials is estimated following finite volume method (FVM). Finite difference (FDM) solution of energy equations provides the gas and solid temperature profiles, which are used as inputs to formulate the objective function for the inverse analysis.

Genetic algorithm (GA) is used to minimize the objective function and simultaneous optimization of two optical properties, namely, emissivity at the right edge and scattering albedo, of the porous structure is performed. Next, in an attempt to estimate four parameters, the objective function is modified using the radiative and convective heat flux distribution along the $y-$direction at the exit of the porous matrix. Two optimization algorithms the GA, and the GSA are employed and compared in the minimization of objective function. Four properties are simultaneously estimated, namely, emissivity,

scattering albedo, non-dimensional solid conduction and dimensionless convective heat transfer coefficient. The GSA performs better than the GA.

5.2 Formulation

Schematic representation of the geometry under consideration is shown in Fig. 5.1(a). A rectangular porous matrix is selected as the computational domain, with gas flowing through it from the left. Combustion is simulated incorporating a zone of heat generation at the center of the matrix. The solid is assumed to be radiatively absorbing, emitting and isotropically scattering, while the gas is radiatively non-participating. Gas and solid phases are in thermal non-equilibrium, necessitating two separate energy equations for either phase. The phases are convectively coupled to facilitate thermal interaction between them. Accordingly the steady-state energy equations for both the phases are the followings.

$$\text{Gas phase: } \phi\rho_g c_g u\frac{\partial T_g}{\partial x} + (1-\phi)Ah(T_g - T_s) = \phi\dot{Q}\delta(x) + \phi k_g\left(\frac{\partial^2 T_g}{\partial x^2} + \frac{\partial^2 T_g}{\partial y^2}\right) \tag{5.1a}$$

$$\text{Solid phase: } (1-\phi)Ah(T_g - T_s) + (1-\phi)k_s\left(\frac{\partial^2 T_s}{\partial x^2} + \frac{\partial^2 T_s}{\partial y^2}\right) - \nabla\cdot q_R = 0 \tag{5.1b}$$

Here the volumetric heat generation rate per unit volume ($\dot{Q}$) is applicable only for the simulated combustion zone and that is achieved using the Dirac-delta function $\delta(x)$, which is defined as unity for $0.45L_x < x \le 0.55L_x$ and zero elsewhere. The solid phase participates in radiation via the volumetric radiation term $\nabla\cdot q_R$ appearing solely in Eq. (5.1b) and is computed by the FVM.

Energy equations for both the phases can simultaneously be solved by computing the volumetric radiation term. In order to generalize the problem, conservation equations are non-dimensionalized employing the following definitions.

$$\theta=\frac{T-T_i}{T_i} \qquad \eta_x=\frac{x}{L_x} \qquad \eta_y=\frac{y}{L_x} \qquad \Psi_R=\frac{q_R}{\dot{Q}L_x} \qquad P_1=\frac{\rho_g c_g u T_i}{\dot{Q}L_x}$$

$$P_2=\frac{hAT_i}{\dot{Q}} \qquad P_3=\frac{k_g T_i}{\dot{Q}L_x^2} \qquad P_4=\frac{k_s T_i}{\dot{Q}L_x^2} \qquad P_5=\frac{hL_x}{k} \tag{5.2}$$

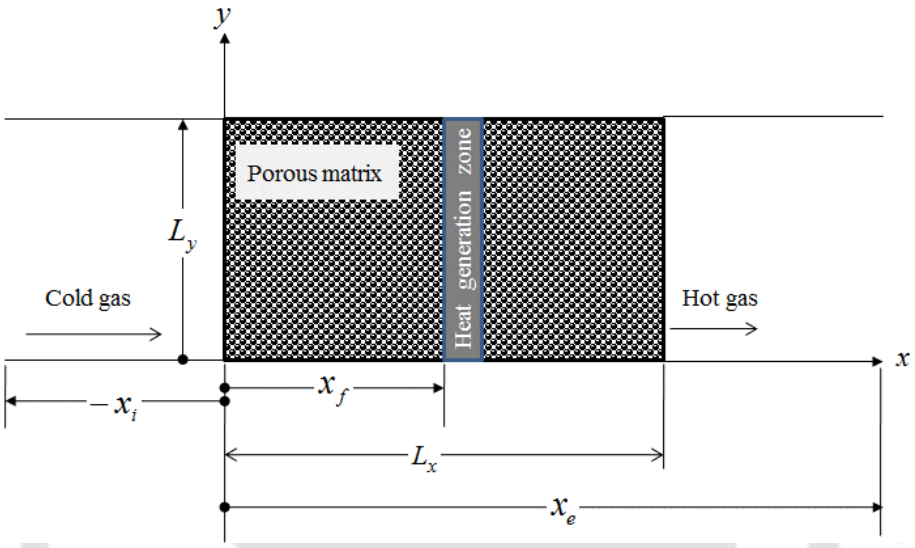

(a)

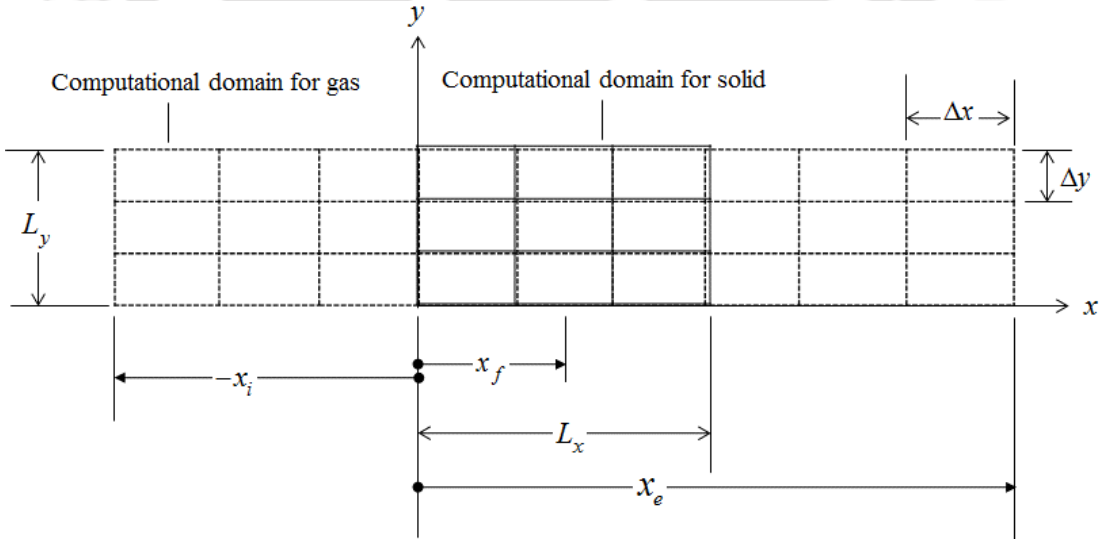

(c)

Figure 5.1. (a) Schematic of the porous matrix and (b) computational domain $(-x_i \le x \le x_e)$ and coordinate system used.

Accordingly the non-dimensional forms of governing equations yields:

$$\text{Gas phase: } \phi P_1 \frac{\partial \theta_g}{\partial \eta_x} + (1-\phi) P_2 (\theta_g - \theta_s) = \phi \delta(\eta_x) + \phi P_3 \left(\frac{\partial^2 \theta_g}{\partial \eta_x^{\,2}} + \frac{\partial^2 \theta_g}{\partial \eta_y^{\,2}} \right) \tag{5.3a}$$

$$\text{Solid phase: } (1-\phi) P_2 (\theta_g - \theta_s) + (1-\phi) P_4 \left(\frac{\partial^2 \theta_s}{\partial \eta_x^2} + \frac{\partial^2 \theta_s}{\partial \eta_y^2} \right) - \nabla \cdot \Psi_R = 0 \tag{5.3b}$$

The computational domain for the solid phase coincides with the porous matrix, i.e., $0 \le x \le L_x$, whereas the same for the gas phase is extended to $-x_i$ on the left and x_e on the right to counter the upstream and downstream energy transport through conduction and radiation. Gas is considered to enter the simulation zone at the ambient temperature, while zero gradient condition is assumed to prevail at the exit section. Accordingly the non-dimensional boundary conditions for the gas energy equation can summarized as:

$$\begin{aligned} &\theta_g = 0 \text{ at } \eta_x = \eta_{x,e} && \frac{\partial \theta_g}{\partial \eta_x} = 0 \text{ at } \eta_x = \eta_{x,e} \\ &\frac{\partial \theta_g}{\partial \eta_y} = 0 \text{ at } \eta_y = 0 && \frac{\partial \theta_g}{\partial \eta_y} = 0 \text{ at } \eta_y = \eta_{Ly} \end{aligned} \tag{5.4}$$

Solid phase exchanges energy with the gas phase by convection and radiation and that provides the boundary conditions for the solid at both ends of the porous matrix as:

$$\begin{aligned} &-\frac{\partial \theta_s}{\partial \eta_x} = P_5 (\theta_g - \theta_s) \text{ at } \eta_x = 0 && \frac{\partial \theta_s}{\partial \eta_x} = P_5 (\theta_g - \theta_s) \text{ at } \eta_x = 1 \\ &\frac{\partial \theta_s}{\partial \eta_y} = 0 \text{ at } \eta_y = 0 && \frac{\partial \theta_s}{\partial \eta_y} = 0 \text{ at } \eta_y = \eta_{Ly} \end{aligned} \tag{5.5}$$

Non-dimensional form of volumetric radiation term $\nabla \cdot \Psi_R$ can be presented as:

$$\nabla \cdot \Psi_R = \beta L_x (1-\omega) \left[4\pi \Phi (1+\theta_s)^4 - G^* \right] \tag{5.6}$$

where $\Phi = \dfrac{\sigma T_i^4}{\dot{Q} L_x}$ is the non-dimensional emissive power at the inlet $\eta_{x,i}$ and $G^* = \dfrac{G}{\dot{Q} L_x}$ is the non-dimensional incident radiation. The non-dimensional source term is given as:

$$S^*(\tau) = (1-\omega)\frac{\Phi(1+\theta)^4}{\pi} + \left(\frac{\omega}{4\pi}\right) G^* \tag{5.7}$$

A knowledge of the boundary intensity is required while marching from any of the corners. For a diffuse-gray boundary/wall with known temperature and emissivity, the boundary intensity can be computed as:

$$I_b^* = \varepsilon_b \frac{\Phi(1+\theta_b)^4}{\pi} + \frac{(1-\varepsilon_b)}{\pi} \sum_{k=1}^{M_\mu} \sum_{l=1}^{M_\lambda/2} I^{*,m}\left(\lambda_l^m, \mu_k^m\right) \sin\lambda_l^m \cos\lambda_l^m \sin\Delta\lambda_l^m \Delta\mu_k^m \tag{5.8}$$

Here $I^* = \dfrac{I}{\dot{Q} L_x}$ refers to the non-dimensional intensity.

Starting with guessed temperature fields for both gas and solid phases, Gauss-Seidel methods is employed to update the temperature fields by solving the energy equations simultaneously. After a few iterations, the radiative transfer equation is solved to compute the divergence of radiative heat flux. The modified value is then used in the energy equations for obtaining the new temperature fields. The iterative process continues till the desired convergence level is achieved.

5.3 Results and Discussions

Principal focus of the present study being the simultaneous estimation of two optical properties, gas temperature distribution can be treated as the known parameter using any possible means such as experimental observations, analytical expressions or numerical simulation. Present work employs numerical estimation of temperature profile following the mathematical model detailed above. Selection of number of grid points and number of grid points in the $4\pi-$spherical space of volumetric radiation is very important for ensuring the accuracy of simulations. A grid system of 300 × 20 (Fig. 5.1b) is adopted here for the solid portion, with 32 number of intensities. The width for the gas-phase domain being three times of solid, 900 × 20 grid points are selected. It is important to

establish the validity of the present grid system by comparing the steady-state temperature profiles, before employing the same for the optimization. Setting a large aspect ratio $r = \frac{L_y}{L_x} = 10$, present situation can be viewed to resemble a 1-D case. Corresponding gas and solid temperature profiles are compared with the numerical results of Tong and Sathe [122] setting $\beta = 1.0$ and a strong convective coupling signified by $P_2 = 500.0$. Values of other relevant parameters are listed in Table 5.1. High value of convective coupling ensures nearly-identical values of solid and gas temperature throughout the porous matrix. As can be seen from Fig. 5.2, satisfactory level of conformity is achieved, particularly around and downstream of the zone of heat generation, and hence the direct code can be utilized for optimization with confidence.

Table 5.1. Parameter values used for simulations.

Parameters	Values
P_1	0.01
P_3	2.5 x 10^{-4}
P_4	0.02
P_5	5
ω	0.5
ε	1.0
$\Phi_i = \Phi_e$	2.98x10^{-5}

In order to understand the relative influence of system parameters, parametric variation is attempted with major focus on P_2 and β, and concerned results are presented in Fig. 5.3. For weak convective coupling $(P_2 = 1.0)$, temperature profile for both the phases are shown with two different values of extinction coefficient. Significant difference exists between the two values at any particular location due to weak convective heat transfer. Direction of heat transfer in the zone upstream to heat generation $(0.45 < \eta_x \leq 0.55)$ is from solid to gas, whereas the same is from gas to solid thereafter. Gas temperature rapidly increases in the middle section due to the volumetric heat generation, while solid receives the heat only from the gas phase by weak convection. Solid medium allows heat transport to the upstream side by conduction, providing a consistent temperature gradient approaching the combustion zone. Radiation from solid on the upstream side also allows

preheating of the gas phase, thereby raising the gas temperature quite substantially before actual heat generation. Radiation can be eliminated by setting $\beta = 0.0$, as is shown in Fig. 5.3(a). Maximum temperature for the gas phase, as well as the gas temperature level downstream to the heat-generation zone, is much higher. Due to weak convective coupling $(P_2 = 1.0)$, solid is not receiving much energy in the heat-generation zone and downstream to that. Solid in the upstream zone is receiving heat only by conduction, resulting in lesser solid temperature and so minimal preheating of the gas phase. With stronger convective coupling $(P_2 = 500.0)$, however, there is hardly any distinction between temperatures of both the phases throughout the domain, irrespective of the value of β. The preheating is obviously present with higher value of β.

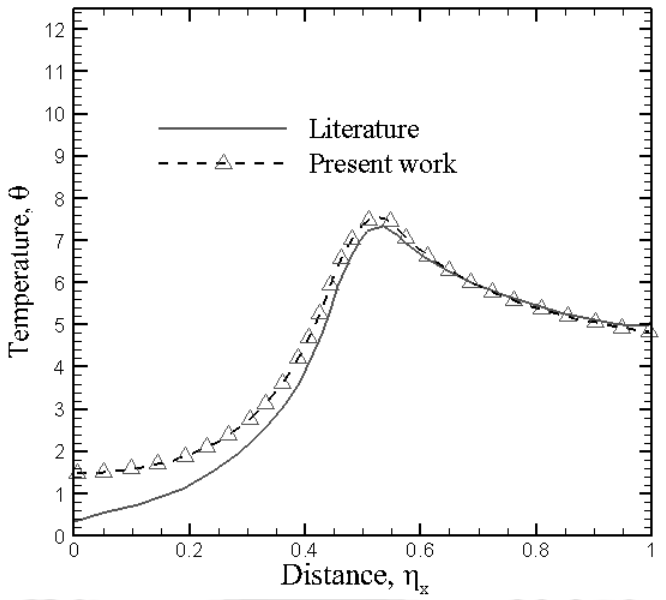

Figure 5.2: Validation of present computational model with the work of Tong and Sathe [114] for $P_2 = 500$ and $\beta = 1.0$.

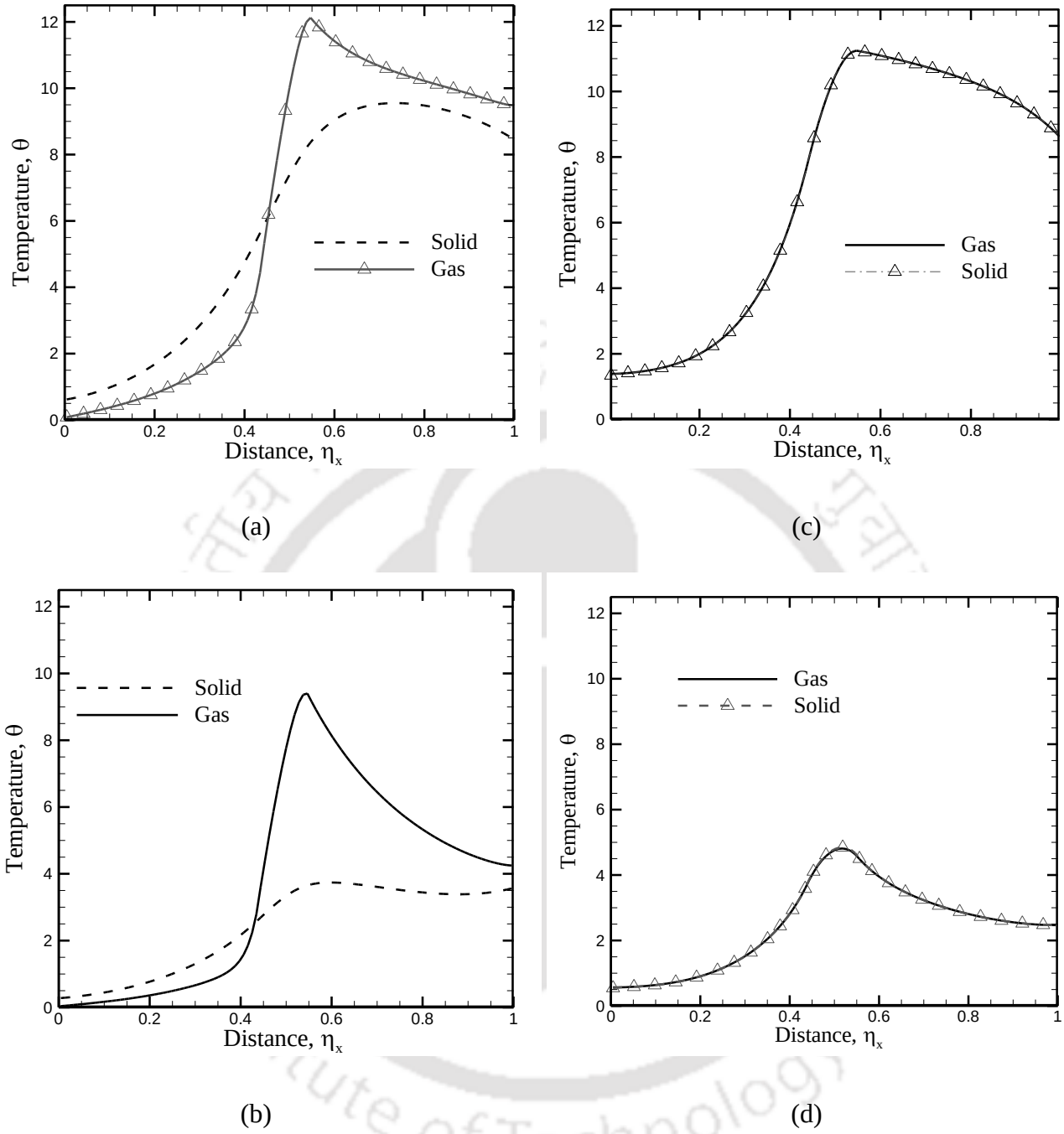

Figure 5.3: Distributions of gas and solid temperatures for (a) $\beta = 0.0, P_2 = 1.0$, (b) $\beta = 1000.0, P_2 = 1.0$, (c) $\beta = 1.0, P_2 = 500.0$ and (d) $\beta = 1000.0, P_2 = 500.0$.

The gas-phase energy equation comprises of convective heat transport, conduction and heat generation, while the solid-phase energy equation has conductive, convective and radiative contributions. Relative influence of each of these components is generally a good indicator of the mode of heat transport at any particular location of the domain.

Therefore the percentage contributions for each components in both gas and solid energy equations are shown in Fig. 5.4a and 5.4b respectively for strong convective coupling $(P_2 = 500)$ and intense radiation effects $(\beta = 1000)$. As can clearly be seen, energy received by the gas-phase due to heat generation is mostly balanced by convective heat exchange with solid. Conduction in gas is not of mush significance away from the combustion zone. Heat exchange curve for the gas-phase is positive on the upstream side, indicating higher temperature for the solid phase. Rapid influx of energy to the gas phase in combustion zone sharply increases the gas temperature and hence the heat exchange curve drops to the negative zone on the downstream side. The same is understandably reverse for the solid-phase. Large quantity of energy received by the solid in the heat generation zone is compensated by radiation transport towards the gas. Radiation is quite prominent on the downstream side as well, due to higher temperature values for the solid there. Entry region, despite being at the lowest temperature, receives very little radiation energy due to high optical thickness. Conduction in solid is also more pronounced compared to the gas phase owing to the much larger thermal conductivity of the solid. Conduction heat transfer is also more noticeable on the upstream side, allowing for preheating.

5.3.1 Two parameter Estimation

Scattering albedo and emissivity at the right-hand exit are selected as the target properties in the present work and inverse analysis is employed for their optimization. The objective function can be defined as the cumulative differences between the gas temperatures predicted by the direct and inverse codes at all node points along the x-centerline of the matrix. The mathematical form can be defined accordingly as:

$$J = \sum_{i=1}^{N} \left(\tilde{\theta}_{g,i} - \theta_{g,i} \right)^2 \tag{5.16}$$

N being the number of nodes along x-direction within the matrix. Genetic algorithm (GA) is used to minimize the objective function and concurrently converge towards both the selected variables.

For the purpose of simultaneous optimization of (ω, ε), exact values of these parameters are taken to be 0.5 and 0.9 respectively. Inverse analysis is performed with four different population sizes, namely, 10, 20, 30 and 40, and also with four different generations, namely, 10, 20, 30 and 40 for each population. Predicted values for both the parameters, corresponding percentage errors and magnitude of fitness function are reported for all the combinations in Table 5.2 and 5.3. Reasonably accurate estimation can be observed, particularly high larger values of the population size and number of generations. Temperature profiles for the gas phase with both direct method (FDM-FVM) and inverse method (FDM-FVM-GA) are compared in Fig. 5.5 for 40 generations and 40 number of population. Excellent degree of conformity can be clearly observed.

Proper choice of crossover probability and mutation probability are important factor in optimization. Variation of predicted values and corresponding errors with probabilities are summarized in Table 5.4 for 40 generations and 40 number of populations. Fig. 5.6 presents the variation of fitness function with the number of generations. A crossover probability value of 0.8 and mutation probability of 0.3 is identified to be sufficient from both computational time requirement and solution accuracy point of view. Effect of measurement error with varying number of generations and population size is presented in Fig. 5.7. Measurement error is considered to lie in the range of 0-5%. Excellent fitness value can be found even with small generation and population size for measurement error of 2% or less. Computational time requirement is another important

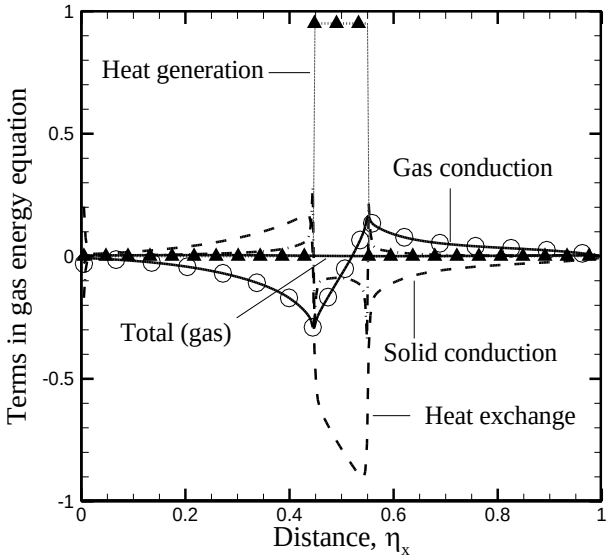

(a)

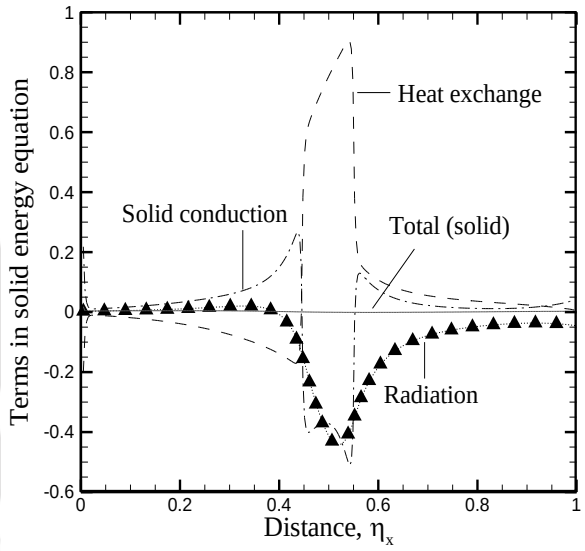

(b)

Figure 5.4: Comparison of different components in energy equations for $P_2 = 500$ and $\beta = 1000$ (a) gas energy equation and (b) solid energy equation

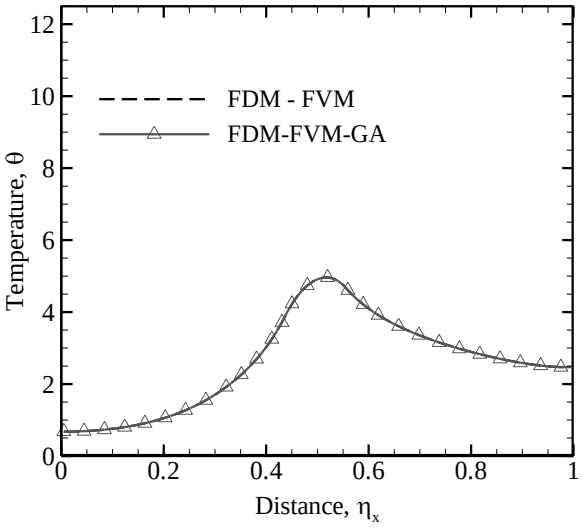

Figure 5.5: Comparison of non-dimensional gas or solid temperature from direct and inverse method

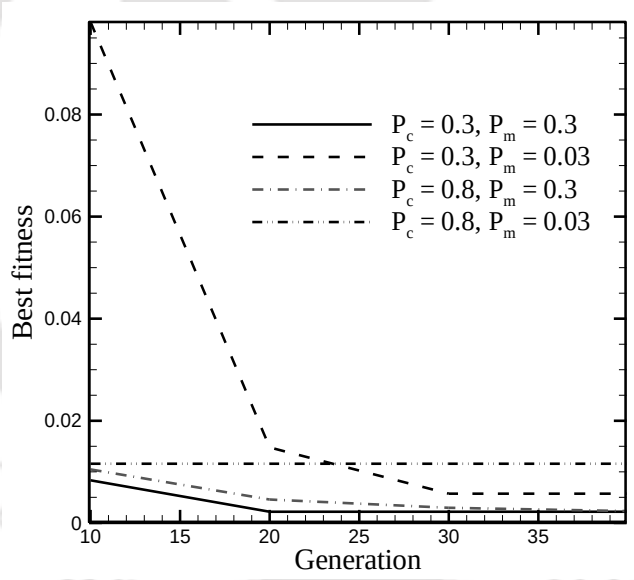

Figure 5.6: Effect of crossover probability and mutation probability on variations of best fitness with number of generations.

aspect in inverse estimation CPU time is expected to increase with both population size and number of generations. Their effect is found to be linear (Fig. 5.8). Measurement error is found to have a similar effect on CPU time. All the simulations here are performed on a computer with 2.1 GHz processor and 2 GB RAM. Quantitative values of CPU time may vary with change in processor, with the qualitative nature remaining the

same. As can be seen from Fig. 5.9, fitness function converges towards a satisfactory level after about 30 generations. Similarly a population size of 40 is found to be sufficient. Even better prediction can be achieved high higher level of generation and population size, but at the expense of large CPU time requirement.

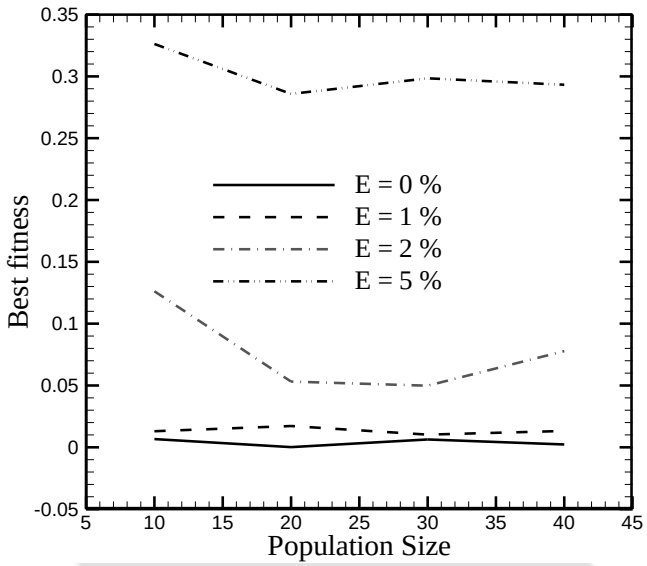

Figure 5.7 (a) : Effect of measurement error on variations of best fitness with population size.

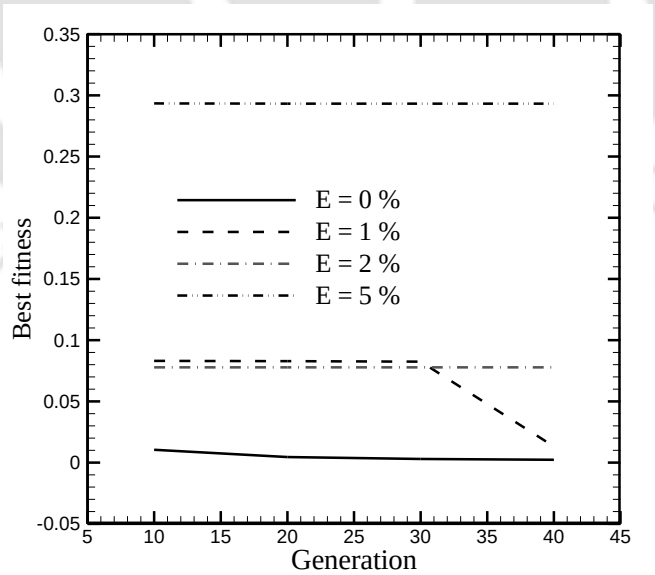

Figure 5.7 (b) : Effect of measurement error on variations of best fitness with number of generations.

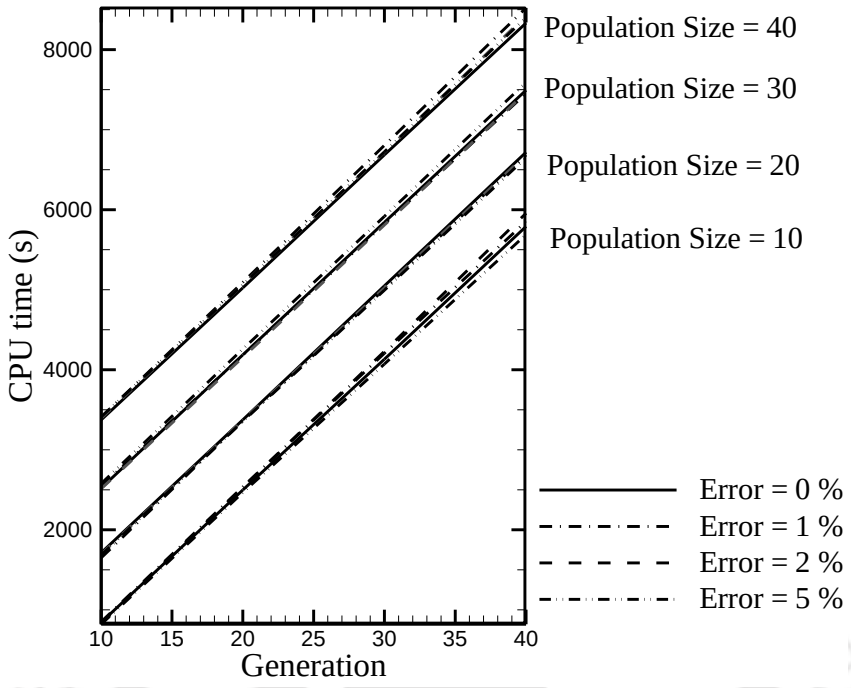

Figure 5.8: Effect of measurement error and population size on variations of CPU time (s) with number of generations.

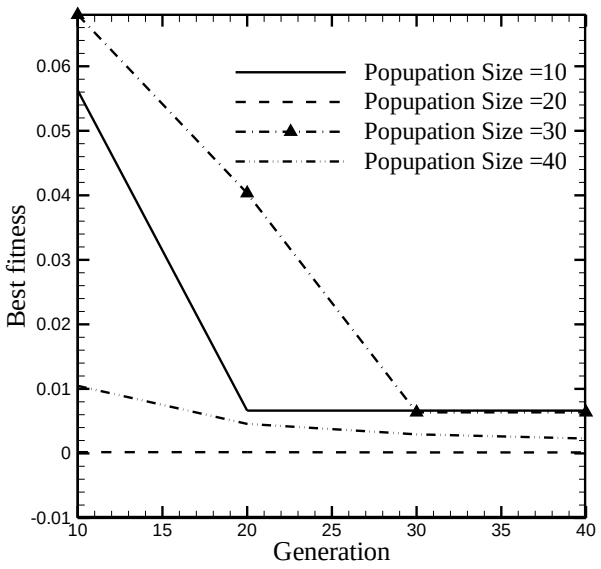

Figure 5.9: Effect of population size on variations of best fitness with number of generations.

Table 5.2. Estimated values of ε_e and ω for different population size and generations.

Generation	Population	Fitness	Time (s)	ω	ε_e	Error in estimation	
						ω	ε_e
10	10	0.056261	842.98	0.537	0.6788	7.4	-24.58
20	10	0.006639	2497.88	0.4865	0.9269	-2.69	2.99
30	10	0.006639	4131.56	0.4865	0.9269	-2.69	2.99
40	10	0.006639	5790.55	0.4865	0.9269	-2.69	2.99
10	20	0.000195	1712.53	0.4981	0.8972	-0.37	-0.31
20	20	0.000195	3374.28	0.4981	0.8972	-0.37	-0.31
30	20	0.000154	5048.42	0.4981	0.9003	-0.37	0.03
40	20	0.000154	6718.32	0.4981	0.9003	-0.37	0.03
10	30	0.067984	2521.33	0.5438	0.7191	8.77	-20.11
20	30	0.040331	4186.36	0.5125	0.7191	2.51	-20.11
30	30	0.006361	5842.89	0.5125	0.8749	2.51	-2.78
40	30	0.006361	7493.27	0.5125	0.8749	2.51	-2.78
10	40	0.01047	3373.4	0.5177	0.8401	3.53	-6.65
20	40	0.004573	5023.33	0.5083	0.8401	1.66	-6.65
30	40	0.002956	6685.34	0.5083	0.8561	1.66	-4.88
40	40	0.002306	8333.03	0.4986	0.8687	-0.28	-3.48

Table 5.3: Effect of population size and measurement error for exact value of $(\varepsilon_e,\ \omega) = (0.9,\ 0.5), P_c = 0.80$ and $P_m = 0.3$.

Generation	Population	Fitness	Time (s)	Error $\pm E$	ω	ε_e	Error in estimation	
							ω	ε_e
30	30	0.006361	5842.89	0	0.5125	0.8749	2.51	-2.78
30	30	0.010248	5822.95	1	0.5009	0.9004	0.18	0.04
30	30	0.049834	5808.93	2	0.5022	0.9004	0.44	0.05
30	30	0.300229	5917.33	5	0.5223	0.7955	4.46	-11.61
30	40	0.002956	6685.34	0	0.5083	0.8561	1.66	-4.88
30	40	0.082456	6803.97	1	0.547	0.7245	9.39	-19.5
30	40	0.0778	6717.71	2	0.5303	0.7973	6.07	-11.41
30	40	0.293231	6723.15	5	0.5172	0.8113	3.44	-9.85
40	30	0.006361	7493.27	0	0.5125	0.8749	2.51	-2.78
40	30	0.010248	7452.15	1	0.5009	0.9004	0.18	0.04
40	30	0.049834	7466.03	2	0.5022	0.9004	0.44	0.05
40	30	0.298433	7591.13	5	0.4999	0.7955	-0.01	-11.61
40	40	0.002306	8333.03	0	0.4986	0.8687	-0.28	-3.48
40	40	0.013208	8521.18	1	0.5057	0.9198	1.13	2.2
40	40	0.0778	8423.63	2	0.5303	0.7973	6.07	-11.41
40	40	0.293231	8401.61	5	0.5172	0.8113	3.44	-9.85

Table 5.4. Effect of crossover probability P_c and mutation probability P_m for exact value of $(\varepsilon_e,\ \omega) = (0.9,\ 0.5)$; number of generations = 40, population size = 40.

P_c	P_m	**Fitness**	**Time (s)**	ω	ε_e	**Error in estimation**	
						ω	ε_e
0.3	0.3	0.002185	8457.71	0.5088	0.8571	1.76	-4.76
0.3	0.03	0.005723	8186.95	0.4891	0.9558	-2.18	6.2
0.8	0.3	0.002306	8333.03	0.4986	0.8687	-0.28	-3.48
0.8	0.03	0.011588	8383.25	0.5181	0.847	3.62	-5.89

In the present numerical model, an accuracy of ±5%, is obtained in the simultaneous estimation of optical properties (ω,ε_e) of the porous matrix, for zero measurement error. However, an accuracy of ±3%, is obtained even for measurement error of up to ± 1 %, but only with higher population sizes i.e. 40. Even though it is expected that, CPU time will rise with the measurement error, but the CPU time is not following any particular trend. This behavior is due to the fact that, the best fitness for different measurement error is not the same. So, it is difficult to predict the trend of the CPU time requirement with variation in measurement error. Also it is important to note that, while doing any analysis with regard to CPU time requirement, the system should not be used for any other work. It is noticed that, accuracy of estimated parameters increases with the increase in number of generation and population size, but with the cost of rising CPU time. A sufficiently good accuracy is attained with 40 number of generations and 40 number of population size. If the measurement error in very less (i.e. < ± 1), 20 number of generations and 20 number of population size, also gives accuracy of within ± 1 %. Such wise selection saves computational cost.

5.3.2 Four Parameter Estimation

After successfully estimating two parameters, objective function is modified to estimate four parameters. Four different parameters, namely, the emissivity ε, the scattering albedo ω, the non-dimensional solid conduction P_4 and the non-dimensional convective heat transfer coefficient P_2, are selected for simultaneous optimization following inverse analysis. The first objective function is defined in terms of the gas phase temperature in the following form.

$$J_1 = \sum_{i=1}^{N_x}\sum_{j=1}^{N_y}\left(\tilde{\theta}_{g,i,j} - \theta_{g,i,j}\right)^2 \tag{5.9}$$

Similarly the second objective function is constructed using the solid phase temperature as:

$$J_2 = \sum_{i=1}^{N_x}\sum_{j=1}^{N_y}\left(\tilde{\theta}_{s,i,j} - \theta_{s,i,j}\right)^2 \tag{5.10}$$

The above tow definitions are combined to obtained a unified objective function encompassing the temperature for both the phases as:

$$J_3 = \frac{(J_1 + J_2)}{2} \tag{5.11}$$

Here $\tilde{\theta}_{g,i,j}$ and $\theta_{g,i,j}$ are the exact and unknown gas temperatures, respectively, whereas $\tilde{\theta}_{s,i,j}$ and $\theta_{s,i,j}$ are the analogous quantities for the solid phase respectively. The convective and radiative energy fluxes are combined to design another objective function as:

$$J_4 = \sum_{j=1}^{N_y}\left(\left(\tilde{\Psi}_{rad,j} - \Psi_{rad,j}\right)^2 + \left(\tilde{\Psi}_{conv,j} - \Psi_{conv,j}\right)^2\right) \tag{5.12}$$

where $\tilde{\Psi}_{rad,j}$ and $\Psi_{rad,j}$ are the exact and unknown radiative heat fluxes, respectively at the outer boundary $(\eta = 1)$ of the porous matrix, whereas $\tilde{\Psi}_{conv,j}$ and Ψ_{conv} are the equivalent convective heat fluxes respectively. Finally the objective functions J_3 and J_4 are united to design the final objective function J as :

$$J = \frac{(2 \times J_3) + (N_x \times J_4)}{N_x + 2} \tag{5.13}$$

In the inverse analysis, gas and solid temperature distributions, radiative heat flux and convective heat flux are estimated following FDM-FVM approach, which refers to the finite volume based solution of the energy equations and the adoption of finite volume method for the radiation component. Inverse analysis being computationally very expensive, judicial choice of optimization tool is an obligation. Two different techniques are compared in the present work, namely, the genetic algorithm (GA) and global search algorithm (GSA). Table 5.5 summarizes the observations with GA for different generations. It is very clear that the percentage error in each of the four variables are significantly high and the values of concerned fitness function are also not very suitable for practical use. Fitness prediction with both the techniques are compared in Fig. 5.10. GSA provides near-zero fitness for reasonably low CPU time and establishes itself as computationally more efficient than GA for all the studied cases. Therefore GSA is employed to minimize the objective function in the present work and results are shown in Table 5.6.

It is important to compare the predictions from the direct and inverse codes of the four dependent variables selected to frame the objective functions, which can also provide useful insight into the thermal characteristics of porous media heat transfer. Gas and solid temperature distribution along the centerline are presented in Fig. 5.11 for weak convective coupling $(P_2 = 10.0)$ and high extinction coefficient $(\beta = 100.0)$, with black boundary at $\eta_y = 0$ and $\eta_y = 1$. Spatial distribution of convective heat flux (Fig. 5.12) and radiative heat flux (Fig. 5.13) along the centerline are used in fabrication of objective function. Amicable agreement can be observed in the results predicted by both the codes.

Upstream to the heat generation zone, solid temperature is higher, as it received energy from the downstream side by both conduction and radiation. Gas has very low thermal conductivity and so can receive energy only by convection from the solid. Such heat addition to the gas results in substantial preheating of the gas phase, as it approaches the heat generation zone. Inside the combustion zone and downstream to that, however, the gas phase has higher temperature and can supply energy to the solid by convection. Large amount of energy added to the gas phase due to the simulated combustion in the central location is the reason for rapid rise in gas temperature in the middle of the matrix.

The accuracy of optimization is governed by the accuracy involved in the values of each of the four supplied dependent variable $\tilde{D}$. If E is the error associated in the measurement of dependent variable D_{measured}, then

$$D_{\text{measured}} = \tilde{D} + E \tag{5.14}$$

where $\tilde{D}$ refers to the exact dependent variables. Fig. 5.14 shows the variation in the objective function with percentage error in input variables, with several choices of the number of initial points in GSA. Magnitude of the fitness function rapidly increases with error in the supplied data. The number of initial point is found to have inconsequential effect on the same. Fig. 5.15 and Fig. 5.16 shows variation of CPU time and a product (CPU time times fitness) with the percentage error in the input variables. It is difficult to identify any general trend about the dependence of CPU time requirement on the initial number of points from Fig. 5.15. When the error is larger than 1%, all the plots seem to be quite random. The product of CPU time to fitness provides a better guide in this context (Fig. 5.16). As the error grows in the supplied data, choice of larger number of initial points seems more desirable. Both Fig. 6 and 7 together serve as useful tool for selecting the number of initial points, based on the error present in the dependent variables.

Table 5.5. Estimated values of $\omega, \varepsilon_e, P_4$ and P_2 for different generations in GA, for exact value of $(\omega, \varepsilon_e, P_4, P_2)$ = (0.5, 0.9, 0.02, 500).

Predicted values				**Generation**	**Population**	**Fitness**	**CPU time (s)**	**% Error in**			
ω	ε_e	P_4	P_2					ω	ε_e	P_4	P_2
0.5736	0.9985	0.0164	479.19	50	50	0.7672	26005	14.7	10.9	-17.8	-4.2
0.5740	0.9999	0.0166	479.25	100	50	0.7663	36703	14.8	11.1	-16.9	-4.1
0.5753	0.9999	0.0173	479.26	150	50	0.7657	47287	15.1	11.1	-13.6	-4.1
0.5753	1.0	0.0172	479.35	200	50	0.7652	57923	15.1	11.1	-13.6	-4.1

Table 5.6. Estimated values of $\omega, \varepsilon_e, P_4$ and P_2 for different number of starting points and error in input, for exact value of $(\omega, \varepsilon_e, P_4, P_2)$ = (0.5, 0.9, 0.02, 10).

Predicted values of				SP	Fitness	CPU time (s)	Input error	% Error in			
ω	ε_e	P_4	P_2					ω	ε_e	P_4	P_2
0.5	0.8595	0.02	9.9996	50	0.00007	82223	0.0	0	-4.5	0	0
	0.8608	0.02	9.9996	60		73104		0	-4.4	0	0
	0.8595	0.02	9.9996	70		98702		0	-4.5	0	0
	0.8594	0.02	9.9996	80		101040		0	-4.5	0	0
0.4869	1	0.0191	10.2875	50	0.07515	40666	1	-2.6	11.1	-4.5	2.9
	1	0.0191	10.2873	60		26138		-2.6	11.1	-4.5	2.9
	1	0.0191	10.2875	70		36326		-2.6	11.1	-4.5	2.9
	1	0.0191	10.2872	80		40063		-2.6	11.1	-4.5	2.9
0.5003	0.1233	0.0198	10.0619	50	0.28640	67912	2	0.1	-86.3	-1.0	0.6
	1	0.0198	10.0761	60	0.28622	64308		0.1	11.1	-1.1	0.8
	1	0.0198	10.0763	70	0.28622	24897		0.1	11.1	-1.1	0.8
	1	0.0198	10.0763	80	0.28622	39703		0.1	11.1	-1.1	0.8
0.4814	1	0.0179	10.8819	50	0.62217	61678	5	-3.7	11.1	-10.6	8.8
		0.0179	10.8816	60		102685		-3.7	11.1	-10.6	8.8
		0.0179	10.8817	70		40706		-3.7	11.1	-10.6	8.8
		0.0179	10.8811	80		27656		-3.7	11.1	-10.6	8.8

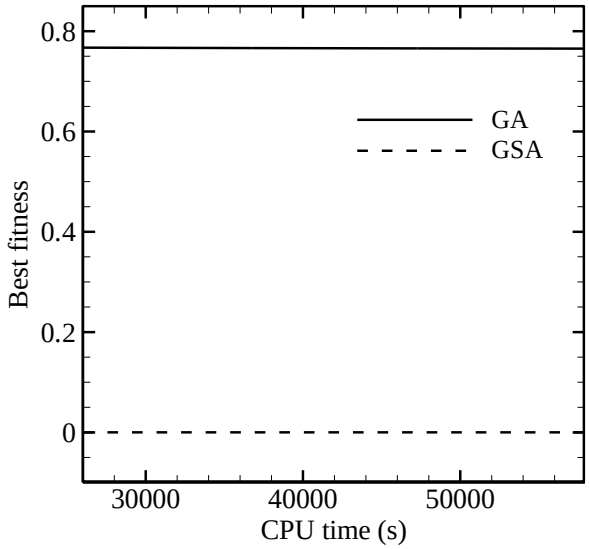

Figure 5.10: Comparison of best fitness for GA (population size = 50)and GSA (number of starting points = 50) with time

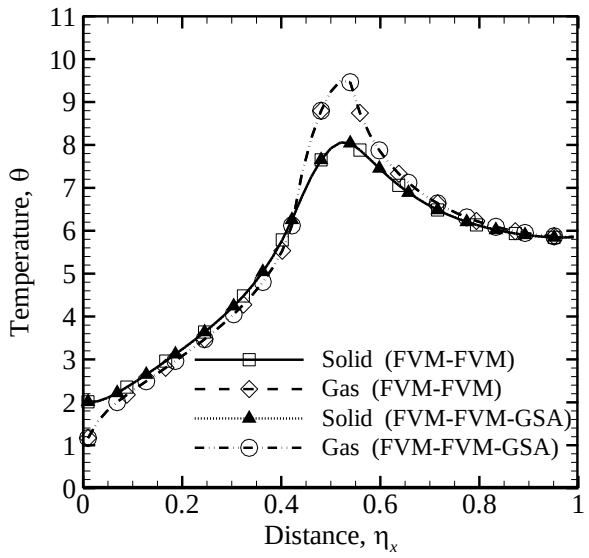

Figure 5.11: Comparison of non-dimensional gas and solid temperature from direct and inverse method.

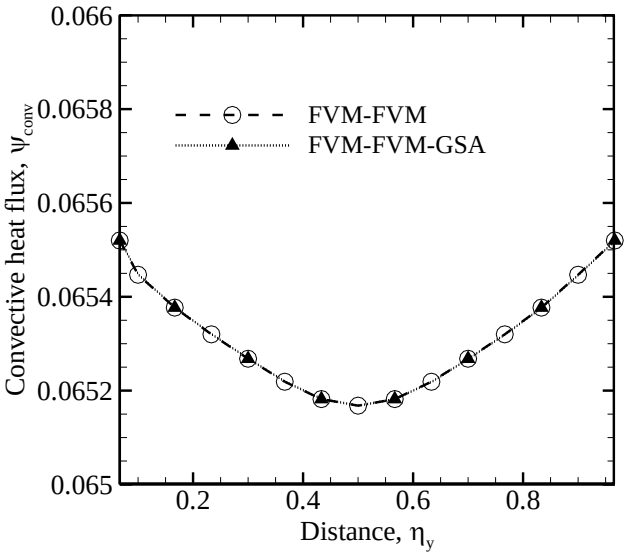

Figure 5.12: Comparison of non-dimensional convective heat flux, at the exit of porous matrix, from direct and inverse method.

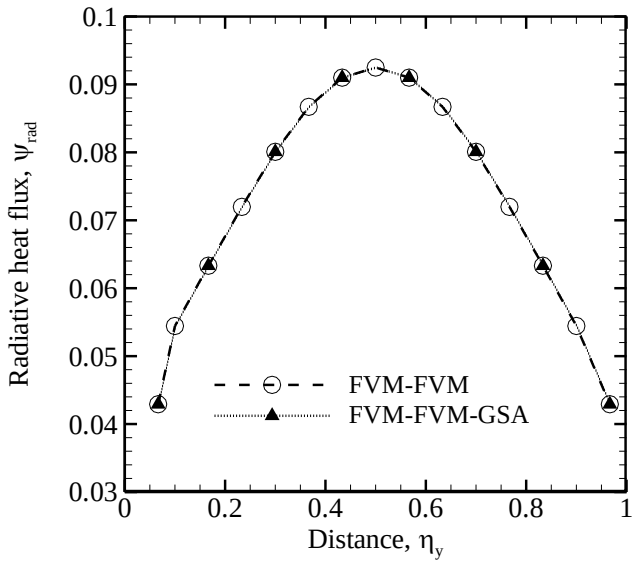

Figure 5.13: Comparison of non-dimensional radiative heat flux, at the exit of porous matrix, from direct and inverse method

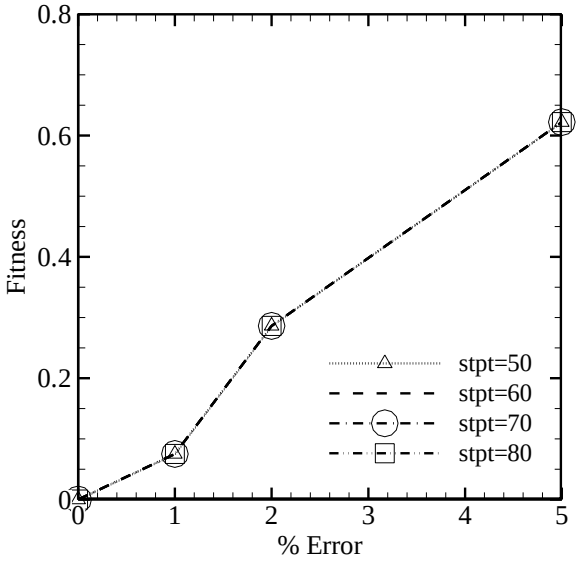

Figure 5.14: Effect of number of starting points on variations of best fitness with error in input.

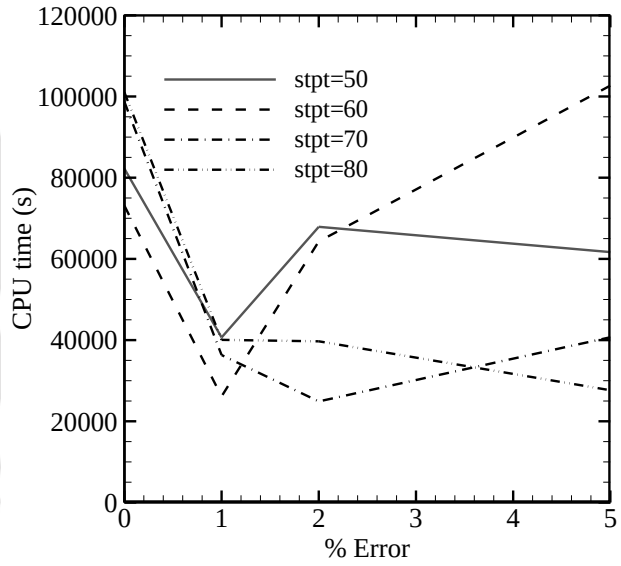

Figure 5.15: Effect of number of starting points on variations of CPU time (s) with error in input.

Magnitude of the fitness function is generally quite invariant of the number of starting points and is dominated by the error percentage (Fig. 5.17). For error less than 1%, magnitude of fitness is found to be very practicable. Fig. 5.18 and 5.19 shows variation of

CPU time and a product (CPU time times fitness) respectively with number of starting points for different percentage error in inputs.

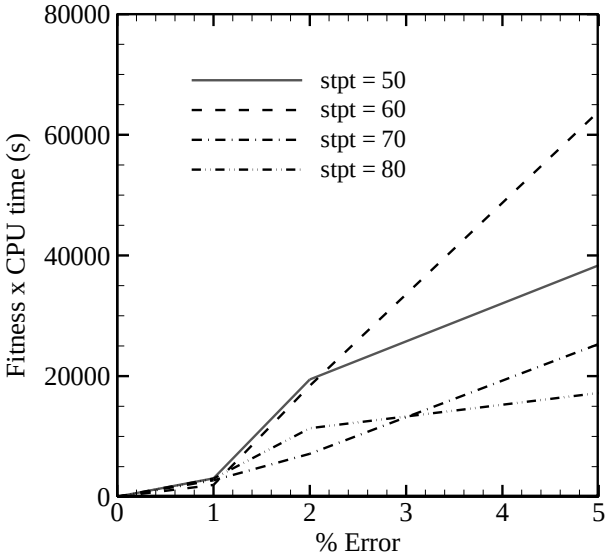

Figure 5.16: Effect of number of starting points on variations of (best fitness × CPU time) with error in input.

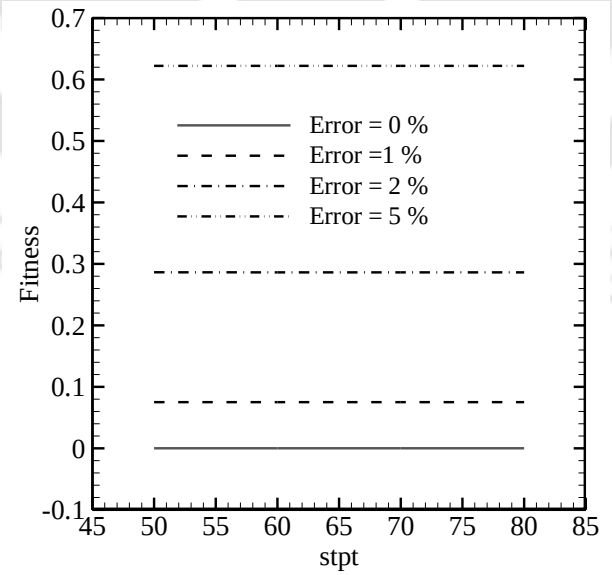

Figure 5.17: Effect of number of error in inputs on variations of best fitness with number of starting points (stpt).

Even though no clear trend is observed in Fig. 5.18, Fig. 5.19 clearly shows that cost in terms of loss of accuracy and CPU time occur with the rise in error in inputs. All runs were taken on 2.1 GHz processor with 2 GB RAM.

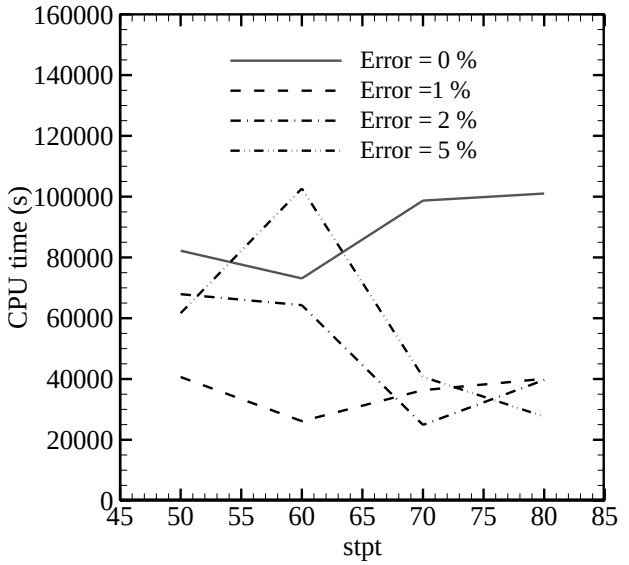

Figure 5.18: Effect of number of error in inputs on variations of CPU time (s) with number of starting points (stpt).

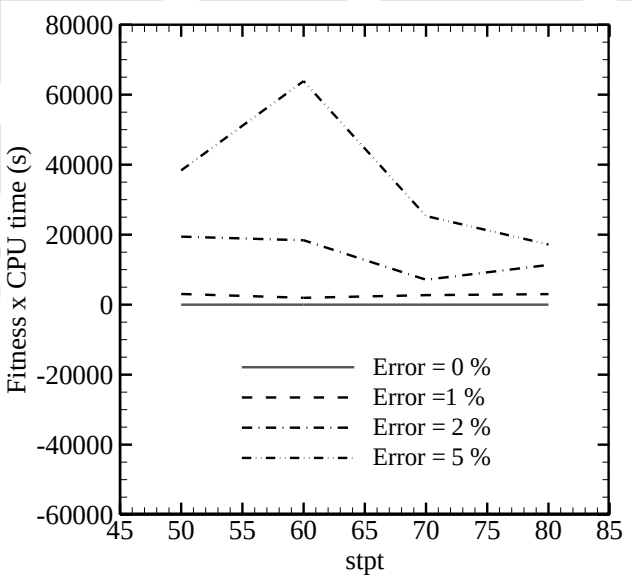

Figure 5.19: Effect of number of error in inputs on variations of (best fitness × CPU time) with number of starting points (stpt).

5.4 Summary

A numerical model is developed in the present study to understand the thermal characteristics of a 2-D rectangular porous medium and simultaneously optimize two optical properties for performance improvement. The porous structure is modeled as a 2-D combined-mode conduction-radiation problem, with combustion simulated as a central zone of heat generation. Non-dimensional forms of energy equations for both the solid and gas phases are developed, where they are convectively coupled by a heat exchange term. Only the solid phase is considered to be radiatively participating. Governing equations are concurrently solved following FDM, while employing FVM for evaluating the volumetric radiation. Computational results from the direct code is successfully compared with existing data from literature. Two separate studies are done: 1) Estimation of two parameters using the GA, and 2) Estimation of four parameters using the GA, and the GSA.

In the two parameter estimation, numerically estimated gas temperature profile is used to formulate the objective function in the inverse optimization problem, with scattering albedo and exit emissivity as the selected parameters, and GA is identified as the tool for minimizing the objective function. The inverse code also exhibits excellent capability of re-producing the gas temperature profile with reasonable values of number of generations and population size. It is possible to predict both the designated variables (ω, ε) within 0.5% accuracy at reasonable computational cost. However, prediction accuracy sharply increase with larger population size and higher number of generations, with proportionally linear increase in CPU time requirement. Crossover probability of 0.8 and mutation probability of 0.3 is found to be sufficient from both CPU time and solution accuracy point of view. For higher value of measurement error, drastic reduction in accuracy and rapid increase in computation time are observed.

In the four parameter estimation, gas and solid temperature distribution throughout the porous structure and the radiative and convective heat flux distributions at the exit plane of the matrix are selected as the dependent variables for the inverse problem. Four properties are simultaneously estimated, namely, emissivity ε_e, scattering albedo ω,

non-dimensional solid conduction P_4 and dimensionless convective heat transfer coefficient P_2. GA and GSA are attempted with as the optimization tool, with GSA demonstrating substantially better performance, both in terms of solution accuracy and CPU time requirement. Effect of the selected number of starting points in the GSA algorithm and percentage error present in the magnitudes of dependent variables are studied. With less than 2% error margin in the input data, good prediction accuracy is achieved. CPU time depends strongly on both the number of starting points and error percentage. Increase in error, affects the solution quite significantly and it is important to ensure the correctness of the supplied data for better optimization performance.

Chapter 6

2D-AXISYMMETRIC POROUS MEDIUM WITH COMBUSTION

6.1 Introduction

In the previous Chapters, different models of PRB were developed. These progress leads to development of very realistic model in the present Chapter. This Chapter deals with a two stage 2D-axisummetric model of PRB. The porosity of the upstream and downstream porous matrix are low and high, respectively. The low porosity upstream section acts as preheater and flame arrester. The other properties of the two porous matrices such as extinction coefficient and conductivities etc., are taken by using correlations available in the literature.

Performance of a PRB is very sensitive to its thermo physical, optical, and geometric properties such as thermal conductivity, scattering albedo, and porosity etc. Knowledge of these important parameters is very necessary for design of a PRB, and inverse analysis is an important engineering tool for the estimation of parameters. In the inverse analysis, an optimization algorithm is employed to minimize the objective function. The objective function to be fed to the optimization algorithm, is constructed using the known value of dependent variable like temperature distribution, heat flux etc. The dependent variable can be obtained by any means like experimentally measured, numerically computed or by analytic solution.

Two separate energy equations for the gas and the solid phase are considered to take care of nonlocal thermal equilibrium between the two phases. The two energy equations are convectively coupled. Methane is taken as fuel and combustion of methane is modelled through single step global mechanism. Gas phase is radiatively transparent as compared to solid. Solid is absorbs, emits and scatters thermal radiation. The radiative source term

appears only in the solid phase energy equation. The radiative source term required in the solid phase energy equation is computed using the finite volume method (FVM). After numerically solving all the governing equations under the required boundary conditions, temperature distribution is computed.

In the inverse analysis application, different test cases are compared like 1) Using different optimization techniques such as GA, GSA Pattern Search Algorithm (PSA), 2) Using experimental data, and numerically computed data as known dependent variables to construct the objective function.

PSA is very promising as an optimization technique especially when the direct problem also takes a lot of time to converge. PSA outperforms GA and GSA in terms of computation time without compromising on accuracy. Two parameters namely equivalence ratio and downstream pore diameter are estimated simultaneously.

6.2 Formulation

Schematic view of a two-stage 2D axisymmetric PRB is shown in Fig. 6.1. The upstream section of the porous matrix is of lower porosity, in comparison to the downstream section, and acts as preheater and flame arrester. Accordingly a two-stage PRB helps stabilizing the flame between the two porous layers. Methane-air mixture of specified equivalence ratio is allowed to enter the PRB from the left boundary and combustion takes place between the layers. A single-step chemistry is used to model the chemical reaction between fuel and oxidizer. Assuming atmospheric air to consist only of oxygen and nitrogen, and considering every mole of oxygen to be accompanied by 3.76 moles of nitrogen, the equation for stoichiometric reaction is given as:

$$CH_4 + 2O_2 + 2(3.76)N_2 \Rightarrow CO_2 + 2H_2O + 2(3.76)N_2 \qquad (6.1)$$

The reaction rate constant for the above equation is $k_c = 1.8\times10^8 \exp(\frac{-125600}{RT_g})[CH_4]$ mol/m^{3}s and equivalence ratio is taken to be 0.65. Hence the only species present inside the simulation domain are CH_4, O_2, N_2, CO_2 and H_2O.

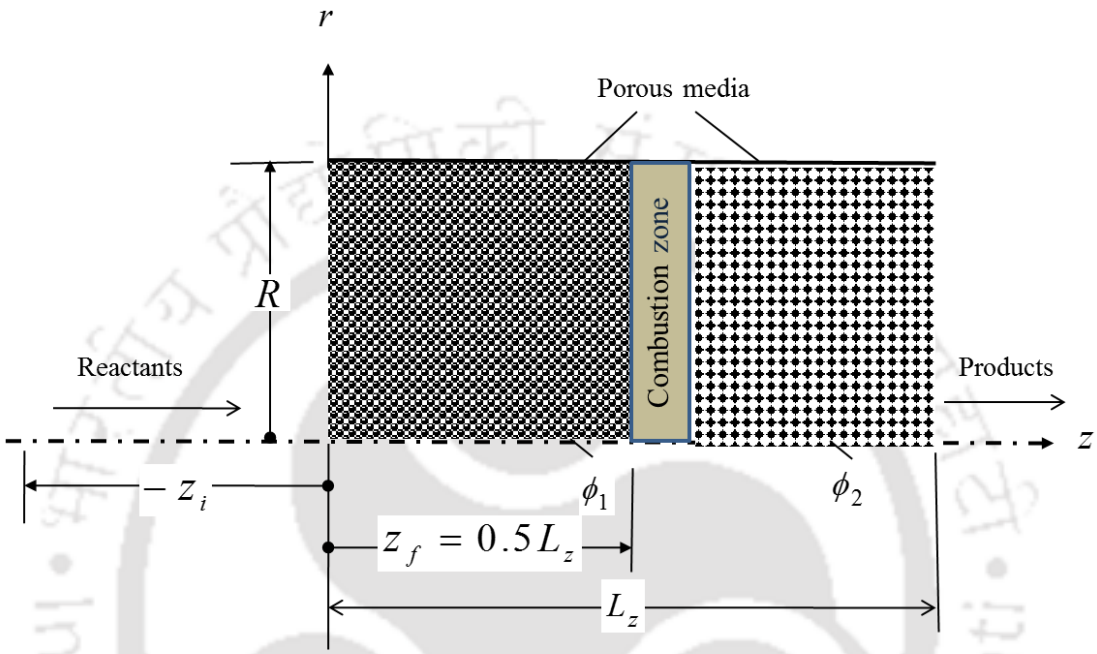

Figure 6.1. Schematic of the two layer 2D-axisymmetric porous matrix.

The gas flow is assumed to be isobaric at atmospheric condition throughout the burner and transparent to radiative energy exchange. It can thermally interact with the solid phase in convective mode. Only the solid phase is considered to participate in radiative heat transport, as it can absorb, emit and scatter radiation. The resultant set of conservation equations are the followings.

Continuity equation:

$$\vec{\nabla}.(\varphi\rho\,\vec{u}) = 0 \tag{6.2}$$

Gas phase energy equation:

$$\varphi\rho_g C_g \vec{u}\frac{\partial T_g}{\partial z} + (1-\varphi)Ah\left(T_g - T_s\right) = -\varphi\sum_{m=1}^{N}\dot{\omega}_m h_m W_m + \varphi k_g\left(\frac{\partial^2 T_g}{\partial r^2} + \frac{1}{r}\frac{\partial T_g}{\partial r} + \frac{\partial^2 T_g}{\partial z^2}\right) \tag{6.3}$$

Solid phase energy equation:

$$(1-\varphi)Ah\left(T_g - T_s\right) + (1-\varphi)k_s\left(\frac{\partial^2 T_s}{\partial r^2} + \frac{1}{r}\frac{\partial T_s}{\partial r} + \frac{\partial^2 T_s}{\partial z^2}\right) - \nabla . q_R = 0 \tag{6.4}$$

Species conservation equation:

$$\vec{\nabla}.(\varphi\rho\,\vec{u}\,y_m) = \vec{\nabla}.\left(\varphi\overrightarrow{V_m}\,\vec{\nabla}.y_m\right) + \varphi\dot{\omega}_m W_m \tag{6.5}$$

Radiative transport equation (RTE):

$$\begin{aligned}&\frac{1}{r}\frac{\partial}{\partial r}[\lambda\, \mathrm{rI}(\vec{\mathrm{r}},\vec{\mathrm{s}})] + \frac{1}{r}\frac{\partial}{\partial \varphi_0}[\eta\, \mathrm{I}(\vec{\mathrm{r}},\vec{\mathrm{s}})] + \frac{\partial}{\partial \mathrm{z}}[\xi\, \mathrm{I}(\vec{\mathrm{r}},\vec{\mathrm{s}})] - \frac{1}{r}\frac{\partial}{\partial \phi}[\eta\, \mathrm{I}(\vec{\mathrm{r}},\vec{\mathrm{s}})] \\ &= -\beta(\vec{\mathrm{r}})\,\mathrm{I}(\vec{\mathrm{r}},\vec{\mathrm{s}}) + \kappa_a(\vec{\mathrm{r}})\,\mathrm{I}_b(\vec{\mathrm{r}}) + \frac{\sigma_s(\vec{\mathrm{r}})}{4\pi}\int_{\Omega'=4\pi} \mathrm{I}(\vec{\mathrm{r}},\vec{\mathrm{s}}')\,d\Omega'\end{aligned} \tag{6.6}$$

Equation of state:

$$\rho = \frac{\bar{W}\,p}{RT_g} \tag{6.7}$$

where $\bar{W}$ is the mixture-averaged molecular weight and is defined as:

$$\bar{W} = \sum_{m=1}^{N} x_m W_m \tag{6.8}$$

The thermal boundary conditions imposed on the gas phase are,

$$\begin{aligned} &T_g = 300\ K && \text{at } z = -z_i && \frac{\partial T_g}{\partial z} = 0 && \text{at } z = L_z \\ &\frac{\partial T_g}{\partial r} = 0 && \text{at } r = 0 && \frac{\partial T_g}{\partial r} = 0 && \text{at } r = R_P \end{aligned} \tag{6.9}$$

Similarly the boundary conditions for solid phase energy equations are,

$$\begin{aligned} &-k_s\frac{\partial T_s}{\partial z} = hA\left(T_g - T_s\right) && \text{at } z = 0 && k_s\frac{\partial T_s}{\partial z} = hA\left(T_g - T_s\right) && \text{at } z = L_z \\ &\frac{\partial T_s}{\partial r} = 0 && \text{at } r = 0 && \frac{\partial T_s}{\partial r} = 0 && \text{at } r = R_P \end{aligned} \tag{6.10}$$

The boundary conditions for the conservation of the kth species are,

$$Y_m = Y_{m,i} \quad \text{at } z = -z_i \qquad \frac{\partial Y_m}{\partial z} = 0 \quad \text{at } z = L_z$$
$$\frac{\partial Y_m}{\partial r} = 0 \quad \text{at } r = 0 \qquad \frac{\partial Y_m}{\partial r} = 0 \quad \text{at } r = R_P \tag{6.11}$$

A knowledge of boundary intensity is essential for marching from one of the corners and the same for a diffuse-gray boundary/wall with known temperature and emissivity can be computed as:

$$I_W(\mathrm{r}_W, \vec{s}) = \varepsilon_w I_b(\mathrm{r}_W) + \frac{1-\varepsilon_w}{\pi} \int_{\vec{n}_W \bullet \vec{s}' < 0} I(\mathrm{r}_W, \vec{s}') \left| \vec{\eta} \bullet \vec{s}' \right| \mathrm{d}\Omega' \text{ for } \vec{\eta} \bullet \vec{s} > 0 \tag{6.12}$$

The governing equations (Eq. 6.2-6.5) are solved employing the boundary conditions mentioned above. The radiative information computed by solving the RTE is used in the solid phase energy equation. Parameter values used for simulation are summarized in Table 6.1. Several transport and radiative properties are required to be calculated as a part of the simulation procedure. The thermal conductivity of solid is given as a function of pore diameter as [123]:

$$k_s(d_p) = 0.188 - 17.5\, d_p \tag{6.13}$$

The extinction coefficient of porous matrix is [123]:

$$\beta(d_p) = \frac{0.0044}{d_p}(1 - \varphi) \tag{6.14}$$

The correlation for volumetric heat transfer coefficient between solid and gas is given as [124]:

$$Nu = \frac{Ah\, {d_p}^2}{k_g} = 0.819 \left[1 - 7.33 \left(\frac{d_p}{L} \right) Re^{0.36\left\{1+15.5\left(d_p/L\right)\right\}} \right] \tag{6.15}$$

Starting with guessed temperature fields for both gas and solid phases, Gauss-Seidel methods is employed to update the temperature and species concentration fields by simultaneously solving the conservation equations. After a few iterations, the radiative transfer equation is solved to compute the divergence of radiative heat flux. The modified value is then used in the energy equations for obtaining the new temperature fields. The iterative process continues till each of the following convergence criteria is satisfied.

1) Fractional change in $\frac{\partial T_g}{\partial z}(\text{at z} = 0, 0 \le \text{r} \le \text{R})$ in consecutive iterations is less than 10^{-6}
2) Fractional change in T_g $(\text{at z} = 0, 0 \le \text{r} \le \text{R})$ at in consecutive iterations is less than 10^{-6}
3) An overall energy balance of less than 0.001 percent is achieved

Selection of the adopted grid system plays a vital role in any numerical simulation. Present problem is solved with 1200×17 grid points for the solid domain ($0 \le z \le L_z$ and $0 \le r \le R$) and 224 $(\text{N}_\theta \times \text{N}_\alpha = 16 \times 14)$ number of intensities. 1500 grid points are chosen in the *z*-direction for solving the gas phase energy, while maintaining the number of grid points in the *r*-direction as identical to the solid phase. A fine grid of 900 grid points are taken in the combustion region to take care of high gradients of the temperature field. Increase in the number of grid points in either direction is found to have minimal effect on the results.

6.3 Results and Discussions

The present study focuses on understanding the heat transfer characteristics of porous radiant burner and estimation of parameters. Direct part of the problem is formulated as solving the conservation equations, with the specified boundary conditions. During estimation of parameters, inverse analysis is employed with experimentally available temperature profile inside the PRB as input and some of the most important design parameters, including scattering albedo, equivalence ratio and pore diameter, are estimated. Each of these parameters play a vital role is deciding the temperature profile inside the porous matrix.

Fig (6.2) shows the validation of the radiation part of the present model with the exact solutions, for the problem of a finite cylindrical enclose containing absorption coefficient. The enclosure with $r = 1\text{m}$ and $z = 2\text{m}$ is cold ($T_w = 0\text{K}$) and black ($\varepsilon_W = 1$), and the enclosed medium is hot as $T_g = T_{ref}$ and has three different absorption coefficients of $\kappa_a = 0.1, 1.0,$ and $5.0\,\text{m}^{-1}$. In this example, the exact intensity at any location within the

enclose is given by the summation of all the intensities from the enclosure wall as well as local emission of the medium such as

$$I(s) = I_{bW} e^{-\kappa_a s} + I_b (1 - e^{-\kappa_a s}) \tag{6.16}$$

where I_b is the blackbody intensity of the homogeneous medium, and s is the path length. The exact wall heat flux can be obtained by numerically integrating $I(s)(\vec{s} \bullet \vec{n}_W)$ over all incident solid angles via Gaussian quadrature numerical integration. For the validation of radiation modelling part, the grid structure used is $(N_r \times N_z = 17 \times 33)$ and $(N_\theta \times N_\alpha = 16 \times 14)$.

Table 6.1. Parameters used for the numerical model.

Property	**Upstream**	**Downstream**
Pore density	25.6 ppc	3.9 ppc
Pore diameter, d	0.029 cm	0.152 cm
Porosity, ϕ	0.835	0.87
Scattering albedo, ω	0.8	0.8
Length of porous matrix	3.5 cm	2.55 cm

Once the radiation part is validated, the grid structure is modified to have more grids in the z-direction. The direct problem is validated against experimental results of Mathis and Ellzey [125], and shown in Fig. 6.3. In their experiment, the burner consisted of two sections of porous ceramic and the flame was stabilized at the interface of the two porous

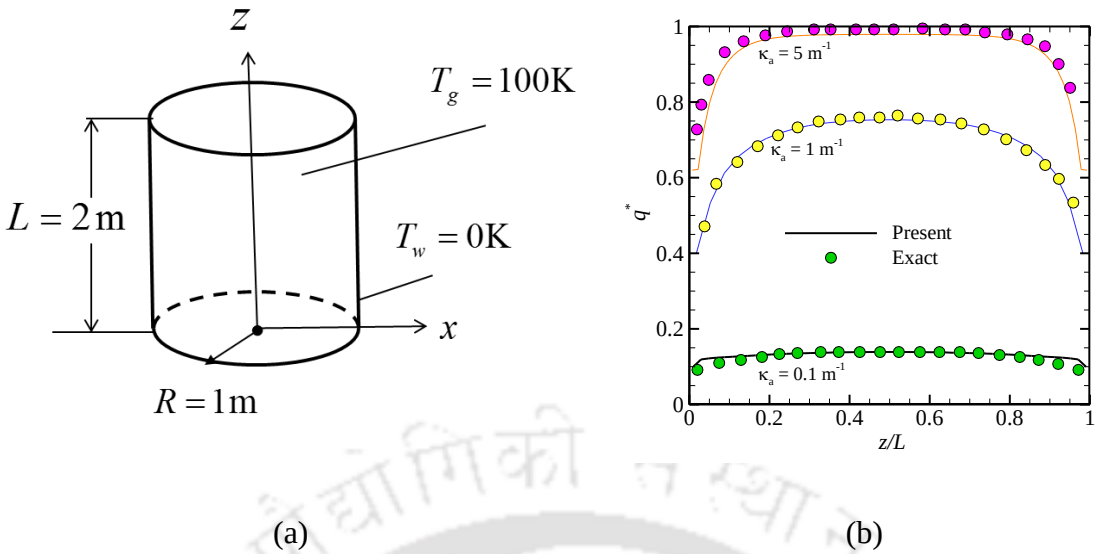

(a) (b)

Figure 6.2: Validation of radiation part of the present computational model with the analytical solution. (a) Schematic of radiation in axisymmetric cylinder (b) Comparison of non dimensional heat flux distribution on the side wall for three different absorption coefficient for the absorption and emitting medium. The grid system employed for validation is $(N_r \times N_z) = (17 \times 33)$ and $(N_\theta \times N_\alpha) = (16 \times 14)$.

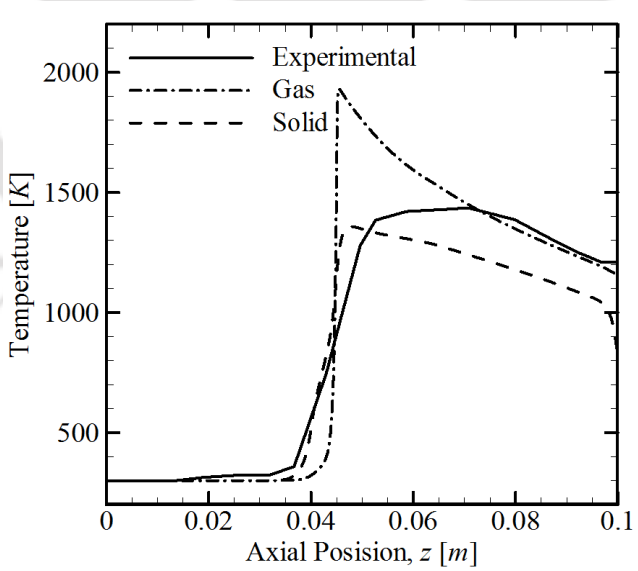

Figure 6.3: Validation of present computational model with the experimental results of Mathis and Ellzey [125] for u=0.45 m/s.

sections. Separate values of solid and gas temperatures are not available, as it is extremely difficult to differentiate between them in a real-life situation. Rather the axial profile of average temperature was reported. As can be seen from Fig. 6.3, the gas and solid temperature profiles clearly covers the experimental temperature distribution of the PRB. The numerical temperature distribution shown in the Fig. 6.3 corresponds to the central axial location ($0 \le z \le L_z$ and $r = 0$). The numerical results here corresponds to the gas velocity of 0.45 m/s, as in the concerned experiment.

Different components of heat flux are separately recognized in Fig. 6.4. Role of both the gas and solid conduction are found to be rather negligible. Since the gas temperature rises suddenly in the combustion zone and remains high in the downstream region, the gas conductive heat transfer takes place towards upstream cooler gas, thus leading to a downward peak of gas conduction. Hence the convective and radiative components can be identified as the most vital ones for the performance of PRB. Effect of gas velocity on the temperature profiles of the gas and the solid phase are shown in Fig. 6.5. The temperature profiles of both the phases rises to higher temperature as expected due to higher rate of firing and hence higher rate of heat generation due to combustion. Fig. 6.6 shows the effect of gas velocity on the gas and the solid phase exit temperature along the radial direction. Temperature variation for either of the phases along the radial direction is negligible. But temperature level changes quite significantly with increase in the velocity of the fuel-air mixture, emphasizing the enhanced role of convection. Fig.s 6.7-6.9 shows the effect of aspect ratio on the gas and the solid temperature along the axial direction $(r = 0, 0 \le z \le L_z)$ and the radial direction $(0 \le r \le R, L_z = 1.0)$. Due to change in the aspect ratio, the variation of temperature profiles of the gas- and the solid phase along the axial direction is very minute. The radial temperature distribution of the gas and the solid phase is very sensitive to the aspect ratio. With the increase in the aspect ratio, the variation in the temperature profiles of both the phases, along the radial direction increases. Fig. 6.10 and 6.11 shows the effect of circumference emissivity on the gas and the solid temperature distribution along the axial and the radial directions, respectively. Increase in exit emissivity clearly leads to higher temperature levels inside the PRB.

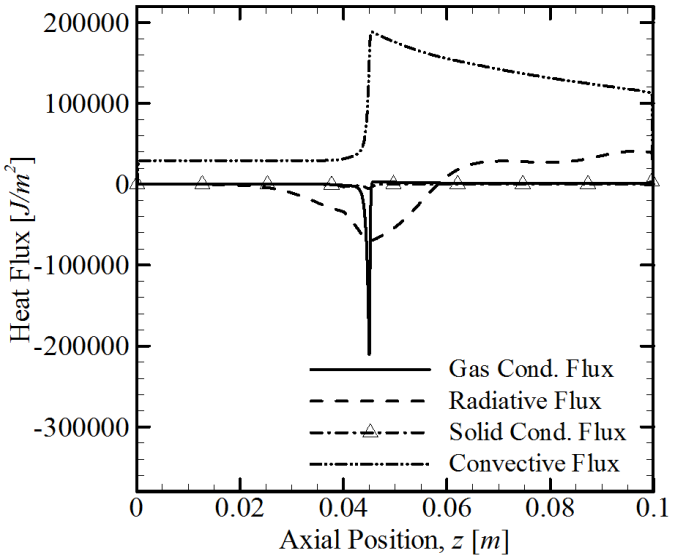

Figure 6.4: Component of different heat fluxes along the axial direction $(\mathrm{r}=0, 0 \le z \le L_z)$.

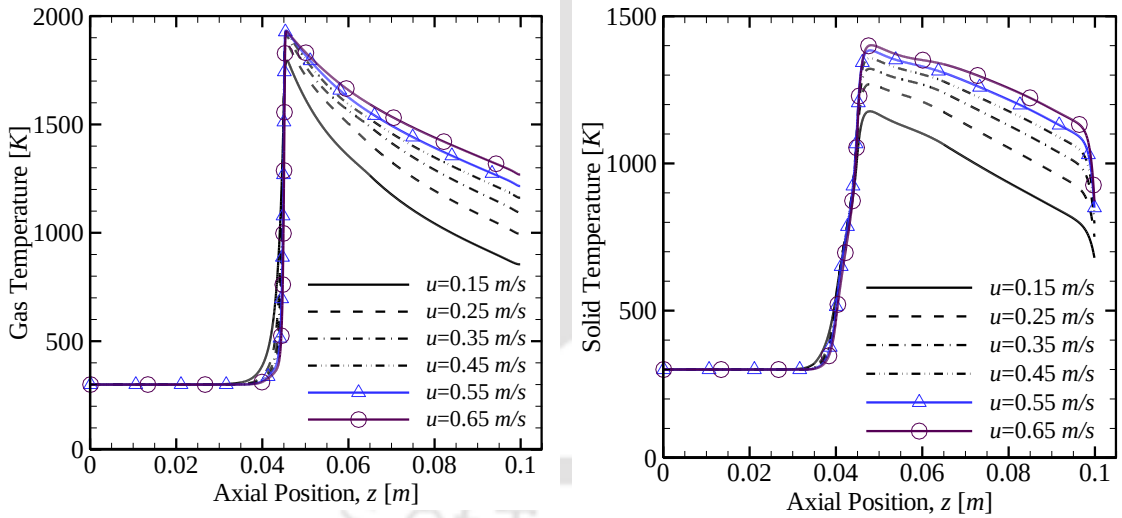

(a) (b)

Figure 6.5: Effect of air velocity on (a) the gas and (b) the solid temperature distribution along the axial direction $(\mathrm{r}=0, 0 \le z \le L_z)$.

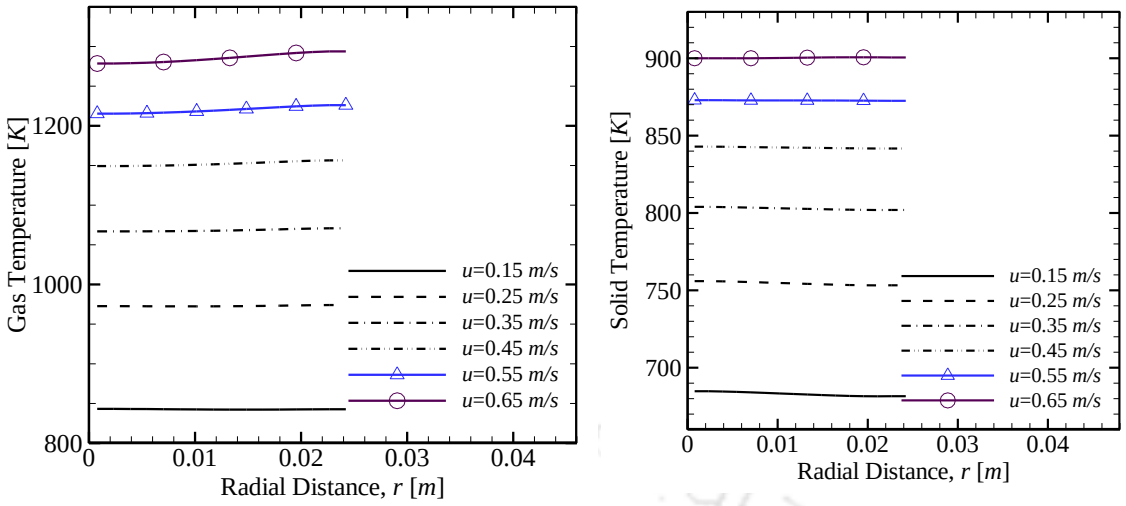

(a) (b)

Figure 6.6: Effect of air velocity on (a) the gas and (b) the solid temperature distribution along the radial direction $(0 \le r \le R, L_z = 1.0)$.

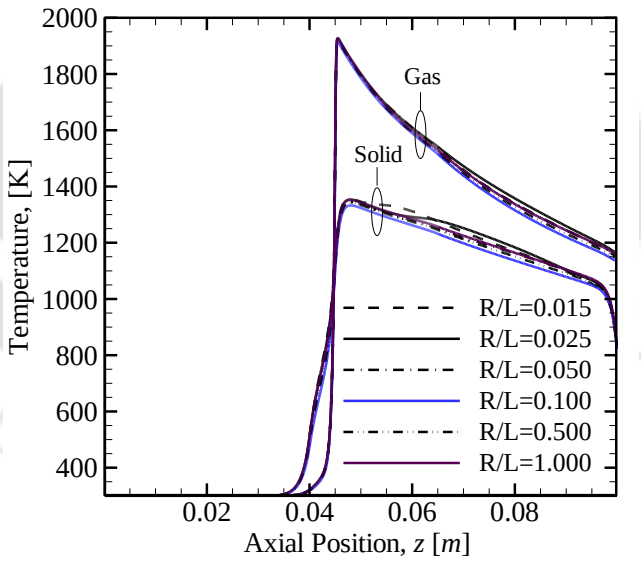

Figure 6.7: Effect of aspect ratio on the solid and the gas temperature distribution along the axial direction $(\mathrm{r} = 0, 0 \le z \le L_z)$.

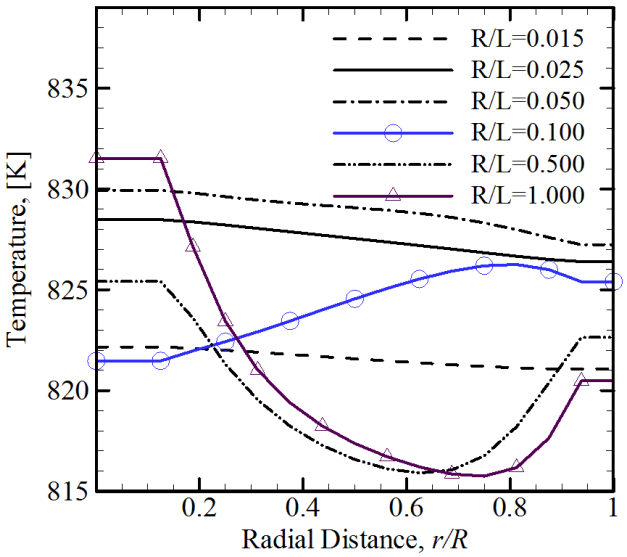

Figure 6.8: Effect of number of aspect ratio on the solid temperature distribution along the radius $(0 \le r \le R, L_z = 1.0)$.

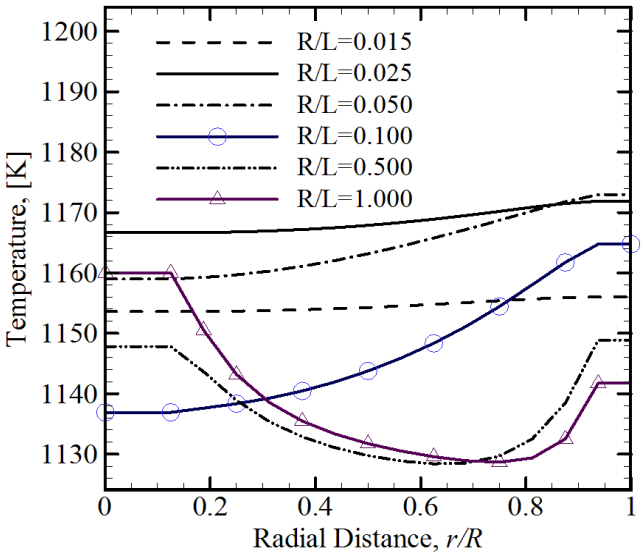

Figure 6.9: Effect of number of aspect ratio on the gas temperature distribution along the radius $(0 \le r \le R, L_z = 1.0)$.

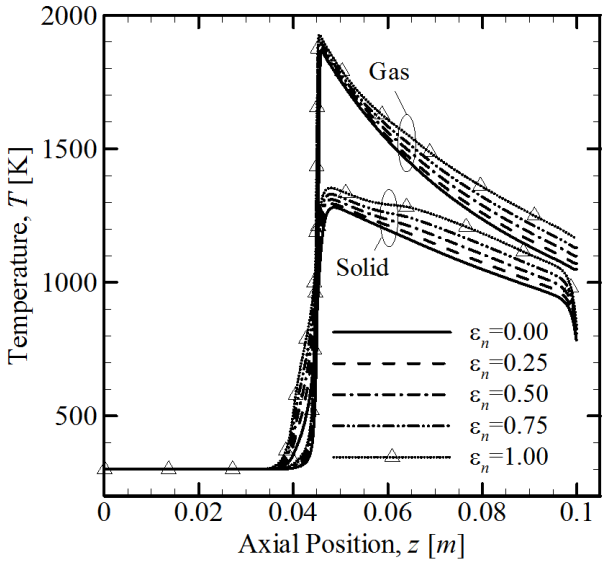

Figure 6.10: Effect of circumference emissivity on the solid and the gas temperature distribution along the axial direction $(\mathrm{r}=0, 0 \le z \le L_z)$.

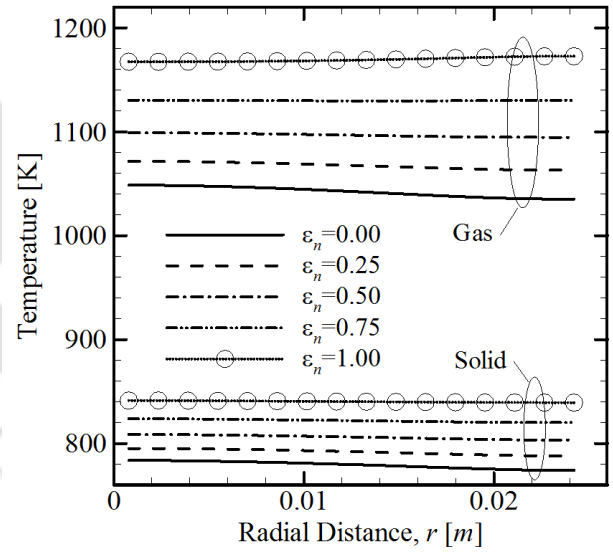

Figure 6.11: Effect of circumference emissivity on the gas and the solid temperature distribution along the radial direction $(0 \le r \le R, L_z = 1.0)$.

Once the direct model is prepared and helped us in understanding the heat transfer characteristics of PRB, attention is given to estimation of parameter. The objective

function required to be minimized in the inverse analysis by employing global search algorithm, is constructed as:

$$J = \sum_{i=1}^{N_z} \left(\tilde{\theta}_i - \frac{\left(T_{g,i} + T_{s,i} \right)}{2} \right)^2 \tag{6.17}$$

Here $\tilde{\theta}_i$ is the temperature distribution obtained through experimental data, whereas $T_{g,i}$ and $T_{s,i}$ are the unknown gas and solid temperatures respectively. The estimated parameter, CPU time requirement, best fitness and error in estimation are shown in Table 6.2. Three different optimization algorithms, namely, Global Search Algorithm (GSA), Pattern Search Algorithm (PSA) and Genetic Algorithm (GA), are tested. All optimization algorithm has its own pros and cons. Any optimization algorithm is either deterministic or probabilistic or combination of both, thereby making the selection of an optimization algorithm for a given problem to be very difficult. High computation cost involved with the inverse analysis, particularly during simultaneous estimation of several parameters can be another issue to consider. Therefore, to have a conservative comparison of the three selected tools, a single test case is tried first with each of the three algorithms (GSA, PSA, and GA). It is observed that PSA is computationally most efficient without any compromise in efficiency. Hence further test cases are attempted with PSA. It is noticed that, for single-parameter estimation, accuracy is high with both experimental and numerical data. When numerical data is used to construct the objective function, PSA is able to estimate the two parameters with higher accuracy compared to GA. But when experimental data is used to construct the objective function, the accuracy of estimation falls drastically. This is due to the uncertainty in the available data, such as pore diameter, porosity and the knowledge of temperature only along the axial grid points. The time taken by GSA is highest followed by GA. The run was taken on 2.1 GHz processor with 2 GB RAM.

Table 6.2. Estimated values of parameters.

Algorithm	First variable to be estimated				Second variable to be estimated				Total error $E=\sqrt{E_1^2+E_2^2}$	Input Data	Best fitness f	CPU Time (s)
	Variable	True value	Estimated value	Error E_1	Variable (mm)	True value	Estimated value	Error E_2				
GSA	ω	0.8	0.45	-42.92					42.92	Numerical	93	1864194
PSA	Φ	0.65	0.50	-23.08					23.08	Numerical	184	28137
			0.50	-23.08					23.08	Experimental	99	28497
			0.50	-23.08	d	1.52	3.00	97.37	100.07	Experimental	52	60203
			0.50	-23.08			1.57	3.29	23.31	Numerical	26	99013
GA			0.57	-12.31			3.00	97.37	98.15	Experimental	52	970417

6.4 Summary

A numerical model is developed for a two-stage 2D-axisymmetric PRB. Two separate energy equations for the gas- and solid-phases are taken to account for local thermal non-equilibrium. Combustion of methane is simulated by single-step global mechanism. Heat transfer characteristics of PRB is studied for different flow rates, geometric ratios and circumferential emissivity. It is found that, with the increase of flow velocity the maximum temperature of both the solid and gas phase rises. Also, for lower values of velocity there is more preheating of the unburned fuel-air mixture. The axial temperature profiles of the two phases are not following any trend with the change of aspect ratio. While the radial temperature profiles of the two phases are flat for lower aspect ratio and variation increases with the increase of aspect ratio. With the increase of circumference emissivity, the temperature of the two phases increases. In the simultaneous estimation of parameters through inverse analysis, three optimization algorithms are employed and their comparative performance is evaluated. Two parameters were successfully estimated simultaneously. GSA, PSA and GA are the optimization tools considered for comparison. The PSA outperforms other optimization algorithms in terms of accuracy and simulation time requirement.

Chapter 7

CONCLUSIONS AND SCOPE FOR FUTURE WORK

7.1 Conclusions

This dissertation dealt with the inverse analysis problems of conduction-radiation heat transfer in porous media in 1-D planar, 2-D rectangular and 2-D axisymmetric geometry. Simultaneous estimation of unknown parameters such as medium and boundary properties as well as unknown geometry and flow conditions was done. The governing energy equations were solved using the FDM and the FVM was used to compute the radiative information. However, the DTM was used for the solution of radiative transfer problem in the 1-D planar geometry. In the inverse analysis, different optimization tools such as the GA, the GSA, the PSA, the SAA, the MSPA etc. were used. The usage of the FDM, the FVM or the DTM, and a number of optimization tools, was studied for the simultaneous estimation of various unknown properties and/or unknown boundary conditions. The quality of the estimated values of the unknown parameters was studied for the effect of different optimization algorithms and measurement errors. The CPU times involved in the direct method and those required in the inverse method were also compared. Following findings are observed based on the current work:

- Use of numerical as well as experimental data, for the construction of objective function in the inverse analysis, is demonstrated successfully.
- Simultaneous estimation of 2-4 parameters is done with good accuracy.
- With the increase of dependent variables (like temperature field, heat flux etc.), number of independent variables/parameters that can be simultaneously estimated, increases.
- If the objective function is multiplied with a suitable number (MF), the CPU time required for simultaneous estimation, decreases.

- Various optimization tools like the GA, the GSA, the SAA, the PSA, the MSPA etc., are compared and all are able to simultaneously estimate the parameters with good accuracy. But the PSA outperforms others in CPU time with same accuracy in estimation.
- Simultaneous estimation of parameters with high accuracy is possible when the error in the input is up to 2%.
- While using the GA as optimization tool, selection of proper algorithm controlling criteria (number of generations, population size, mutation propability etc.) is very necessary for best results.

7.2 Scope for the Future Work

In the present work, unknown parameters in conduction and radiation heat transfer problems in porous media were estimated using the inverse analyses. However, this study has also paved way for further work in the area of inverse analysis in the PRB, and applications of the methods, viz., the FVM, the DTM, the GA etc. used in such problems. Keeping above in mind, scopes for the future work are enumerated below:

1. Simultaneous estimation of parameters in combined mode conduction and radiation heat transfer in porous media can be done for minimum entropy generation.
2. Simultaneous estimation of parameters in combined mode conduction and radiation heat transfer in porous media can be done for minimum thermal stresses in the porous matrix.
3. Combustion is simulated in the present model by single step global chemistry, this model can be modified by using multi step combustion kinematics.
4. Inverse analysis and heat transfer analysis can be performed under the situation when nano particles are added to the fuel.
5. Detailed analysis can be performed to study the effect of combustion of fuel when Nitrogen in air is replaced by CO_2 .
6. Combustion of liquid fuel like kerosene, in porous matrix can be studied with due consideration to evaporation.

References

1. S.R. Turns, An introduction to combustion, McGraw-Hill, New York (1996).
2. M.B. Toftegaard, J. Brix, P.A. Jensen, P. Glarborg, A.D. Jensen, Oxy-fuel combustion of solid fuels, Progress in Energy and Combustion Science, 36 (2010), pp. 581 – 625.
3. F. Durst, D. Trimis, Combustion by free flames versus combustion reactors, Clean Air, 3 (2002), pp. 1 – 20.
4. J.R. Howell, M.J. Hall, J.L. Ellzey, Combustion of hydrocarbon fuels within porous inert media, Prog Energy Combust Sci, 22 (1996), pp. 121 – 145.
5. M. M. Kamal, A.A. Mohamad, Proceedings of the Institution of Mechanical Engineers A- Journal of Power and Energy, 220 (5) (2006), pp 487 – 508.
6. R. Viskanta, J.P. Gore, Overview of cellular ceramics based porous radiant burners for supporting combustion, Clean Air, 1 (2000), pp. 167 – 203.
7. A.A.M. Oliveira, M. Kaviany, Nonequilibrium in the transport of heat and reactants in combustion in porous media, Prog Energy Combust Sci, 27 (2001), pp. 523 – 545
8. M.A. Mujeebu, M.Z. Abdullah, M.Z. Abu Bakar, A.A. Mohamad, M.K. Abdullah, A review of investigations on liquid fuel combustion in porous inert media, Prog Energy Combust Sci , 35 (2009), pp. 216 – 230.
9. A.J. Barra, J.L. Ellzey, Heat recirculation and heat transfer in porous burners, Combust Flame, 137 (2004), pp. 230–241.

10. S.B. Sathe, R.E. Peck, T.W. Tong, A numerical analysis of heat transfer and combustion in porous radiant burners, International Journal of Heat and Mass Transfer, 33 (6) (1990), pp 1331 – 38.

11. Y. Yoshizawa, K. Sasaki, R. Echigo, Analytical study of the structure of radiation controlled flame, International Journal of Heat and Mass Transfer, 31 (2) (1998), pp 311 – 19.

12. O. Pickenacker, K. Pickenacker, K. Wawrzinek, D. Trimis, W.E.C. Pritzkow, C. Muller, P. Goedtke, U. Papenburg, J. Adler, G. Standke, H. Heymer, W. Tauscher, F. Jansen, Innovative ceramic materials for porous-medium burners, Interceram, 48 (5) (1999), pp 326 – 30.

13. K. Hanamura, K. Bohda, Y. Miyairp, A study of super-adiabatic combustion engine, Energy Conversion and Management, 38 (10 – 13) (1997), pp. 1259 – 1266.

14. C.W. Park, M. Kaviany, Evaporation–combustion affected by in-cylinder, reciprocating porous regenerator, ASME Journal of Heat Transfer, 124 (2002), pp. 184 – 194.

15. J.L. Ellzey, M. William, Porous Burner For Gas Turbine Applications, (2003), United States Patent No. 2003024655.

16. C. Periasamy, S.K.S. Chinthamony, S.R. Gollahalli, Numerical modeling of evaporation process in porous media for gas turbine applications, In: Proceedings of the 42nd AIAA Aerospace Sciences Meeting and Exhibit, Reno, Nevada, No. AIAA 2004 – 139.

17. N. Delalic, Dz. Mulahasanovic, E.N. Ganic, Porous media compact heat exchanger unitdexperiment and analysis, Experimental Thermal and Fluid Science, 28 (2 – 3) (2004), pp. 185 – 192.

18. L. Malico, X.Y. Zhou, J.C.F. Pereira, Two-dimensional numerical study of combustion and pollutants formation in porous burners, Combustion Science and Technology, 152 (2000), pp. 57 – 79.

19. J.E. Sanmiguel, S.A. Mehta, R.G. Moore, An experimental study of controlled gas-phase combustion in porous media for enhanced recovery of oil and gas, ASME Transactions, 125 (2003).

20. I.Y. Akkutlu, Y.C. Yortsos, The dynamics of in-situ combustion fronts in porous media, Combustion and Flame, 134 (2003), pp. 229 – 247.

21. K. Qiu, A.C.S. Hayden, Premixed gas combustion stabilized in fiber felt and its application to a novel radiant burner, Fuel, 85 (2006), pp. 1094 – 1100.

22. J.P. Bingue, A.V. Saveliev, A.A. Fridman, L.A. Kennedy, Hydrogen production in ultra-rich filtration combustion of methane and hydrogen sulfide, International Journal of Hydrogen Energy, 27 (6) (2000), pp. 643 – 649.

23. J.P. Bingue, A.V. Saveliev, L.A. Kennedy, Optimization of hydrogen production by filtration combustion of methane by oxygen enrichment and depletion, International Journal of Hydrogen Energy, 29 (2004), pp. 1365 – 1370.

24. K. Nagano, T. Mochida, K. Ochifuji, Influence of natural convection on forced horizontal flow in saturated porous media for aquifer thermal energy storage, Applied Thermal Engineering, 22 (2002), pp. 1299 – 1311.

25. A.A. Mohamad, High efficiency solar air heater, Solar Energy, 60 (1997), pp.71 – 76.

26. G. Lauriat, R. Ghafir, Forced convective transfer in porous media. In: Vafai K, Hadim HA (editors), Handbook of porous media, New York: Marcel Dekker, 2000.

27. P. Naphon, Effect of Porous Media on the performance of the double-pass flat plate solar air heater, International communications in heat and mass transfer, 32 (2005), pp. 140 – 150.

28. P. Talukdar, S.C. Mishra, D. Trimis, F. Durst, Combined radiation and convection heat transfer in a porous channel bounded by isothermal parallel plates, International Journal of Heat and Mass Transfer, 47 (2004), pp. 1001 – 1013.

29. S.B. Sathe, R.E. Peck, T.W. Tong, Flame stabilization and multimode heat transfer in inert porous media: a numerical study, Combustion Science and Technology, 70 (1990), pp. 93 – 109.

30. M. Kaplan, M.J. Hall, The combustion of liquid fuels within a porous media radiant burners, Experimental Thermal and Fluid Science, 11 (1995), pp. 13 – 20.

31. R. Tanaka, M. Shinoda, N. Arai, Combustion characteristics of a heat-recirculating ceramic burner using a low-calorific-fuel, Energy Conversion and Management, 42 (2001), pp. 1897 – 1907.

32. S.A. Leonardi, R. Viskanta, J.P. Gore, Radiation and thermal performance measurements of a metal fibre burner, Journal of Quantitative Spectroscopy and Radiative Transfer, 73 (2002), pp. 491 – 501.

33. M.M. Kamal, A.A. Mohamad, Development of a cylindrical porous-medium burner, Journal of Porous Media, 9 (2006), pp. 469 – 481.

34. V.K. Patangi, S.C. Mishra, P. Muthukumar, R. Reddy, Studies on porous radiant burners for LPG applications, Energy 36 (2011), pp. 6074 – 6080.

35. C. Keramiotis, B. Stelzner, D. Trimis, M. Founti, Porous burners for low emission combustion: an experimental investigation, Energy, 45 (2012), pp. 213 – 219.

36. B. Yu, S-M Kum, C-E Lee, S. Lee, Combustion characteristics and thermal efficiency for premixed porous-media types of burners, Energy, 53 (2013), pp. 343 – 350.

37. H.B. Gao, Z.G. Qu, X.B. Feng, W.Q.Tao, Methane/air premixed combustion in a two-layer porous burner with different foam materials, Fuel, 115 (2014), pp. 154 – 161.

38. G. Brenner, K. Picken¨acker, O. Picken¨acker, D. Trimis, K. Wawrzinek, T. Weber, Numerical and experimental investigation of matrix-stabilized methane/air combustion in porous inert media, Combustion and Flame, 123 (2000), pp. 201 – 213.

39. C.L. Hackert, J.L. Ellzey, O.A. Ezekoye, Combustion and heat transfer in model two-dimensional porous burners, Combustion and Flame, 116 (1999), pp. 177 - 191.

40. S.C. Mishra, M. Steven, S. Nemoda, P. Talukdar, D. Trimis, F. Durst, Heat transfer analysis of a two dimensional rectangular porous radiant burner, International Communications in Heat and Mass Transfer, 33 (2006), pp. 467 – 474.

41. M.M. Keshtkar, S.A.G. Nassab, Theoretical analysis of porous radiant burners under 2-D radiation field using discrete ordinates method, Journal of Quantitative Spectroscopy and Radiative Transfer, 110 (2009), pp. 1894 – 1907.

42. J.Y. Zhang, H.S. Liu, Z.J. Xu, Numerical study on the premixed combustion in porous media burner, Advanced Materials Research. 614–615 (2013), pp. 73 – 76.

43. F.J. Weinberg, Combustion temperature: the future, Nature, 41 (1971), pp. 233 – 239.

44. D.R. Hardesty, F.J. Weinberg, Burners producing large excess enthalpies, Combustion Science and Technologies, 8 (1974), pp. 201 – 214.

45. T. Takeno, K. Sato, An Excess Enthalpy Flame Theory, Combustion Science and Technology, 20 (1979), pp. 1 – 2.

46. J. Buckmaster, T. Takeno, Blow-off and flashback of an excess enthalpy flame, Combustion and Science Technology, 25 (1981), pp. 153 – 158.

47. T. Takeno, K. Hase, Effects of solid length and heat loss on an excess enthalpy flame, Combustion and Science Technology, 31 (1983), pp. 207 – 215.

48. Y. Kotani, T. Takeno, An experimental study on stability and combustion characteristics of an excess enthalpy flame, 19th Symposium (International) on Combustion, The Combustion Institute, (1982), pp. 1503 – 1509.

49. R. Echigo, Y. Yoshizawa, K. Hanamura, T. Tominura, Analytical and experimental studies on radiative propagation in porous media with internal heat generation, Proceedings of the 8th International Heat Transfer Conference, 2 (1986), pp. 827 – 832.

50. T.W. Tong., W.Q. Lin, R.E. Peck, Radiative heat transfer in porous media with spatially-dependant heat generation, International Communications on Heat and Mass Transfer, 14 (1987), pp. 627 – 637.

51. P.F. Hsu, R.D. Matthews, The necessity of using detailed kinetics in models for premixed combustion within porous inert media, Combustion and Flame, 93 (1993), pp. 457 – 467.

52. P.F. Hsu, J.R. Howell, R.D. Matthews, A numerical investigation of premixed combustion within porous inert media, Journal of Heat Transfer, 115 (3) (1993), pp. 744 – 750.

53. V. Khanna, R. Goel, J.L. Ellzey, Measurements of emissions and radiation for methane combustion within a porous medium burner, Combustion Science and Technology, 99 (1994), pp. 133 – 142.

54. A.J. Barra, G. Diepvens, J.L. Ellzey, M.R. Henneke, Numerical study of the effects of material properties on flame stabilization in a porous burner, Combustion and Flame, 134 (2003), pp. 369 – 379.

55. S. Kakati, P. Mahanta, S.K. Kakoty, Performance analysis of pressurized kerosene stove with porous medium inserts, J. of scientific & industrial research, 66 (2007), pp. 565–569.

56. V.K. Pantangi, A.S.S.R.K. Kumar, S.C. Mishra, N. Sahoo, Performance analysis of domestic LPG cooking stoves with porous media, Int. J. Energy , 8 (2007), pp. 139– 44.

57. M. Sharma, S.C. Mishra, P. Mahanta, An experimental investigation on efficiency improvement of conventional kerosene pressure stove, Int. J. energy for a clean environment, 12 (2011), pp. 1– 4.

58. V.K.,Pantangi, S.C. Mishra, P. Muthukumar, R. Reddy, Studies on porous radiant burners for LPG (liquefied petroleum gas) cooking applications. Energy, 36 (2011), pp. 6074 – 6080.

59. S.C. Mishra, P. Muthukumar, V.K. Pantangi, Porous Radiant Burner for Domestic LPG Cooking Device with Improved Thermal Efficiency and Reduced Emissions of CO and NOx. Patent Number: 73/KOL/2013 and Reference Number: E-2/548/2013-KOL.

60. S.C. Mishra, P. Muthukumar, N.K. Mishra, Self-Aspirated LPG Domestic Cooking Stove with a Two-Layer Porous Radiant Burner (Submitted to TIFAC, New Delhi, June 2014).

61. S.C. Mishra, P. Muthukumar, N.K. Mishra, S. Panigrahi. Medium-Scale Self-Aspirated Improved Air Entrainment LPG Cooking Stove with a Two-Layer Porous Radiant Burner. (Submitted to TIFAC, New Delhi, November 2014).

62. N.K. Mishra, S.C. Mishra, P. Muthukumar, Performance characterization of a medium-scale liquefied petroleum gas cooking stove with a two-layer porous radiant burner, Applied Thermal Engineering, 89 (2015), pp. 44 – 50.

63. J. Randrianalisoa, Y. Bréchet, D. Baillis, Materials selection for optimal design of a porous radiant burner for environmentally driven requirements, Advanced Engineering Materials, 11 (2009), pp. 1049 – 1056.

64. P.J. Smith, W.A. Sowa, P.O. Hedman, Furnace design using comprehensive combustion models, Combustion and Flame, 79 (1990), pp. 111 – 121.

65. C.D. Correa, P.J. Smith, Optimization of ehtylene furnace operations, AiChe Annual General Meeting, Miami Beach, (1998).

66. R.S. Gemmen, Oxidation of low calorific value gases - Applying optimization techniques to combustor design, International Joint ASME/EPRI Power Generation Conference, Baltimore, (1998).

67. D. Büche, P. Stoll, P. Koumoutsakos, An evolutionary algorithm for multi-objective optimization of combustion processes, Center for Turbulence Research, Annual Research Briefs, (2001), pp. 231 – 239.

68. L.A. Catalano, , A. Dadone, D. Manodoro, A. Saponaro, Efficient design optimization of duct-burners for combined-cycle and cogenerative plants, Engineering Optimization, 38 (2006), pp. 801 – 820.

69. A.P. Horsman, K.J. Daun, Design Optimization of a Two-Stage Porous Radiant Burner Through Response Surface Modeling, Numer. Heat Transfer A, 60 (2011), pp. 727 – 745.

70. H.Y. Li, Estimation of thermal properties in combined conduction and radiation, Int. J. Heat Mass Transfer, 40 (1999), pp. 1545 – 1549.

71. S. Manickavasagam, M.P. Menguc, Inverse radiation/conduction problem in plane parallel media Radiat, Heat Transfer: Theory and Appl., ASME HTD, 244 (1993), pp. 67 – 75.

72. H.Y. Li, C.Y. Yang, A genetic algorithm for inverse radiation problems containing a participating medium, Int. J. Heat Mass Transfer, 40 (1996), pp. 1545 – 1549.

73. G.D. Raithby, E.H. Chui, A finite volume method for predicting radiant heat transfer in enclosures with participating medium, ASME J. Heat Transfer, 110 (1990), pp. 415 – 423.

74. R. Viskanta, R.J. Grosh, Heat transfer by simultaneous conduction and radiation in a absorbing medium, ASME J. Heat Transfer, 5 (1962), pp. 63 – 72.

75. M.A. Heaslet, R.F. Warming, Radiative transport and wall temperature slip in absorbing planar medium, Int. J. Heat Mass Transfer, 8 (1965), pp. 979 – 994.

76. H.M. Park, W.S. Jung, The Karhunen–Loeve Galerkin method for the inverse natural convection problems, Int. J. Heat Mass Transfer, 44 (2001), pp. 155 – 167.

77. S.S. Sablani, A. Kacimov, J. Perret, A.S. Mujumdr, A. Campo, Non-iterative estimation of heat transfer coefficients using artificial neural network models, Int. J. Heat Mass Transfer, 48 (2005), pp. 665 – 679

78. N.G. Shah, New method of Computation of Radiant Heat Transfer in Combustion Chambers, Ph.D. thesis, England: Imperial College, University of London, (1979).

79. F.C. Lockwood, N.G. Shah, Evaluation of an efficient radiation flux model for furnace prediction procedures, 6th Int. Heat Trans. Conf., Toronto, Vol. 2, Hemisphere Pub. Co, N.Y (Aug. 7 11, 1978).

80. G.D. Raithbay, E.H. Chui, A Finite Volume Method for Predicting Radiant Heat Transfer in Enclosures with Participating Media, ASME J Heat Transfer, 112 (1990), pp. 415 – 423.

81. J.C. Chai, S.V. Patankar, Finite Volume Method for Radiation Heat Transfer, Adv. Numer. Heat Transfer, 2 (2000), pp. 110 – 135.

82. J.C. Chai, G. Parthasarathy, H.O. Lee, S.V. Patankar, Finite Volume Radiative Heat Transfer Procedure for Irregular Geometries, J. Thermophys. Heat Transfer, 9 (1995), pp. 410 – 415.

83. M.Y. Kim, S.W. Baek, Analysis of radiative transfer in cylindrical enclosures using the finite volume method, J. Thermophys. Heat Transfer, 11 (1997), pp. 246 – 252.

84. J.Y. Murthy, S.R. Mathur, Radiative heat transfer in axisymmetric geometries using an unstructured finite-volume method, Numer. Heat Transfer B, 33 (1998), pp. 397 – 416.

85. O.M. Alifanov, Solution of an inverse problem of heat-conduction by iterative methods, J. Eng. Phys., 26 (4) (1974), pp. 471–476.

86. O.M. Alifanov, E.A. Artyukhin, Regularized numerical solution of nonlinear inverse heat-conduction problem, J. Eng. Phys., 29 (1) (1975), pp. 934 – 938.

87. A.N. Tikhonov, V.Y. Arsenin, Solution of Ill-Posed Problems, Winston & Sons, Washington, DC, (1977).

88. J.V. Beck, Calculation of surface heat flux from an internal temperature history, ASME Paper 62-HT-46, (1962).

89. J.V. Beck, B. Blackwell, A. Haji-Sheikh, Comparison of some inverse heat conduction methods using experimental data, Int. J. Heat Mass Transfer, 39 (17) (1996), pp. 3649 – 3657.

90. J.V. Beck, D.A. Murio, Combined function specification-regularization procedure for solution of inverse heat conduction problem, Am. Inst. Aeronaut. Astronaut. J., 247 (1) (1986), pp. 180 – 185.

91. A.M. Osman, K.J. Dowding, J.V. Beck, Numerical solution of the general two dimensional inverse heat conduction problem (IHCP), J. Heat Transfer, 119 (1) (1997), pp. 38 – 45.

92. C-C Ji, H-Y Jang, Experimental investigation in inverse heat conduction problem, Numer. Heat Transfer Part A, 34 (1) (1998), pp. 75 – 91.

93. F. Bozzoli, S. Rainieri, Comparative application of CGM and Wiener filtering techniques for the estimation of heat flux distribution, Inverse Probl. Sci. Eng., 19 (4) (2011), pp. 551 – 573.

94. F. Bozzoli, G. Pagliarini, S. Rainieri, Experimental validation of the filtering technique approach applied to the restoration of the heat source field, Exp. Therm. Fluid Sci., 44 (2013), pp. 858 – 867.

95. J.M. Colaço, H.R.B. Orlande, G.S. Dulikravich, Inverse and optimization problems in heat transfer, J. Braz. Soc. Mech. Sci. Eng., 28 (1) (2006), pp. 1 – 24.

96. M.N. Ozisik, H.R.B. Orlande, Inverse Heat Transfer, Taylor & Francis, New York, (2000).

97. F.D. Moura Neto, A.J. da Silva Neto, An Introduction to Inverse Problems with Applications, Springer, New York, NY, USA, (2013).

98. R. Hilbert, G. Janiga, R. Baron, D. Thévenin, Multiobjective shape optimization of a heat exchanger using parallel genetic algorithms, Int. J. Heat Mass Transfer, 49 (2006), pp. 2567 – 2577.

99. T. Dias Jr., L.F. Milanez, Optimal location of heat sources on a vertical wall with natural convection through genetic algorithms, Int. J. Heat Mass Transfer, 49 (2006), pp. 2090 – 2096.

100. R.R. Madadi, C. Balaji, Optimization of the location of multiple discrete heat sources in a ventilated cavity using artificial neural networks and micro genetic algorithm, Int. J. Heat Mass Transfer, 51 (2008), pp. 2299 – 2312.

101. P.W. Partridge, L.C. Wrobel, An inverse geometry problem for the localization of skin tumors by thermal analysis, Eng. Anal. Boundary Elem., 31 (2007), pp. 803 – 811.

102. K. Das, S.C. Mishra, Estimation of tumor characteristics in a breast tissue with known skin surface temperature, J. Therm. Biol., 38 (2013), pp. 311 – 317.

103. M. Randall, A. Lewis, A parallel implementation of ant colony optimization, J. Parallel Distrib. Comput., 62 (2002), pp. 1421 – 1432.

104. S. Vakili, M.S. Gadala, Effectiveness and efficiency of particle swarm optimization technique in inverse heat conduction analysis, Numer. Heat Transfer Part B, 56 (2) (2009), pp. 119 – 141.

105. S. Vakili, M.S. Gadala, A modified sequential particle swarm optimization algorithm with future time data for solving transient inverse heat conduction problems, Numer. Heat Transfer A, 59 (12) (2011), pp. 911 – 933.

106. R.P. Souto, H.F. Campos, S. Stephany, Reconstruction of vertical profiles of the absorption and scattering coefficients from multispectral radiances, Math. Comput. Simul., 73 (2006), pp. 255 – 267.

107. S. Stephany, J.C. Becceneri, R.P. Souto, H.F. de Campos Velho, A.J. Silva Neto, A pre-regularization scheme for the reconstruction of a spatial dependent scattering albedo using a hybrid ant colony optimization implementation, Appl. Math. Modell., 34 (2010), pp. 561 – 572.

108. A. Parwani, P. Talukdar, P.M.V. Subbarao, Performance evaluation of hybrid differential evolution approach for estimation of the strength of a heat source in a radiatively participating medium, Int. J. Heat Mass Transfer, 56 (1 – 2) (2013), pp. 552 – 560.

109. A. Parwani, P. Talukdar, P.M.V. Subbarao, A hybrid approach using CGM and DE algorithm for estimation of boundary heat flux in a parallel plate channel, Numer. Heat Transfer A, 65 (2014), pp. 461 – 481.

110. L. Gosselin, M. Tye-Gingras, F. Mathieu-Potvin, Review of utilization of genetic algorithms in heat transfer problems, Int. J. Heat Mass Transfer, 52 (2009), pp. 2169 – 2188.

111. J. Holland, Adaptation in Natural and Artificial Systems, University of Michigan Press, (1975).

112. N. Jawahar, A.N. Balaji, A genetic algorithm for two-stage distribution problem associated with a fixed charge, European Journal of Operational Research, 194 (2009), pp. 496 – 537.

113. Z. Ugray, L. Lasdon, J.C. Plummer, F. Glover, J. Kelly, R. Martí, Scatter search and local NLP solvers: a multistart framework for global optimization, INFORMS J. Comput., 19 (2007), pp. 328 – 340.

114. S. Sivanesskumar, R. Sukanesh, Performance analysis of global search algorithm based multiuser detector for multi carrier code division multiple access system under clipping noise, Journal of Computer Science, 7 (2011), pp. 638 – 643.

115. R. Hooke, T.A. Jeeves, Direct search solution of numerical and statistical problems, J. ACM, 8 (1961), pp. 212 – 229.

116. T.G. Kolda, R.M. Lewis, V. Torczon, A generating set direct search augmented Lagrangian algorithm for optimization with a combination of general and linear constraints, Technical Report SAND2006-5315, Sandia National Laboratories, August 2006.

117. D.S. Johnson, C.R. Aragon, L.A. McGeoch, C. Schevon, Optimization by simulated annealing: An experimental evaluation (Parts 1 and 2), Report, AT&T Bell Laboratories, Murray Hill, NJ, (1987).

118. S.B. Gelfand, Analysis of simulated annealing type algorithms, Ph.D. Thesis, MIT, Cambridge, MA (1987).

119. P.J.M. van Laarhoven, E.H.L. Aarts, Simulated Annealing: Theory and Applications, D. Reidel, Dordrecht, The Netherlands (1987).

120. L. Dixon, G. P. Szegö, The Global Optimization Problem: an Introduction, in L.C.W. Dixon and G.P. Szegö (eds.), Towards Global Optimisation, Amsterdam, The Netherlands: North Holland, 2(1978), pp. 1 – 15.

121. F. Glover, A template for scatter search and path relinking, Artificial Evolution (J.-K. Hao, E.Lutton, E.Ronald, M.Schoenauer, D.Snyers, eds.), Lecture Notes in Computer Science, 1363, Springer, Berlin/Heidelberg, (1998), pp. 13 – 54.

122. T. Tong, S. Sathe, Heat transfer characteristics of porous radiant burners, Trans. ASME, Journal Heat Transfer, 113 (1991), pp.423 – 428.

123. P.F. Hsu, J.R. Howell, Measurement of thermal conductivity and optical properties of porous partially stabilized zirconia, Experimental Heat Transfer, 5 (1992), pp. 293 – 313.

124. L.B. Younis, R. Viskanta, Experimental determination of the volumetric heat transfer coefficient between stream of air and ceramic foam, Internation Journal of Heat and Mass Transfer, 36 (6) (1993), pp. 1425 – 1434.

125. W.M. Mathis, J.L. Ellzey, Flame stabilization, operating range, and emissions for a methane/air porous burner, Combust Sci Technol, 175 (2003), pp. 825 – 839.

126. M. Farzaneh, M. Shafiey, R. Ebrahimi, M. Shams, Numerical investigation of premixed combustion in a porous burner with integrated heat exchanger, Heat Mass Transfer, 48 (2012), pp. 1273 – 1283.

127. M.R. Henneke, J.L. Ellzey, Modeling of filtration combustion in a packed bed, Combust. Flame, 117 (4) (1999), pp. 832 – 840.